Published for SISSA by Springer

Received: *September 26, 2025*
Revised: *January 30, 2026*
Accepted: *January 31, 2026*
Published: *April 2, 2026*

Towards a unified framework for pseudo-Nambu-Goldstone Dark Matter and electroweak baryogenesis

Thomas Biekötter[a], **Pedro Gabriel**[b,c], **Milada Margarete Mühlleitner**[b] and **Rui Santos**[c,d]

[a] *Instituto de Física Teórica UAM/CSIC, Calle Nicolás Cabrera 13-15, Cantoblanco, 28049, Madrid, Spain*
[b] *Institute for Theoretical Physics, Karlsruhe Institute of Technology, Wolfgang-Gaede-Str. 1, 76131 Karlsruhe, Germany*
[c] *Centro de Física Téorica e Computacional, Faculdade de Cîencias, Universidade de Lisboa, Campo Grande, Edifício C8 1749-016 Lisboa, Portugal*
[d] *ISEL — Instituto Superior de Engenharia de Lisboa, Instituto Politécnico de Lisboa, 1959-007 Lisboa, Portugal*

E-mail: thomas.biekoetter@desy.de, ptgabriel@fc.ul.pt, milada.muehlleitner@kit.edu, rasantos@fc.ul.pt

Abstract: We propose the complex singlet-extended 2-Higgs-Doublet Model (cS2HDM), a spin-0 Dark Matter (DM) model with a Higgs sector consisting of two Higgs doublets and a complex singlet, as a benchmark for LHC DM searches. The model predicts a pseudo-Nambu-Goldstone DM candidate whose interactions with nuclei are naturally suppressed, while allowing for all sources of CP-violation under the assumption of flavour alignment in the Yukawa sector, which enables CP-violating interactions of the Higgs bosons even in the alignment limit. This feature makes the model attractive for studies of electroweak baryogenesis while accommodating a Higgs-portal DM candidate with standard thermal freeze-out. We confront the model with a comprehensive set of theoretical and experimental constraints, including Higgs-boson signal strength measurements, searches for additional Higgs bosons, DM relic abundance and direct detection, as well as electroweak precision observables and the electron EDM, with emphasis on the impact of the new CP-violating sources. For DM direct detection, we perform a one-loop computation of DM-nucleon scattering including CP-violating effects. We provide a public software package to facilitate future phenomenological studies of the cS2HDM.

Keywords: Dark Matter at Colliders, Multi-Higgs Models, Specific BSM Phenomenology

ArXiv ePrint: 2509.01682

Open Access, © The Authors.
Article funded by SCOAP[3].

https://doi.org/10.1007/JHEP04(2026)038

JHEP04(2026)038

Contents

1 Introduction **1**

2 The model cS2HDM **4**
- 2.1 Higgs sector 4
- 2.2 Yukawa sector 7
- 2.3 Parameter basis 9
- 2.4 The dark sector 11
- 2.5 CP-violation 12
- 2.6 Comments on the early universe 15

3 Constraints **16**
- 3.1 Vacuum stability 17
- 3.2 Perturbative unitarity 18
- 3.3 Collider constraints 19
- 3.4 Dark-Matter constraints 25
- 3.5 Electric dipole moments 35

4 Benchmark planes and scans **37**
- 4.1 The electron EDM constraint 38
- 4.2 DM direct detection 40
- 4.3 LHC sensitivity to CP-violating Higgs boson couplings 42
- 4.4 Benchmark point with a strong first-order electroweak phase transition 46

5 Conclusions and outlook **49**

1 Introduction

The Standard Model (SM) contains a minimal prescription of electroweak (EW) symmetry breaking postulating a single fundamental scalar particle. In 2012 the ATLAS and the CMS collaborations reported the discovery of a new particle at the Large Hadron Collider (LHC) in agreement with the predictions of the SM [1, 2]. After the Run 2 of the LHC operating at 13 TeV, the coupling measurements of the detected Higgs boson have reached a precision of better than 10% in the experimentally most sensitive channels [3, 4]. So far, no significant discrepancies from the SM predictions have been observed, such that any realistic model has to contain a spin-0 particle that behaves — within the current experimental uncertainties — according to the predictions of the SM.

With the Higgs boson the last missing fundamental particle contained in the SM has been observed. However, cosmological and astronomical observations are in disagreement with the SM, calling for extensions of the SM particle content. For instance, the SM does not contain a particle that can contribute to the observed relic density of cold Dark Matter (DM), and it does not explain the origin of the observed asymmetry between matter and antimatter in the Universe. These shortcomings can be addressed in theories beyond the Standard Model (BSM) that feature extended scalar sectors. These models generically predict additional spin-0 particles. The search for additional Higgs bosons is one of the prime tasks of the current and future LHC programme [5].

JHEP04(2026)038

An important class of models with extended Higgs sectors consists of the so-called *Higgs-portal* DM models [6, 7], where the particles contained in the dark sector interact with the visible/SM sector exclusively via the exchange of Higgs bosons. In fact, in the SM the dimension-two operator $|H|^2$, where H is the Higgs doublet field, is the only gauge- and Lorentz-invariant operator to which a dark sector with fields that are not charged under the SM gauge interactions can be coupled to in a renormalizable way [8]. Given the fact that this operator is super-renormalizable, from an effective-field-theory perspective a Higgs-portal coupling between the dark sector and the visible sector is in general a renormalizable operator that can be relevant even if it is generated at energy scales that are much larger than the electroweak scale.

In the context of models with extended scalar sectors, Higgs-portal DM can be realized most economically by extending the SM with a real gauge singlet scalar field acting as the DM [9]. However, this minimal possibility is excluded by DM direct detection experiments apart from a small mass interval where the DM mass is approximately equal to half the mass of the 125 GeV Higgs boson or for rather heavy DM masses of more than about 2 TeV, leaving only little discovery potential for the LHC [10, 11]. Phenomenologically more interesting models arise under the presence of a complex gauge singlet field, where (depending on the applied symmetry on the singlet field) one component of the singlet field can act as the DM particle and the other component can mix with the Higgs field contained in the SM, giving rise to the presence of a second Higgs boson [12]. Notably, this construction allows for the presence of so-called pseudo-Nambu-Goldstone (pNG) DM [13] which is naturally faint to direct-detection experiments as a consequence of a softly broken global U(1) symmetry (see discussion below). This feature makes the model especially appealing for DM searches at particle colliders [14], whereas in other models a possible detection at colliders is largely ruled out by DM direct-detection experiments. However, in the minimal pNG DM model it is not possible to accommodate additional sources of CP-violation, and one cannot account for a strong first-order electroweak (EW) phase transition [15], both required to realize EW baryogenesis [16, 17] (see ref. [18] for a recent review). As such, the complex-singlet extended SM is not able to explain the observed asymmetry between matter and antimatter in the Universe, while at the same time containing a pNG DM state.

In light of this, pNG DM models have been studied that — in addition to a complex gauge singlet scalar field — augment the Higgs sector of the SM by a second Higgs doublet [19–25]. In a 2-Higgs-Doublet Model (2HDM) the additional quartic couplings in the potential allow for a strong first-order EW phase transition by means of sizable radiative and thermal corrections to the effective potential [26]. Additionally, the 2HDM in general also contains additional sources of CP-violation in the Higgs sector [27].[1] Consequently, 2HDM + complex singlet models are the minimal framework for pNG DM models that in addition have the potential to dynamically generate the matter-antimatter asymmetry of the Universe via EW baryogenesis.[2]

[1] An exception is the so-called inert 2HDM in which the two doublets have opposite parity under an exact $\mathbb{Z}_2$ symmetry.

[2] The DM and collider phenomenology of more general 2HDM models extended with a complex scalar singlet, where no natural suppression mechanism of direct-detection scattering rates is present and without considering CP-violation in the scalar sector, has been studied, for example, in refs. [28–31].

JHEP04(2026)038

The fact that EW baryogensis may be realized without spoiling the cancellation mechanism that suppresses the scattering rates at DM direct-detection experiments distinguishes the model from models in which the stringent constraints from DM direct-detection experiments are evaded by assuming that the Higgs portal is confined to the CP-odd sector. The minimal UV-complete realization of such a pseudoscalar Higgs-portal is the 2HDM+a [32, 33]. The 2HDM+a has been used most commonly as one of the benchmark models for LHC DM searches during Run 2 [34]. There, due to the pseudoscalar nature of the portal couplings, the spin-independent interactions between the DM and nucleons are momentum-suppressed [35, 36]. However, in general this attractive feature of the 2HDM+a is lost if there are explicit CP-violating phases in the scalar potential, in contrast to the cancellation mechanism that protects pNG DM which is related to the global U(1) symmetry and not the CP-symmetry.[3] Another important difference between the model put forward here and the 2HDM+a is that in our model the DM particle and its portal couplings are contained in the scalar sector, whereas in the 2HDM+a the DM particle and its interactions with the visible sector are in principle yet undefined (typically the DM particle in the 2HDM+a is chosen to be a Dirac fermion with Yukawa-like portal couplings).

According to the discussion above, we propose in this paper the CP-violating singlet-extended 2HDM (cS2HDM) as a benchmark model for future LHC DM searches and LHC searches for additional Higgs bosons motivated by the simultaneous description of both DM and EW baryogenesis.[4] To this end, we provide the necessary computational tools in order to study the phenomenology of the cS2HDM via the software package `cs2hdmtools` available at:

https://gitlab.com/thomas.biekoetter/cs2hdmtools

This tool includes predictions for the branching ratios of the Higgs bosons via a modified version of the public code `HDECAY` [39, 40], cross section predictions and methods to confront the model with measurements from the LHC via an interface to the public code `HiggsTools` [41], and predictions for the EW ρ-parameter and the electron electric dipole moment (eEDM) that can be used to indirectly constrain the parameter space of the model with precision measurements. Furthermore, we provide functions to apply theoretical constraints from vacuum stability and from perturbative unitarity that give rise to important bounds on the parameters in the scalar potential. Finally, we provide an interface to the public code `micrOMEGAs` [42, 43] to compute the DM relic abundance assuming thermal freeze-out in the early universe, and we provide routines to compute the one-loop induced DM-nucleon scattering interactions that can be used to confront the cS2HDM with current and future constraints from DM direct detection experiments.

The outline of the paper is as follows. In section 2 we introduce the model, with a special focus on the various new sources of explicit CP-violation and the Higgs-portal interactions of the DM scalar. In section 3 we discuss the theoretical and experimental constraints that are relevant in the cS2HDM, and we discuss how we confront the model with these

[3] In the 2HDM+a, the cancellation can be maintained if the CP-violation necessary for EW baryogenesis is generated spontaneously at finite temperature and vanishes at zero temperature [37, 38]. In our paper, we restrict the discussion to explicit CP violation in the scalar sector.

[4] The same model has recently been discussed in ref. [24], focusing on the predictions for the eEDM and the indirect detection of DM in the numerical analysis.

JHEP04(2026)038

constraints in our numerical analysis. In section 4 we present a selection of representative benchmark scenarios that demonstrate how the model can manifest itself at the LHC with novel signatures and CP-violating couplings of the 125 GeV Higgs boson, while satisfying all theoretical and experimental constraints and, in addition, predicting a large fraction or all of the observed DM relic abundance. We summarize and conclude our findings in section 5.

2 The model cS2HDM

The cS2HDM extends the particle content of the SM by a second Higgs doublet field and a complex gauge singlet scalar. In this section we introduce all elements of the model that are relevant for our numerical analysis, and we fix the notation used throughout the paper.

2.1 Higgs sector

The scalar potential is defined such that the singlet field Φ_S respects a global U(1) symmetry which is only softly broken via a dimension-two term. Under this assumption, the most general scalar potential can be written as

$$\begin{aligned} V = {} & m_{11}^2|\Phi_1|^2 + m_{22}^2|\Phi_2|^2 - \left(m_{12}^2\Phi_1^\dagger\Phi_2 + \text{h.c.}\right) + \frac{1}{2}m_S^2|\Phi_S|^2 - \frac{1}{4}\left(m_\chi^2\Phi_S^2 + \text{h.c.}\right) \\ & + \frac{1}{2}\lambda_1|\Phi_1|^4 + \frac{1}{2}\lambda_2|\Phi_2|^4 + \lambda_3|\Phi_1|^2|\Phi_2|^2 + \lambda_4(\Phi_1^\dagger\Phi_2)(\Phi_2^\dagger\Phi_1) \\ & + \left(\frac{1}{2}\lambda_5(\Phi_1^\dagger\Phi_2)^2 + \lambda_6(\Phi_1^\dagger\Phi_2)|\Phi_1|^2 + \lambda_7(\Phi_1^\dagger\Phi_2)|\Phi_2|^2 + \text{h.c.}\right) \\ & + \frac{1}{2}\lambda_8|\Phi_S|^4 + \lambda_9|\Phi_S|^2|\Phi_1|^2 + \lambda_{10}|\Phi_S|^2|\Phi_2|^2 + \left(\lambda_{11}(\Phi_1^\dagger\Phi_2)|\Phi_S|^2 + \text{h.c.}\right), \end{aligned} \tag{2.1}$$

where Φ_1 and Φ_2 are SU(2) doublet fields with hypercharge 1/2, and Φ_S is the gauge singlet complex scalar field. As pointed out in ref. [24], the term proportional to λ_{11} is redundant and could be removed via a field redefinition of Φ_1 and Φ_2. However, we write the potential including this terms since it allows us to use a physically more convenient basis for the input parameters using 6 independent angles that parametrize the mixing of the neutral scalars. The parameters $m_{12}^2, m_\chi^2, \lambda_5, \lambda_6, \lambda_7, \lambda_{11}$ can be complex, whereas the remaining parameters are real.

The electroweak vacuum is defined in such a way that the neutral components of the Higgs doublets Φ_1 and Φ_2 and the singlet field have non-zero real vacuum expectation values (vevs) v_1, v_2 and v_S, respectively. In this case the scalar fields can be expanded around their vevs and written as

$$\Phi_1 = \begin{pmatrix} \varphi_1^+ \\ (v_1 + \varphi_1 + \mathrm{i}\sigma_1)/\sqrt{2} \end{pmatrix}, \quad \Phi_2 = \begin{pmatrix} \varphi_2^+ \\ (v_2 + \varphi_2 + \mathrm{i}\sigma_2)/\sqrt{2} \end{pmatrix}, \quad \Phi_S = (v_S + \varphi_S + \mathrm{i}\chi)/\sqrt{2}\,. \tag{2.2}$$

We assume v_1 and v_2 to be real since we do not consider the possibility of spontaneous CP-violation. We leave the exploration of spontaneous CP-violation in the model for future work and focus here on explicit CP-violation. A complex vev v_S would spoil the stability of the DM candidate χ, see discussion below. The stationary conditions with respect to

JHEP04(2026)038

the three fields that obtain a vev are then given by

$$\frac{\partial V}{\partial \varphi_1} = 0 \Rightarrow$$
$$m_{11}^2 = \frac{v_2}{v_1}(m_{12}^2)^{\mathrm{Re}} - \frac{v_1^2}{2}\lambda_1 - \frac{v_2^2}{2}\left(\lambda_3 + \lambda_4 + \lambda_5^{\mathrm{Re}}\right) - \frac{3v_1v_2}{2}\lambda_6^{\mathrm{Re}} - \frac{v_2^3}{2v_1}\lambda_7^{\mathrm{Re}} - \frac{v_2v_S^2}{2v_1}\lambda_{11}^{\mathrm{Re}}\,, \tag{2.3}$$

$$\frac{\partial V}{\partial \varphi_2} = 0 \quad \Rightarrow$$
$$m_{22}^2 = \frac{v_1}{v_2}(m_{12}^2)^{\mathrm{Re}} - \frac{v_2^2}{2}\lambda_2 - \frac{v_1^2}{2}\left(\lambda_3 + \lambda_4 + \lambda_5^{\mathrm{Re}}\right) - \frac{v_1^3}{2v_2}\lambda_6^{\mathrm{Re}} - \frac{3v_1v_2}{2}\lambda_7^{\mathrm{Re}} - \frac{v_1v_S^2}{2v_2}\lambda_{11}^{\mathrm{Re}}\,, \tag{2.4}$$

$$\frac{\partial V}{\partial \varphi_S} = 0 \quad \Rightarrow$$
$$m_S^2 = (m_\chi^2)^{\mathrm{Re}} - v_S^2\lambda_8 - v_1^2\lambda_9 - v_2^2\lambda_{10} - 2v_1v_2\lambda_{11}^{\mathrm{Re}}\,, \tag{2.5}$$

where the superscript 'Re' refers to the real component of the respective parameter. In order to make connection to the 2HDM with natural flavour conservation, we define the parameter $\tan\beta = v_2/v_1$. However, it should be kept in mind that without a discrete symmetry applied on the Higgs doublets that acts differently on Φ_1 and Φ_2, the parameter $\tan\beta$ is not basis invariant and has no direct physical meaning in the general case [44].

All terms in eq. (2.1) that contain the singlet field Φ_S respect a global U(1) symmetry, with the exception of the dimension-two term proportional to m_χ^2 in the first line. If $v_S > 0$, the imaginary component of Φ_S acts as a pseudo-Nambu-Goldstone boson under this symmetry. The mass of χ is then given by the U(1)-breaking parameter m_χ. A discrete symmetry $\chi \to -\chi$ remains as a remnant of the U(1) symmetry, such that χ is stable and can play the role of the DM candidate of the model.

As stated above, the scalar potential contains six potentially complex parameters: $m_{12}^2, m_\chi^2, \lambda_5, \lambda_6, \lambda_7, \lambda_{11}$. In the following, we will denote with a^{Re} and a^{Im} the real and imaginary parts of a complex parameter a, respectively. The imaginary components of the complex parameters in the scalar potential can in general be the source of explicit CP-violation. However, assuming an electroweak vacuum as given in eq. (2.2), the imaginary part of m_χ^2 has to vanish according to the stationary condition,

$$\frac{\partial V}{\partial \chi} = (m_\chi^2)^{\mathrm{Im}} = 0\,. \tag{2.6}$$

Moreover, using the stationary conditions with respect to either of the two CP-odd doublet components[5] σ_1 and σ_2, one can express the imaginary part of m_{12}^2 in dependence of the imaginary parts of the complex quartic couplings, such that

$$(m_{12}^2)^{\mathrm{Im}} = \frac{v_1v_2}{2}\lambda_5^{\mathrm{Im}} + \frac{v_1^2}{2}\lambda_6^{\mathrm{Im}} + \frac{v_2^2}{2}\lambda_7^{\mathrm{Im}} + \frac{v_S^2}{2}\lambda_{11}^{\mathrm{Im}}\,. \tag{2.7}$$

Hence, only four independent CP-violating phases remain in the Higgs potential. As will be discussed in section 2.3, one can use three (of a total of six) mixing angles in the neutral scalar

[5]Since the theory is CP-violating there are no CP-odd fields. We call them CP-odd to make the connection with the CP-conserving version of the model, noting that they do not correspond to a physical mass eigenstate.

JHEP04(2026)038

sector in order to parametrize the mixing of gauge eigenstates with opposite CP charges. In this case the imaginary parts of λ_6, λ_7 and λ_{11} are dependent parameters, and only the imaginary part of λ_5 remains as free input parameter.

After decomposing the neutral scalar fields in real and imaginary parts, there are a total of six real neutral scalar fields φ_1, φ_2, σ_1, σ_2, φ_S and χ, see eq. (2.2). As a consequence of the global U(1) symmetry and since v_S is real, the field χ does not mix with the other fields. Furthermore, a rotation of the imaginary components of the doublet fields via the angle β in the form $\sigma_1 = s_\beta A_0 + c_\beta G_0$ and $\sigma_2 = c_\beta A_0 - s_\beta G_0$ removes the mixing between the unphysical Goldstone boson G_0 and the physical states. The field A_0 corresponds to a CP-odd state that in general is not a mass eigenstate but mixes with the CP-even fields φ_1, φ_2 and φ_S under the presence of CP-violation. Hence, there are a total of four neutral scalar Higgs bosons in the model. The mass matrix of the neutral scalar sector can be written in the field basis $\phi = (\varphi_1, \varphi_2, \varphi_S, A_0)$ as

$$-\mathcal{L} = \phi^T \mathcal{M}_H^2 \phi\,, \quad \text{with } \left(\mathcal{M}_H^2\right)_{ij} = \frac{\partial^2 V}{\partial\phi_i \phi_j}\,, \tag{2.8}$$

where the elements of the mass matrix are not written here for the sake of brevity. In order to obtain the mass eigenstates, we define the 4×4 orthogonal matrix R that diagonalizes $\mathcal{M}_H^2$ such that

$$\begin{pmatrix} m_{H_1}^2 & 0 & 0 & 0 \\ 0 & m_{H_2}^2 & 0 & 0 \\ 0 & 0 & m_{H_3}^2 & 0 \\ 0 & 0 & 0 & m_{H_4}^2 \end{pmatrix} = R\, \mathcal{M}_H^2 R^T\,, \tag{2.9}$$

with m_{H_i} being the masses of the neutral Higgs bosons. We parametrize the mixing matrix R in term of six mixing angles $\alpha_{i=1,\ldots,6}$ as

$$R_{11} = \cos\alpha_1 \cos\alpha_2 \cos\alpha_6\,, \tag{2.10}$$

$$R_{12} = \cos\alpha_2 \cos\alpha_6 \sin\alpha_1\,, \tag{2.11}$$

$$R_{13} = \cos\alpha_6 \sin\alpha_2\,, \tag{2.12}$$

$$R_{14} = -\sin\alpha_6\,, \tag{2.13}$$

$$\begin{aligned} R_{21} = &-\sin\alpha_1(\cos\alpha_3 \cos\alpha_4 + \sin\alpha_3 \sin\alpha_4 \sin\alpha_5) + \cos\alpha_1(-\sin\alpha_2(\cos\alpha_4 \sin\alpha_3 \\ &- \cos\alpha_3 \sin\alpha_4 \sin\alpha_5) - \cos\alpha_2 \cos\alpha_5 \sin\alpha_4 \sin\alpha_6)\,, \end{aligned} \tag{2.14}$$

$$\begin{aligned} R_{22} = &\cos\alpha_1(\cos\alpha_3 \cos\alpha_4 + \sin\alpha_3 \sin\alpha_4 \sin\alpha_5) + \sin\alpha_1(-\sin\alpha_2(\cos\alpha_4 \sin\alpha_3 \\ &- \cos\alpha_3 \sin\alpha_4 \sin\alpha_5) - \cos\alpha_2 \cos\alpha_5 \sin\alpha_4 \sin\alpha_6)\,, \end{aligned} \tag{2.15}$$

$$R_{23} = \cos\alpha_2(\cos\alpha_4 \sin\alpha_3 - \cos\alpha_3 \sin\alpha_4 \sin\alpha_5) - \cos\alpha_5 \sin\alpha_2 \sin\alpha_4 \sin\alpha_6\,, \tag{2.16}$$

$$R_{24} = -\cos\alpha_5 \cos\alpha_6 \sin\alpha_4\,, \tag{2.17}$$

$$R_{31} = \cos\alpha_5 \sin\alpha_1 \sin\alpha_3 - \cos\alpha_1(\cos\alpha_3 \cos\alpha_5 \sin\alpha_2 + \cos\alpha_2 \sin\alpha_5 \sin\alpha_6)\,, \tag{2.18}$$

$$R_{32} = -\cos\alpha_1 \cos\alpha_5 \sin\alpha_3 - \sin\alpha_1(\cos\alpha_3 \cos\alpha_5 \sin\alpha_2 + \cos\alpha_2 \sin\alpha_5 \sin\alpha_6)\,, \tag{2.19}$$

$$R_{33} = \cos\alpha_2 \cos\alpha_3 \cos\alpha_5 - \sin\alpha_2 \sin\alpha_5 \sin\alpha_6\,, \tag{2.20}$$

$$R_{34} = -\cos\alpha_6 \sin\alpha_5\,, \tag{2.21}$$

JHEP04(2026)038

$$R_{41} = -\sin\alpha_1(\cos\alpha_3\sin\alpha_4 - \cos\alpha_4\sin\alpha_3\sin\alpha_5) + \cos\alpha_1(-\sin\alpha_2(\sin\alpha_3\sin\alpha_4 + \cos\alpha_3\cos\alpha_4\sin\alpha_5) + \cos\alpha_2\cos\alpha_4\cos\alpha_5\sin\alpha_6)\,, \tag{2.22}$$

$$R_{42} = \cos\alpha_1(\cos\alpha_3\sin\alpha_4 - \cos\alpha_4\sin\alpha_3\sin\alpha_5) + \sin\alpha_1(-\sin\alpha_2(\sin\alpha_3\sin\alpha_4 + \cos\alpha_3\cos\alpha_4\sin\alpha_5) + \cos\alpha_2\cos\alpha_4\cos\alpha_5\sin\alpha_6)\,, \tag{2.23}$$

$$R_{43} = \cos\alpha_2(\sin\alpha_3\sin\alpha_4 + \cos\alpha_3\cos\alpha_4\sin\alpha_5)\cos\alpha_4\cos\alpha_5\sin\alpha_2\sin\alpha_6\,, \tag{2.24}$$

$$R_{44} = \cos\alpha_4\cos\alpha_5\cos\alpha_6\,. \tag{2.25}$$

We note that the model features a so-called alignment limit in which one of the states H_i has couplings to fermions and gauge bosons of the same form as the ones predicted for the Higgs boson in the SM. The couplings of the mass eigenstate H_1 only depend on the mixing angles α_1, α_2 and α_6 as can be seen in eqs. (2.10)–(2.13). A convenient choice to parametrize the alignment limit is therefore

$$\alpha_1 = \beta\,, \quad \alpha_2 = \alpha_6 = 0\,, \tag{2.26}$$

in which case the state H_1 is the one resembling a SM Higgs boson of mass m_{H_1}. For instance, the couplings of the neutral Higgs bosons H_i to the massive gauge bosons, Γ_{H_iVV}, with $V = Z, W^\pm$, normalized to the corresponding ones of the SM Higgs boson, $\Gamma^{\rm SM}_{HVV}$, are in general given by

$$\kappa_i^V = \frac{\Gamma_{H_iVV}}{\Gamma^{\rm SM}_{HVV}} = \frac{v_1 R_{i1} + v_2 R_{i2}}{v} = c_\beta R_{i1} + s_\beta R_{i2}\,. \tag{2.27}$$

In the limit shown in eq. (2.26), we find $R_{11} = c_\beta$ and $R_{12} = s_\beta$, and thus $\kappa_1^V = 1$. In the same way, one can show that the couplings of H_1 to fermions become equal to the ones of the SM Higgs boson. This is discussed in detail in section 2.5.2.

One should note that in this alignment limit the singlet field is in general not decoupled since the remaining states H_2, H_3 and H_4 can still mix with each other as long as α_3, α_4 and/or α_5 are not equal to zero (see the discussion in section 3.4.1 for details).

The charged scalar sector of the model consists of a pair of physical charged Higgs bosons $H^\pm$ and the unphysical charged Goldstone bosons $G^\pm$. As in the 2HDM, the mass matrix in the charged scalar sector is diagonalized via a rotation with angle β, giving rise to the massive mass eigenstates $H^\pm$ with mass

$$m_{H^\pm} = -\frac{v_1^2 + v_2^2}{2v_1 v_2}\left(-2m_{12}^{2\,\rm Re} + v_1 v_2\left(\lambda_4 + \lambda_5^{\rm Re}\right) + v_1^2\lambda_6^{\rm Re} + v_2^2\lambda_7^{\rm Re} + v_S^2\lambda_{11}^{\rm Re}\right)\,. \tag{2.28}$$

In the absence of CP-violation one finds the relation $m_{H^\pm}^2 - m_A^2 = v^2(\lambda_5 - \lambda_4)/2$ that is known from the real 2HDM, where m_A is the mass of the CP-odd mass eigenstate A_0.

2.2 Yukawa sector

The most general Yukawa interactions can be written as

$$\mathcal{L}_{\rm Yuk} = -\sum_{a=1}^{2}\left((Y_u^{(a)})_{ij}\Phi_a Q_i \bar{u}_j + (Y_d^{(a)})_{ij}\tilde{\Phi}_a Q_i \bar{d}_j + (Y_\ell^{(a)})_{ij}\tilde{\Phi}_a L_i \bar{e}_j\right) + \text{h.c.}\,, \tag{2.29}$$

JHEP04(2026)038

where the sum runs over the two Higgs doublets, with $\tilde{\Phi}_a = (\Phi_a^T \varepsilon)^\dagger$ and $\epsilon_{21} = -1$, and the indices $i, j = 1, 2, 3$ run over the fermion flavours.[6] The Yukawa couplings $Y_{u,d,\ell}^{(1,2)}$ are 3×3 matrices in flavour spaces. Their elements can be complex, which would in general give rise to CP-violation in the Yukawa sector. After electroweak symmetry breaking, one finds the following mass matrices for the quarks and the charged leptons,

$$-\mathcal{L} = f_{iL}\,(\mathcal{M}_f)_{ij}\,f_{jR}^* + \text{h.c.}\,, \qquad (\mathcal{M}_f)_{ij} = \frac{1}{\sqrt{2}}\left(v_1 (Y_f^{(1)})_{ji} + v_2 (Y_f^{(2)})_{ji}\right)\,, \quad f_i = u_i, d_i, \ell_i\,. \tag{2.30}$$

If the matrices $Y_f^{(1)}$ and $Y_f^{(2)}$ are not diagonalizable simultaneously, the diagonalization of the fermion mass matrices would yield flavour-changing couplings of the neutral Higgs bosons to fermions, and thus to flavour-changing neutral currents (FCNC) which are tightly constraint by experiments. In order to avoid FCNC, we apply the so-called flavour-alignment scenario [45]. Here it is assumed that the Yukawa matrices $Y_f^{(1)}$ and $Y_f^{(2)}$ are proportional to each other, in which case they can be diagonalized by means of the same fermion rotation matrices which then also diagonalize the mass matrices. We parametrize the flavour alignment in terms of the flavour alignment parameters ξ_u, ξ_d and ξ_ℓ for the up-type quarks, the down-type quarks and the charged leptons, respectively, such that

$$(Y_u^{(1)})_{ij} = \xi_u\,(Y_u^{(2)})_{ij}\,, \quad (Y_d^{(1)})_{ij} = \xi_d\,(Y_d^{(2)})_{ij}\,, \quad (Y_\ell^{(1)})_{ij} = \xi_\ell\,(Y_u^{(2)})_{ij}\,. \tag{2.31}$$

The flavour alignment parameters are in general complex. Their imaginary parts constitute three sources of CP violation in the Yukawa sector. Without loss of generality, we assume the Yukawa matrices $Y_f^{(2)}$ to be diagonal,

$$Y_u^{(2)} = \text{diag}(Y_u, Y_c, Y_t)\,, \quad Y_d^{(2)} = \text{diag}(Y_d, Y_s, Y_b)\,, \quad Y_\ell^{(2)} = \text{diag}(Y_e, Y_\mu, Y_\tau)\,, \tag{2.32}$$

where the Yukawa couplings on the right-hand side of the equations are the Yukawa coupling of each fermion contained in the SM.[7] These Yukawa couplings can be written in dependence of the physical masses m_f of the fermions, the vevs of the Higgs doublets and the flavour alignment parameters,

$$Y_f = \frac{\sqrt{2}\,m_f}{\xi_f v_1 + v_2}\,, \quad f = u, c, t, d, s, b, e, \mu, \tau\,. \tag{2.33}$$

We note that although the Yukawa coupling Y_f is complex if ξ_f is complex, the elements of the fermion mass matrices shown in eq. (2.30) are always real.

In general, the flavour alignment is not protected by a symmetry. The only exception is the case in which all fermions with the same electric charge only couple to one of the two Higgs doublets, leading to the traditional Yukawa types of the 2HDM, see discussion below [46]. Thus, radiative corrections give rise to a breaking of the flavour alignment. As a consequence, the flavour alignment can be set at one particular energy scale (here assumed to be the EW scale), but the renormalization group running would induce a breaking of the

[6] We do not consider the possible presence of right-handed neutrinos. The Yukawa sector and the flavour alignment (see discussion below) can be trivially extended to take into account right-handed neutrinos.

[7] For simplicity, we neglect the quark-flavour mixing in terms of the CKM matrix in this discussion, but it is taken into account in the numerical analysis if relevant.

JHEP04(2026)038

Type	ξ_u^{Re}	ξ_d^{Re}	ξ_ℓ^{Re}	Φ_1	Φ_2
I	0	0	0	-	u, d, ℓ
II	0	∞	∞	d, ℓ	u
LS/III	0	0	∞	ℓ	u, d
FL/IV	0	∞	0	d	u, ℓ

Table 1. Correspondence between special choices of the flavour alignment parameters and the four different Yukawa types if natural flavour alignment is assumed. The imaginary parts $\xi_{u,d,\ell}^{\mathrm{Im}}$ can be chosen to be vanishing in the Yukawa types since a complex phase of the flavour alignment parameters can be removed via field redefinitions. The last two columns indicate which of the two Higgs doublets Φ_1 and Φ_2 is coupled to the different kind of fermions, where u, d and ℓ corresponds to up-type quarks, down-type quarks and charged leptons, respectively.

flavour alignment at different energy scales. This being said, if flavour alignment is assumed at the EW scale, the impact of the radiatively induced breaking of the flavour alignment at other experimentally accessible scales is typically too small to generate observable FCNCs at the current experimental precision [47].

In order to make the flavour alignment stable under the renormalization group, one can impose the so-called natural flavour alignment, where a discrete $\mathbb{Z}_2$ symmetry is responsible for the invariance of the flavour alignment. In this case, one of the Higgs doublets changes the sign while the other transforms trivially, such that only one Higgs doublet can be coupled to one kind of fermion, but not both at the same time. There are four different ways to extend the Z_2 symmetry to the fermions, giving rise to the so-called Yukawa types I, II, lepton-specific (LS)/III and Flipped (FL)/IV [48]. The four Yukawa types correspond to particular choices of the flavour parameters as summarized in table 1. Imposing such a $\mathbb{Z}_2$ symmetry is a significant restriction of the model and its phenomenology at the LHC (and other experiments) since it constrains the Higgs-boson couplings to fermions. Moreover, the symmetry removes the possibility of CP violation in the scalar sector in the Higgs alignment limit of the model. The current LHC measurements are well compatible with the predictions for a Higgs boson predicted by the SM, thus driving the model towards the alignment limit. As a consequence, the presence of CP violation in the Higgs sector, and in particular in the couplings of the Higgs boson at 125 GeV, are severely restricted by the LHC measurements if a $\mathbb{Z}_2$ is imposed (see ref. [49] for a recent analysis in the complex 2HDM). Consequently, in order to allow for the presence of CP-violation in the alignment limit we use in our analysis the less restrictive flavour alignment scenario.

2.3 Parameter basis

To investigate the phenomenology of the model, it is convenient to choose a basis of free input parameters which are more closely related to physical observables than the bare parameter appearing in the Lagrangian. In the scalar sector we make use of the masses and the mixing angles as input parameters. The mixing angles are suitable input parameters since they are related to the couplings of the scalars to fermions and gauge bosons. Using the stationary coditions of the scalar potential and the mass matrix relations shown in eq. (2.9) for the

JHEP04(2026)038

neutral and in eq. (2.28) for the charged scalars, one can trade 11 Lagrangian parameters for the physical masses and the mixing angles according to the relations

$$\lambda_1 = \frac{1}{c_\beta^2 v^2}\left[\sum_{i=1}^{4} R_{i1}^2 m_{H_i}^2 - s_\beta^2 M^2\right] - \frac{3}{2} t_\beta \lambda_6^{\mathrm{Re}} + \frac{1}{2} t_\beta^2 \lambda_7^{\mathrm{Re}} + \frac{v_S^2}{2v^2}\frac{t_\beta}{c_\beta^2}\lambda_{11}^{\mathrm{Re}}\,, \tag{2.34}$$

$$\lambda_2 = \frac{1}{s_\beta^2 v^2}\left[\sum_{i=1}^{4} R_{i2}^2 m_{H_i}^2 - c_\beta^2 M^2\right] + \frac{1}{2}\frac{1}{t_\beta^3}\lambda_6^{\mathrm{Re}} - \frac{3}{2}\frac{1}{t_\beta}\lambda_7^{\mathrm{Re}} + \frac{v_S^2}{2\,v^2}\frac{1}{s_\beta^2 t_\beta}\lambda_{11}^{\mathrm{Re}}\,, \tag{2.35}$$

$$\lambda_3 = \frac{2}{v^2} m_{H^\pm}^2 + \frac{1}{c_\beta s_\beta v^2}\left[\sum_{i=1}^{4} R_{i1} R_{i2} m_{H_i}^2 - c_\beta s_\beta M^2\right] - \frac{1}{2}\frac{1}{t_\beta}\lambda_6^{\mathrm{Re}} - \frac{1}{2} t_\beta \lambda_7^{\mathrm{Re}} + \frac{1}{s_{2\beta}}\frac{v_S^2}{v^2}\lambda_{11}^{\mathrm{Re}}\,, \tag{2.36}$$

$$\lambda_4 = -\frac{2}{v^2} m_{H^\pm}^2 + \frac{1}{v^2}\left[\sum_{i=1}^{4} R_{i4}^2 m_{H_i}^2 + M^2\right] - \frac{1}{2}\frac{1}{t_\beta}\lambda_6^{\mathrm{Re}} - \frac{1}{2} t_\beta \lambda_7^{\mathrm{Re}} - \frac{1}{s_{2\beta}}\frac{v_S^2}{v^2}\lambda_{11}^{\mathrm{Re}}\,, \tag{2.37}$$

$$\lambda_5^{\mathrm{Re}} = \frac{1}{v^2}\left[\sum_{i=1}^{4} R_{i4}^2 m_{H_i}^2 - M^2\right] - \frac{1}{2}\frac{1}{t_\beta}\lambda_6^{\mathrm{Re}} - \frac{1}{2} t_\beta \lambda_7^{\mathrm{Re}} - \frac{1}{s_{2\beta}}\frac{v_S^2}{v^2}\lambda_{11}^{\mathrm{Re}}\,, \tag{2.38}$$

$$\lambda_6^{\mathrm{Im}} = -\frac{1}{c_\beta v^2}\sum_{i=1}^{4} R_{i1} R_{i4} m_{H_i}^2 - \frac{1}{2} t_\beta \lambda_5^{\mathrm{Im}}\,, \tag{2.39}$$

$$\lambda_7^{\mathrm{Im}} = -\frac{1}{s_\beta v^2}\sum_{i=1}^{4} R_{i2} R_{i4} m_{H_i}^2 - \frac{1}{2}\frac{1}{t_\beta}\lambda_5^{\mathrm{Im}}\,, \tag{2.40}$$

$$\lambda_8 = \frac{1}{v_S^2}\sum_{i=1}^{4} R_{i3}^2 m_{H_i}^2\,, \tag{2.41}$$

$$\lambda_9 = \frac{1}{c_\beta v v_S}\sum_{i=1}^{4} R_{i1} R_{i3} m_{H_i}^2 - t_\beta \lambda_{11}^{\mathrm{Re}}\,, \tag{2.42}$$

$$\lambda_{10} = \frac{1}{s_\beta v v_S}\sum_{i=1}^{4} R_{i2} R_{i3} m_{H_i}^2 - \frac{1}{t_\beta}\lambda_{11}^{\mathrm{Re}}\,, \tag{2.43}$$

$$\lambda_{11}^{\mathrm{Im}} = -\frac{1}{v v_S}\sum_{i=1}^{4} R_{i3} R_{i4} m_{H_i}^2\,, \tag{2.44}$$

where we have introduced the parameter

$$M^2 = \frac{(m_{12}^2)^{\mathrm{Re}}}{c_\beta s_\beta}\,, \tag{2.45}$$

and the scalar mixing matrix elements R_{ij} are expressed in terms of the six mixing angles α_i as shown in eqs. (2.10)–(2.25). In the fermion sector, we will use the fermion masses and the flavour alignment parameters as input. The Yukawa couplings can then be derived from eq. (2.33). This leaves us with the following set of input parameters to specify a parameter point

$$\begin{aligned} &v = 246.2\,\mathrm{GeV}\,, \quad m_{H_1} = 125.1\,\mathrm{GeV}\,, \quad m_{H_{2,3,4}}\,, \quad m_{H^\pm}\,, \quad m_\chi\,, \quad \tan\beta\,, \quad M\,, \\ &v_S\,, \quad \alpha_{1,2,3,4,5,6}\,, \quad \lambda_5^{\mathrm{Im}}\,, \quad \lambda_6^{\mathrm{Re}}\,, \quad \lambda_7^{\mathrm{Re}}\,, \quad \lambda_{11}^{\mathrm{Re}}\,, \quad \xi_{u,d,\ell}^{\mathrm{Re}}\,, \quad \xi_{u,d,\ell}^{\mathrm{Im}}\,. \end{aligned} \tag{2.46}$$

JHEP04(2026)038

Since the number of free parameters is sizable, we will make different simplifying assumptions throughout our numerical analysis. This also facilitates the comparison to simpler models that have been extensively studied in the literature. This concerns the parameters λ_6^{Re} and λ_7^{Re} and $\lambda_{11}^{\mathrm{Re}}$ which we set to zero in order to eliminate FCNC at tree level which are tightly constrained experimentally. In addition, since we assume H_1 to play the role of the detected Higgs boson at about 125 GeV, we will make use of the conditions shown in eq. (2.26) if we impose the alignment limit. Moreover, if we consider natural flavour conservation (NFC) in terms of the well-known Yukawa types, we set $\xi_{u,d,\ell}^{\mathrm{Im}} = 0$ and, depending on the considered type, the parameters $\xi_{u,d,\ell}^{\mathrm{Re}}$ as depicted in table 1.

2.4 The dark sector

The model predicts a neutral stable scalar particle χ that plays the role of the DM candidate. χ interacts with the fermions and gauge bosons only via Higgs-boson exchange. The tree-level couplings $\chi\chi H_i$ are given by

$$\mathrm{i}\Gamma_{\chi\chi H_i} = v\left[c_\beta\lambda_9 R_{i1} + s_\beta\lambda_{10}R_{i2} + (s_\beta R_{i1} + c_\beta R_{i2})\lambda_{11}^{\mathrm{Re}} + \lambda_{11}^{\mathrm{Im}}R_{i4} + \frac{v_S}{v}\lambda_8 R_{i3}\right] = \frac{m_{H_i}^2}{v_S}R_{i3}\,, \tag{2.47}$$

where in the last step we used the parameter relations for λ_8, λ_9, λ_{10} and λ_{11} shown above and the orthogonality of the mixing matrix R to express the couplings in terms of the masses of the neutral Higgs bosons. The coupling of χ to the doublet components is generated via the terms proportional to the portal couplings λ_9, λ_{10} and λ_{11}, whose corresponding potential terms, as shown in eq. (2.1), contain both the doublet fields Φ_1 or Φ_2 and the gauge singlet field Φ_S. On the other hand, the coupling of χ to the singlet components of the states H_i is generated via the coupling λ_8 that appears in the $|\Phi_S|^4$ term in the scalar potential. One important consequence is that the detected Higgs boson at 125 GeV can be coupled to χ only if either at least one of the portal couplings is non-zero, or if it has a non-vanishing singlet admixture and $\lambda_8 > 0$. The $\mathbb{Z}_2$-breaking couplings λ_6 and λ_7 do not appear in the $\chi\chi H_i$ couplings at leading order and thus do not play a major role for the DM phenomenology. The DM particle χ is in general coupled to all four neutral Higgs bosons. This gives rise to an important distinction to the CP-conserving version of the model as studied in ref. [21], where the DM state is only coupled to the three CP-even scalars but not to the CP-odd pseudoscalar. This additional coupling of χ can play an important role for the prediction of the DM relic abundance, as will be discussed in section 3.4.1.

In the alignment limit, as defined in eq. (2.26), and additionally setting $\alpha_3 = \alpha_4 = \alpha_5 = 0$, the expression shown in eq. (2.47) can be written as

$$\mathrm{i}\Gamma_{\chi\chi H_{1,2,4}} = 0\,, \quad \mathrm{i}\Gamma_{\chi\chi H_3} = \frac{m_{H_3}^2}{v_S}\,. \tag{2.48}$$

Thus, in this limit the DM particle χ only interacts with the singlet state H_3. Since a pure gauge-singlet scalar does not couple directly to SM fermions or gauge bosons and acquires such couplings only via mixing with the Higgs doublet fields, the absence of doublet admixtures in H_3 implies that both χ and H_3 form a decoupled dark sector whose interactions with the visible sector are switched off (see also section 2.5.2 for a more detailed discussion of

JHEP04(2026)038

the $H_i f\bar{f}$ couplings). As such, departures from this parameter configuration have to be considered in order to enable the standard freeze-out scenario for the production of the DM relic abundance in agreement with observations. Staying in the alignment limit, these can be generated by mixing the singlet state H_3 with the second CP-even state H_2 and/or by mixing the singlet state H_3 with the CP-odd state H_4 under the presence of CP-violation. For instance, setting $\alpha_3 \neq 0$ and keeping the other mixing angles as before, both H_2 and H_3 share a non-zero component of the singlet field, and one finds

$$i\Gamma_{\chi\chi H_{1,4}} = 0\,, \quad i\Gamma_{\chi\chi H_2} = \frac{m_{H_2}^2 s_{\alpha_3}}{v_S}\,, \quad i\Gamma_{\chi\chi H_3} = \frac{m_{H_3}^2 c_{\alpha_3}}{v_S}\,. \tag{2.49}$$

Since in this case both CP-even states H_2 and H_3 couple to fermions and gauge bosons, the freeze-out mechanism can efficiently proceed via these two states without modifications to the couplings of the SM-like Higgs boson H_1. On the other hand, if mixing is considered via $\alpha_5 \neq 0$ (with $\alpha_3 = \alpha_4 = 0$), then the states H_3 and H_4 are CP-odd and both share a singlet admixture, and one finds for the couplings to the DM state

$$i\Gamma_{\chi\chi H_{1,2}} = 0\,, \quad i\Gamma_{\chi\chi H_3} = \frac{m_{H_3}^2 c_{\alpha_5}}{v_S}\,, \quad i\Gamma_{\chi\chi H_4} = \frac{m_{H_4}^2 s_{\alpha_5}}{v_S}\,. \tag{2.50}$$

This opens up the interesting possibility that the DM annihilation proceeds mainly via a CP-odd Higgs-portal which is not possible for pseudo-Nambu-Goldstone (pNG) DM if the Higgs sector respects the CP symmetry.

The special feature of the cS2HDM is that the DM state χ acts as a pNG boson under a softly-broken global U(1) symmetry. As a pNG boson, the on-shell interactions of χ with the neutral Higgs bosons H_i are proportional to the momentum squared of H_i. In ref. [13] it was shown that this leads to a cancellation of the scattering process of χ on nucleons in the limit of vanishing momentum transfer. As a consequence, for non-relativistic pNG DM the scattering rates at direct detection experiments are highly suppressed. This opens up parameter space regions and DM masses that can be probed by the LHC, where in other models the possibility of a detection of DM at the LHC is largely excluded by direct-detection experiments. Thus, the model put forward here is especially motivated to serve as an LHC benchmark model for future DM searches. Still, since the global U(1) symmetry acting on the singlet field is softly broken, the cancellation mechanism is not exact, and radiative corrections from diagrams with χ in the loops generate contributions to the DM-nucleon scattering that do not vanish in the limit of vanishing momentum exchange.[8] The impact of the radiative corrections, and how we take them into account in order to confront the model with the constraints from direct-detection experiments, is discussed in section 3.4.2.

2.5 CP-violation

The model contains different sources of CP-violation both in the scalar and in the Yukawa sector. The CP-violation can physically manifest itself at low-energy experiments, most notably in the form of electromagnetic dipole moments (EDMs), or at higher energies at collider experiments like the LHC or LEP in the production and decay of the Higgs bosons.

[8] Finite-momentum contributions have been shown to be too small to generate detectable scattering cross sections [50] and are therefore not considered here.

JHEP04(2026)038

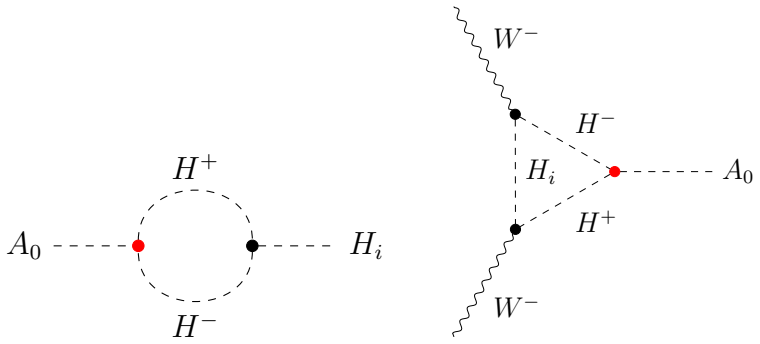

Figure 1. Left: one-loop self-energy diagram that gives rise to a CP-violating mixing between A_0 and H_i under the presence of a bosonic CP-violating coupling $A_0 H^+ H^-$. Right: one-loop diagram that gives rise to a coupling between a seemingly CP-odd state A_0 and the W boson under the presence of the same CP-violating coupling considered in the left diagram. See text for details.

2.5.1 CP-violation in the scalar potential

In the scalar sector, and using the set of input parameters introduced in section 2.3, one can impose CP-violation in two different ways. The first possibility is to choose the mixing angles α_i in such a way that there is a mixing between at least one of the CP-even fields φ_1 or φ_2 and the CP-odd field A_0 (see discussion in section 2.1). If a CP-violating mixing is present in the scalar sector, the CP-violation manifests itself phenomenologically in various ways. For instance, at least two neutral scalars H_i possesses couplings to fermions f that contain both a CP-even component $H_i f \bar{f}$ and a CP-odd component $\mathrm{i} H_i f \gamma_5 \bar{f}$, giving rise to charge-conserving but parity (P)-violating interactions [51]. In addition, purely bosonic CP-violating interactions are generated. For instance, one finds in general that the couplings $H_i H_j Z$ exist for all four neutral Higgs bosons $i = 1, 2, 3, 4$ with $j \neq i$, which is a P-even but CP-violating phenomenon [51]. On the other hand, one can remove the CP-violating mixing of the scalar fields by choosing the mixing angles in such a way that the CP-odd state A_0 is a mass eigenstate and does not mix with the other fields. This can be achieved, for example, by setting

$$\alpha_4 = 0, \pi, -\pi\,, \quad \alpha_5 = 0, \pi, -\pi\,, \quad \alpha_6 = 0, \pi, -\pi \quad \Rightarrow \quad R_{i,4} = R_{4,i} = \pm\delta_{i4}\,, \quad i = 1, 2, 3, 4\,. \tag{2.51}$$

Then, only a mixing between the three CP-even fields $(\varphi_1, \varphi_2, \varphi_S) \to (H_1, H_2, H_3)$ remains that is parametrized in terms of the mixing angles α_1, α_2 and α_3, and the state $H_4 = A_0$ does not mix with the other mass eigenstates. Here it should be noted that at the loop level CP-violating couplings give in general rise to a mixing between the states $H_{1,2,3}$ and the state H_4, such that the states $H_{1,2,3}$ and H_4 should only be understood as approximate CP-even and CP-odd eigenstates, respectively, see also the discussion below.

Even if the CP-violating mixing in the scalar sector is removed (at the classical level) by choosing the mixing angles according to eq. (2.51), the model still allows for the presence of CP-violation by setting $\lambda_5^{\mathrm{Im}} \neq 0$. In this case, using the free parameters shown in eq. (2.46), one finds CP-violation only in scalar interactions, whereas all couplings of the scalars to the fermions and gauge bosons are in agreement with the predictions of a CP conserving model. For instance, the state A_0 acts as a pseudoscalar in its interactions with SM particles, i.e. it

JHEP04(2026)038

couples to fermions with a CP-odd coupling $A_0 f\gamma_5 \bar{f}$, and its couplings to gauge bosons are absent. Nevertheless, it also features a coupling to the charged scalars of the form

$$\mathrm{i}\Gamma^{(0)}_{A_0H^+H^-} = \frac{v\lambda_5^{\mathrm{Im}}}{2c_\beta s_\beta}\,, \tag{2.52}$$

which is a coupling that is P-even but CP-violating. Here it should be noted that this purely *bosonic CP-violation* resulting from $\lambda_5^{\mathrm{Im}} \neq 0$ leaks into the other couplings of the Higgs bosons and in their mixing among each other at the radiative level. Another purely scalar CP-violating interaction that is generated in this case are $A_0H_iH_j$ interactions. In general, due to the mixing of the states H_i the corresponding couplings have a complicated form. However, in the alignment limit defined in eq. (2.26), in combination with the absence of CP-violating mixings by setting $\alpha_4 = \alpha_5 = 0$, the couplings are non-vanishing only for the states H_2 and H_3 and given by

$$\mathrm{i}\Gamma^{(0)}_{A_0H_2H_2} = \frac{c_{\alpha_3}^2 v\lambda_5^{\mathrm{Im}}}{s_{2\beta}}\,, \quad \mathrm{i}\Gamma^{(0)}_{A_0H_2H_3} = \frac{s_{\alpha_3}c_{\alpha_3} v\lambda_5^{\mathrm{Im}}}{s_{2\beta}}\,, \quad \mathrm{i}\Gamma^{(0)}_{A_0H_3H_3} = \frac{s_{\alpha_3}^2 v\lambda_5^{\mathrm{Im}}}{s_{2\beta}}\,. \tag{2.53}$$

As a result of the CP-violating scalar vertices $A_0H^+H^-$ and $A_0H_iH_j$ at tree level, also other forms of CP-violating interactions are generated via quantum corrections. Already at one-loop level, the self-energy diagram depicted in figure 1 induces a CP-violating mixing between a seemingly CP-even state H_i and the seemingly CP-odd state A_0. Moreover, the Feynman diagram on the right-hand side induces a coupling of A_0 to the W boson which would not be allowed for a pure pseudoscalar. Taking such radiative effects into account in the mixing between the scalar fields would require a complete renormalization of the scalar potential, which lies beyond the scope of this paper, and is not considered in our numerical discussion. However, we do take into account the CP-violating scalar couplings in the (tree-level) computation of the partial decay widths of the Higgs bosons, as these couplings open up novel decay modes that would be impossible in a CP-conserving model.

2.5.2 CP-violation in the Yukawa sector

Imposing NFC forbids sources of CP-violation in the Yukawa sector of 2HDMs. Instead, we impose in our analysis the less restrictive flavour alignment. This allows for three additional CP-violating phases in the Yukawa sector. We parametrize the CP-violation by treating the flavour alignment parameters ξ_u, ξ_d and ξ_ℓ as potentially complex parameters. If one or more of these three parameters has an imaginary part, there is CP-violation in the Yukawa sector, which then gives rise to CP-violating $H_i f\bar{f}$ interactions. The corresponding couplings can be written at leading order as

$$\begin{aligned}
\mathrm{i}\Gamma^{(0)}_{H_if\bar{f}} &= \Gamma_{H_if\bar{f}} + \mathrm{i}\gamma_5\tilde{\Gamma}_{H_if\bar{f}}\,,\\
\Gamma_{H_if\bar{f}} &= \frac{m_f\left[(|\xi_f|^2c_\beta + \xi_f^{\mathrm{Re}}s_\beta)R_{i1} + (\xi_f^{\mathrm{Re}}c_\beta + s_\beta)R_{i2} - \xi_f^{\mathrm{Im}}R_{i4}\right]}{v\left[|\xi_f|^2c_\beta^2 + s_\beta^2 + \xi_f^{\mathrm{Re}}s_{2\beta}\right]}\,, \qquad (2.54)\\
\tilde{\Gamma}_{H_if\bar{f}} &= \frac{m_f\left[-\xi_f^{\mathrm{Im}}s_\beta R_{i1} + \xi_f^{\mathrm{Im}}c_\beta R_{i2} + \left((1-|\xi_f|^2)\frac{s_{2\beta}}{2} + \xi_f^{\mathrm{Im}}c_{2\beta}\right)R_{i4}\right]}{v\left[(\xi_f^{\mathrm{Im}}c_\beta)^2 + (\xi_f^{\mathrm{Re}}c_\beta + s_\beta)^2\right]}\,. \qquad (2.55)
\end{aligned}$$

JHEP04(2026)038

CP-violation is present in the couplings of the Higgs bosons to fermions if at least one scalar H_i features a coupling in which both $\Gamma_{H_i f\bar{f}} \neq 0$ and $\tilde{\Gamma}_{H_i f\bar{f}} \neq 0$. In our model this effect can arise from two independent sources: (1) if there is CP-violation in the scalar sector such that $R_{i4} \neq 0$ for $i = 1, 2, 3$, see the last terms in eq. (2.54) and eq. (2.55). (2) if there is CP-violation in the Yukawa sector such that ξ_f is a complex number, see the first two terms in eq. (2.54) and eq. (2.55). It should also be noted that in the alignment limit the expression shown in eq. (2.55) yields $\tilde{\Gamma}_{H_1 f\bar{f}} = 0$ for the SM-like Higgs boson H_1, irrespective of non-zero values of ξ_f^{Im}, and only one of the other BSM Higgs bosons obtains CP-violating couplings to fermions. It is useful to define so-called κ-factors that are given by normalizing the CP-even and CP-odd components of the $H_i f\bar{f}$ couplings to the CP-even coupling of a SM Higgs boson of the same mass, i.e.

$$\Gamma_{H_i f\bar{f}} = \frac{m_f}{v}\kappa_i^f \,, \quad \tilde{\Gamma}_{H_i f\bar{f}} = \frac{m_f}{v}\tilde{\kappa}_i^f \,. \tag{2.56}$$

Hence, in the alignment limit defined in eq. (2.26) one finds $\kappa_1^f = 1$ and $\tilde{\kappa}_1^f = 0$ for the SM-like state H_1, $\kappa_{2,3}^f \neq 0$ and $\tilde{\kappa}_{2,3}^f = 0$ for the second CP-even doublet and the singlet states H_2 and H_3, and $\kappa_4^f = 0$ and $\tilde{\kappa}_4^f \neq 0$ for the CP-odd state H_4.

We end this discussion by noting that the presence of sources for CP-violation in the scalar sector and in the Yukawa sector allows for cancellations in the theoretical predictions of the EDMs between the contributions from both sectors [52]. As a consequence, compared to models with NFC in which the Yukawa sector is CP conserving, models with flavour alignment have more freedom to accommodate sizable CP-violating couplings of the Higgs bosons without being in conflict with experimental upper limits on the EDMs. We will discuss this in more detail in section 3.5.

2.6 Comments on the early universe

The cS2HDM predicts a phenomenologically viable DM candidate while also containing all required ingredients to realize EW baryogensis. Here, the strong constraints from the non-observation of the eEDM can be avoided via a cancellation between CP-violating effects between the Higgs sector and the Yukawa sector, as will be illustrated in specific parameter planes below. The strong constraints from DM direct detection experiments are evaded due to the pNG nature of the DM and the strongly suppressed DM-nucleon interactions, see discussion above. Although it is not the main focus of this paper, we briefly comment on general cosmological aspects of the model and possible phenomenological consequences from the thermal history of the model in the early universe.

Regarding the DM sector, the most natural production mechanism of the DM in the early universe proceeds via the freeze-out mechanism [53]. For temperatures of the order of the DM mass, assumed to be of the order of the EW scale here, the DM state χ is in thermal equilibrium with the particles from the visible sector by means of the Higgs-portal interactions. After the temperature of the universe drops significantly below the DM mass, the portal interaction rate falls below the expansion rate of the universe, at which moment the number density of the DM effectively freezes out. The resulting relic abundance of DM depends on the mass of the DM, m_χ, the masses m_{H_i} of the Higgs bosons acting as mediators between the dark and the visible sector, and the size of the portal couplings λ_9, λ_{10} and

JHEP04(2026)038

λ_{11}, see eq. (2.1). We note here that in our parametrization only the real part of λ_{11} is an input parameter, whereas λ_9, λ_{10} and $\lambda_{11}^{\mathrm{Im}}$ are derived parameters according to eq. (2.42), eq. (2.43) and eq. (2.44), respectively.

Modifications from the usual freeze-out mechanism have to be considered in special corners of the parameter space. For instance, if the DM mass is approximately equal to half the mass of one of the Higgs bosons, the DM annihilation is resonantly enhanced. To predict a relic abundance in agreement with the Planck measurement then requires strongly suppressed portal couplings. This can give rise to the effect of *early kinematic decoupling* that should be taken into account for an accurate prediction for the DM relic abundance [54]. Early kinematic decoupling of pNG DM has been studied recently in ref. [55]. Parameter space regions where the DM mass is set to be roughly equal to the mediator mass can be used to evade the limits from DM direct-detection experiments, because the small portal couplings also reduce the scattering rates. In our model, however, the scattering rates are momentum-suppressed already due to the pNG nature, such that it is not necessary to consider resonance regions with $m_\chi \approx m_{H_i}/2$ for a viable DM phenomenology. We therefore do not take into account the effect of early kinematic decoupling here. Another alternative process for the production of the DM in the early universe consists of the freeze-in mechanism [56], where the interaction rate between the DM and the ordinary matter is so low that the DM particle is never in thermal equilibrium with the visible sector. The DM is typically assumed to be produced via the decay of a heavier particle that is in equilibrium with the thermal bath. In our model the portal couplings are related to the EW interactions, and thus, in the absence of additional symmetries restricting the Higgs-portal interactions, are significantly too large to accommodate the freeze-in mechanism. We will therefore not consider the freeze-in of DM here.

A strong first-order EW phase transition in the early universe is necessary for the realization of EW baryogensis, which seeks to explain the matter-antimatter asymmetry of the universe. The model considered here is an extension of the 2HDM, such that it can accommodate an EW phase transition in a manner similar to the 2HDM. However, compared to the most studied $\mathbb{Z}_2$-symmetric 2HDM with CP-violation, usually denoted C2HDM in the literature, our model offers additional advantages. The stringent experimental limits on CP-violation in the scalar sector can be mitigated through potential cancellations with CP-violating couplings in the Yukawa sector. Furthermore, constraints from LHC searches for additional Higgs bosons can be relaxed if the BSM Higgs bosons decay with a sizable branching fraction invisibly into two DM scalars. This allows for a lighter BSM Higgs boson spectrum, which would strengthen the EW phase transition and enhance the resulting gravitational wave signal from the transitions. We leave a detailed discussion of the thermal history of the model, the possible patterns of cosmological phase transitions and the associated gravitational wave signals for future work.

3 Constraints

The parameter space of the model is subject to various theoretical and experimental constraints. In the following, we will discuss the constraints that we apply in our numerical analysis, starting with the theoretical requirements that we have imposed.

JHEP04(2026)038

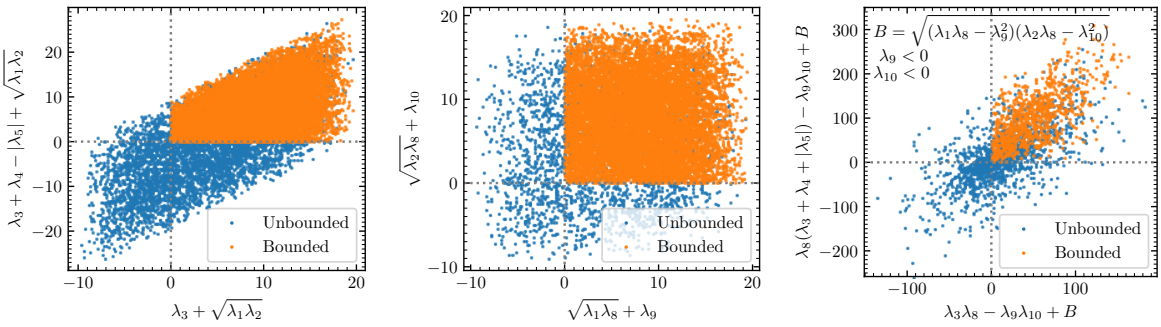

Figure 2. Set of points without (with) vacuum stability constraints in blue (orange) in three different plane projections. The points are obtained in a limit where analytical conditions are available [59]. The plot shows that in this limit our strategy to obtain the conditions numerically works.

3.1 Vacuum stability

We verify if the scalar potential is bounded from below in order to ensure that the EW vacuum can be stable. While in simpler extensions of the SM by a second Higgs doublet and/or a real scalar singlet analytic conditions can be found that can be used to determine whether the scalar potential is bounded from below, analytic conditions are not avalaible in this model due to the additional terms present in the scalar potential and the correspondingly larger number of parameters. We therefore apply a numerical method to check for the behaviour of the potential for very large field values.

To this end, we expressed the quartic part of the potential in terms of gauge-invariant bilinears

$$|\Phi_1|^2 = \frac{h_1^2}{2}, \quad |\Phi_2|^2 = \frac{h_2^2}{2}, \quad |\Phi_S|^2 = \frac{h_S^2}{2}, \quad \Phi_2^\dagger\Phi_1 = \rho e^{-i\eta}\frac{h_1 h_2}{2}, \Phi_1^\dagger\Phi_2 = \rho e^{i\eta}\frac{h_1 h_2}{2}. \tag{3.1}$$

This reduces the number of field dimensions that have to be considered to five, parametrized by the five real parameters h_1, h_2, h_S, ρ and η. Note here that the possible ranges of the parameters are restricted: $0 \leq \rho \leq 1$ and $-\pi \leq \eta \leq \pi$, and h_1, h_2 and h_S are non-negative. Using these invariants, the quartic part of the scalar potential is given by

$$\begin{aligned} V_{\text{quartic}} = &\frac{\lambda_1}{8}h_1^4 + \frac{\lambda_2}{8}h_2^4 + \frac{\lambda_3}{4}h_1^2h_2^2 + \frac{\lambda_4}{4}h_1^2h_2^2\rho^2 + \frac{\lambda_8}{8}h_S^4 + \frac{\lambda_9}{4}h_1^2h_S^2 + \frac{\lambda_{10}}{4}h_2^2h_S^2 \\ &+ \frac{1}{4}h_1^2h_2^2\rho^2(c_{2\eta}\lambda_5^{\text{Re}} - s_{2\eta}\lambda_5^{\text{Im}}) + \frac{1}{2}h_1^3h_2\rho(c_\eta\lambda_6^{\text{Re}} - s_\eta\lambda_6^{\text{Im}}) \\ &+ \frac{1}{2}h_1h_2^3\rho(c_\eta\lambda_7^{\text{Re}} - s_\eta\lambda_7^{\text{Im}}) + \frac{1}{2}h_1h_2h_S^2\rho(c_\eta\lambda_{11}^{\text{Re}} - s_\eta\lambda_{11}^{\text{Im}}). \end{aligned} \tag{3.2}$$

The scalar potential is unbounded if there are values of the invariants for which $V_{\text{quartic}} < 0$, and it is bounded from below otherwise. We numerically verified this by minimizing V_{quartic} and checking the sign of V_{quartic} at the deepest minimum that is found. Since the possible ranges of the invariants is finite, we used a constrained minimization method called bound optimization by quadratic approximation [57] as implemented in the public Fortran package `PowellOpt` [58]. In order to improve the reliability of this procedure, we applied the minimizer up to ten times with different initial seed values for the invariants for each considered parameter point.

JHEP04(2026)038

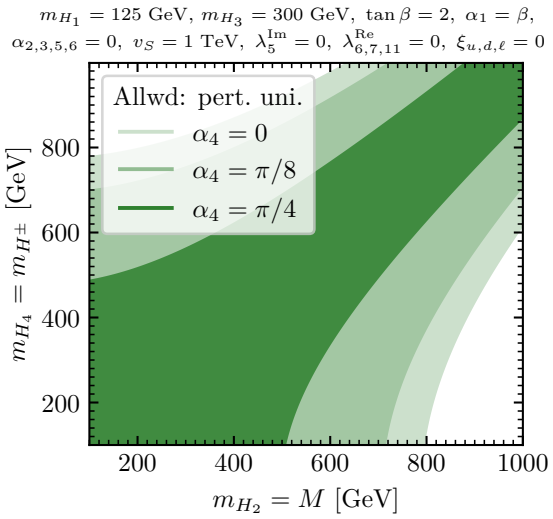

Figure 3. Allowed parameter space after imposing perturbative unitarity constraints in a projection plane with $m_{H_2} = M$ on the horizontal axis and $m_{H_4} = m_{H^\pm}$ on the vertical axis, keeping all other parameters fixed as shown on top of the plot. Different tones of green correspond to three values of the CP-violating mixing angleα_4.

In order to test the reliability of this numerical approach, we generated parameter points in a limiting case for which analytical conditions are known to verify the boundedness of the potential. In this limit all quartic couplings λ_i are set to be real, and we set $\lambda_6 = \lambda_7 = \lambda_{11} = 0$.[9] By scanning over the remaining λ_i in a range from -10 to 10 (without considering any other constraint), we randomly generated 10,000 parameter points that feature a bounded scalar potential according to our numerical procedure. Subsequently, we generated 10,000 parameter points in the same way that are predicted to feature an unbounded potential. The two sets of parameter points are shown in figure 2 in orange and blue colour, respectively, in three different parameter planes. The axes of the three plots show different combinations of the quartic scalar couplings that according to ref. [59] should be positive if the potential is bounded. One can observe that all orange points lie within the upper right quadrant. This demonstrates that our numerical method is able to reliably predict the boundedness of the potential for all 10,000 parameter points in agreement with the analytical conditions in the considered limit.

3.2 Perturbative unitarity

Upper limits on the absolute values of the quartic scalar couplings λ_i can be found on the basis of unitarity. To this end, we apply so-called perturbative unitariy constraints at tree level in the high-energy limit in which only scalar self interactions have to be considered. We require that the absolute values of the eigenvalues of the $2 \to 2$ scalar scattering matrices are smaller than 8π. The scalar scattering matrices in the high-energy limit for neutral, charged and doubly-charged final and initial states are matrices of dimension 25, 12 and 3, respectively. We do not display the elements of these matrices here for brevity, but they can be found in the module `perturbative_unitarity` of our code.

[9] The scalar potential then resembles the one of the so-called Next-to 2HDM (N2HDM) [60].

JHEP04(2026)038

The perturbative unitarity requirement gives rise to upper limits on the absolute values of the scalar quartic couplings λ_i. This, in turn, results in upper limits on the mass splitting between neutral scalar states that are mixed with each other, and also on the splitting between the masses of the scalars and the two BSM mass scales $M = m_{12}^2/(s_\beta c_\beta)$ and v_S contained in the model. In figure 3 we show the impact of the perturbative unitarity constraints in a benchmark plane where we vary $m_{H_2} = M$ on the horizontal and $m_{H_4} = m_{H^\pm}$ on the vertical axis, keeping all other parameters fixed as shown on top of the plot. Such a parameter plane is of interest in the context of realizing a strong first-order EW phase transition, in which the strengths of the transition is typically correlated with sizable mass splitting between two neutral scalar states [61–64].[10] The green shaded regions indicate the allowed parameter regions for different values of the CP-violating mixing angle α_4. One can see that the possible amount of mass splitting between H_2 and H_4 becomes more constraint the larger the value of α_4, i.e. the more CP-violating mixing is present in the scalar sector (see also ref. [68] for a detailed discussion). Since the model studied here allows for CP-violation without non-zero values for the CP-violating mixing angles, it would be interesting to investigate whether in this model one can realize a first-order EW phase transition in or close to the alignment limit with a transition strength and an amount of CP-violation that are sufficient to account for the observed baryon asymmetry of the universe via EW baryogenesis, while at the same time being in agreement with the experimental upper limits on the eEDM. We leave this analysis for future work.

One should note that using the limit of 8π on the absolute values of the eigenvalues of the scattering matrices still allows for large values of individual λ_i couplings which (depending on the observables of interest) may lie outside of the region in which the model can be treated perturbatively. Additional constraints can be imposed on the absolute values of the parameters λ_i themselves. A typical choice is to require $|\lambda_i| < 4\pi$ in order to ensure perturbativity. It should be noted that such conditions depend on the numerical prefactors of the different terms contained in the scalar potential, whereas the perturbative unitarity conditions derived from the scattering matrix are independent of these prefactors. Furthermore, such a limit can also be too restrictive, excluding in principle allowed parameter regions with potentially interesting phenomenology. Thus, in order to be conservative regarding the exclusion of parameter points, and since we present a broad phenomenological study of the model instead of focusing on a particular observable, we do not include additional perturbativity limits in our numerical analysis.

3.3 Collider constraints

We now turn to the experimental constraints, starting with the ones stemming from measurements at colliders. These comprise the LHC cross-section measurements of the detected Higgs boson at 125 GeV, cross-section limits from searches for additional Higgs bosons at LEP and the LHC, measurements of flavour-physics observables which are especially sensitive to the presence of the charged Higgs bosons, and measurements of electroweak precision observables (EWPO).

[10] Strong first-order EW phase transition, although of substantially smaller strengths, can also be realized without large mass splittings between the neutral Higgs bosons [65–67].

JHEP04(2026)038

3.3.1 LHC Higgs-boson measurements

After the LHC Run 2 at 13 TeV we have entered the era of precision measurements of the 125 GeV Higgs boson. The Higgs boson has now been produced and detected in several different production and decay channels. Models with additional Higgs bosons, as the one considered here, have to accommodate a Higgs boson at 125 GeV that predicts the measured signal rates in agreement with the LHC measurements. Since the measured cross sections are so far compatible with the predictions for a Higgs boson contained in the SM, extended Higgs sector models have to feature a Higgs boson that approximately resembles a SM Higgs boson.

In the model considered here, there are four different neutral scalar states that can play the role of the detected Higgs boson.[11] We test whether a parameter point is consistent with the current LHC data by using `HiggsSignals` [69–71] contained in the software package `HiggsTools v.1.2` [41]. We perform a χ^2 fit comparing the theoretically predicted signal rates (see section 3.3.2 for a discussion of the theory predictions) of the scalar at 125 GeV against the experimentally measured values, taking into account total cross section measurements and the measurements published in the framework of the simplified template cross sections. We use the `HiggsSignals` data set with version number 1.1 which contains the currently most precise Run 2 measurements. We reject a parameter point if the total χ^2 from `HiggsSignals` is larger than the one obtained assuming a SM Higgs boson by 6.18 units, i.e. if the fit result of the parameter point is worse compared to the SM fit result at a confidence level of more than 2σ in joint estimation of two parameters.

As already mentioned in section 2.1, the LHC Higgs data drives the model towards the alignment limit. If this limit is imposed, the state H_1 will feature couplings that are identical to the ones of a SM Higgs boson. One way to enforce the alignment limit is given in eq. (2.26). Applying the constraints from the Higgs-boson measurements severely constraints the allowed values of the six mixing angles α_i. Hence, a random scan over these angles would be highly inefficient as it would give rise to tiny fractions of allowed parameter points. Therefore, in our analysis we will often start from a valid parameter point in the alignment limit and then investigate to what extend departures from the alignment limit are still allowed. The modifications to the properties of the state at 125 GeV compared to the SM can arise in several ways in our model, e.g. from a misalignment of the mixing of the doublet state away from the so-called Higgs basis [72], from a singlet admixture, or from CP-violating effects that, as we remind the reader, can be present in this model even in the alignment limit.

3.3.2 BSM Higgs-boson searches

While a vast search programme for additional scalar particles is ongoing at the LHC, so far only one Higgs boson has been detected. Hence, the BSM Higgs bosons predicted by the model have to respect the cross-section limits from the various collider searches that have been performed at the LHC, but also at previous colliders like LEP or Tevatron. We verify whether a parameter point is in agreement with all existing cross section limits by using `HiggsBounds` [73–76] which is now incorporated in `HiggsTools`. For the full set of experimental results implemented in the `HiggsBounds` data set with version number 1.4

[11] We do not consider the possibility that there are more than one Higgs boson with masses of about 125 GeV whose combined signal rates give rise to the experimentally measured values at the LHC.

JHEP04(2026)038

we identify the most sensitive search for each BSM Higgs boson based on the expected experimental sensitivity. For the selected searches, we apply the observed cross section limits at 95% confidence level. If one or more of the BSM Higgs bosons features a cross section that is larger than the experimentally observed limit, we regard the corresponding parameter point as excluded.

In order to use `HiggsBounds` (and `HiggsSignals` for the test against the LHC Higgs data of the detected Higgs boson) one needs the cross sections and partial decay widths of all the neutral and charged Higgs bosons contained in the model. We obtain the cross sections at the LHC and LEP as functions of effective coupling coefficients by using the package `HiggsPredictions` of `HiggsTools` For the neutral scalars H_i, the effective coupling coefficients correspond to the so-called κ-factors which are defined as the couplings normalized to the prediction of a SM Higgs boson of the same mass. For the charged Higgs bosons, the process $pp \to H^{\pm}tb$ is currently the only one for which LHC searches exist. We compute the cross sections at 13 TeV as functions of the couplings $t\bar{b}H^-$ and $\bar{t}bH^+$ using `HiggsPredictions`. For the scalar DM state, we only take into account its production via decays of the neutral scalars. This can give rise to final states with large missing transverse energy and/or mono-Higgs or mono-jet final states.

We compute the partial decays of the Higgs bosons using an extension of the public code `HDECAY` [39, 40]. This code was originally developed for the SM and the minimal supersymmmetric extension of the SM and later extended to the 2HDM and other BSM models. We extended it to include the additional particles and their interactions predicted in the model considered here. The resulting Fortran library `CS2HDECAY` will be made publicly available contained in the Fortran package `cs2hdmTools`. With this package and its interfaces to `HiggsTools` and `C2SHDECAY` the parameter points of the model can be readily confronted with the current LHC measurements and cross section limits.

3.3.3 Flavour-physics observables

Flavour-physics observables tightly constrain models with more than one Higgs doublet. In the SM FCNCs are naturally suppressed, whereas this suppression is lost in general under the presence of a second Higgs doublet field.

In order to comply with the corresponding experimental limits, we employ the flavour alignment in the Yukawa sector as discussed in section 2.2. Since the flavour alignment is not enforced by a symmetry, small deviations from the flavour alignment are generated at loop level that would ultimately lead to FCNCs. However, it has been shown that these radiative flavour-misalignment effects are sufficiently small to not be in conflict with existing experimental limits on FCNCs [77].

In the scalar sector, FCNCs are generated at loop level even under the assumption of flavour alignment if at least one of the quartic scalar couplings that break the $\mathbb{Z}_2$ symmetry under which the doublet fields transform as $\Phi_1 \to -\Phi_1$ and $\Phi_2 \to \Phi_2$ are non-zero. This mainly concerns the parameters λ_6 and λ_7. Hence, in order to suppress FCNCs we set $\lambda_6^{\mathrm{Re}} = \lambda_7^{\mathrm{Re}} = 0$ in our numerical analysis, and we note that their imaginary components are typically suppressed because they violate CP. A third $\mathbb{Z}_2$-breaking term proportional to λ_{11} is present that can induce dangerous FCNCs at loop level. Since in the corresponding

JHEP04(2026)038

potential term the singlet field Φ_S appears, its contribution to FCNCs is milder, potentially only relevant if the mixing between the doublet fields and the singlet field are sizable and the portal couplings are large. As for λ_6 and λ_7, in a conservative approach to avoid the appearance of FCNCs, we set $\lambda_{11}^{\text{Re}} = 0$. The imaginary part λ_{11}^{Im} is a derived parameter in our analysis and not generically zero, but its impact on FCNCs is suppressed in a two-fold way due to the CP breaking and the singlet admixture required to induce FCNCs from this parameter.

Under the assumptions discussed above, the appearance of FCNCs in this model reduces to the case of the 2HDM with softly-broken $\mathbb{Z}_2$ symmetry, where the presence of the charged scalars gives rise, most importantly, to radiative decays of B mesons. This leads to strong constraints from measurements of $b \to s\gamma$ transitions, giving rise to a lower limit on the mass of the charged scalars of $m_{H^\pm} \gtrsim 500\,\text{GeV}$ in the type II 2HDM [49, 78, 79], and to a lower limit on $\tan\beta$ that, depending on the value of $m_{H^\pm}$ ranges between $\tan\beta \gtrsim 2$ for $m_{H^\pm} = 200\,\text{GeV}$ and $\tan\beta \gtrsim 1$ for $m_{H^\pm} = 1\,\text{TeV}$ for all Yukawa types. Similar, but currently slightly weaker, limits on $\tan\beta$ result from measurements of leptonic B-meson decays, $B_s^0 \to \mu^+\mu^-$ and $B^0 \to \mu^+\mu^-$. We consider these limits from the 2HDM in our analysis whenever we consider values of the flavour-alignment parameters that result in one of the four Yukawa types of the $\mathbb{Z}_2$-symmetric 2HDM, see table 1. For all other cases, the application of experimental bounds from flavour-physics observables requires a dedicated computation which is beyond the scope of this paper, and thus left for future work.

3.3.4 Electroweak precision observables

In the SM the ρ parameter [80]

$$\rho = \frac{M_W^2}{M_Z^2 c_w^2}\,, \tag{3.3}$$

with c_w the cosine of the weak mixing angle, is predicted to be equal to one at the classical level as a consequence of the custodial symmetry of the Higgs potential. This prediction is confirmed by experiment at the sub-permille level [81], making the ρ parameter one of the most important probes of new physics. In models with extended scalar sectors where several scalar fields obtain a vev, as considered here, the predictions for the ρ parameter are in general different from one. However, in extensions of the SM that contain additional scalar fields that are either gauge-singlets or SU(2) doublets with hypercharge $\pm 1/2$, the SM prediction $\rho = 1$ is maintained at the classical level, and modifications to the ρ parameter are only generated via radiative corrections. In this case, modifications to the ρ parameter are typically parametrized in terms of the parameter $\Delta\rho$, which is defined by [82]

$$\Delta\rho = \left[\frac{\Pi_{WW}^T(0)}{M_W^2} - \frac{\Pi_{ZZ}^T(0)}{M_Z^2}\right]_{\text{BSM}} - \left[\frac{\Pi_{WW}^T(0)}{M_W^2} - \frac{\Pi_{ZZ}^T(0)}{M_Z^2}\right]_{\text{SM}}\,, \tag{3.4}$$

where $\Pi_{WW}^T(0)$ and $\Pi_{ZZ}^T(0)$ are the transverse parts of the W-boson and Z-boson self-energies at zero external momentum, respectively, and the first and the second bracket contain the self-energies in the BSM theory under consideration and in the SM, respectively. The parameter $\Delta\rho$ is related to the oblique parameter T [83] via the relation $\Delta\rho = \alpha T$, where α is the fine-structure constant.

JHEP04(2026)038

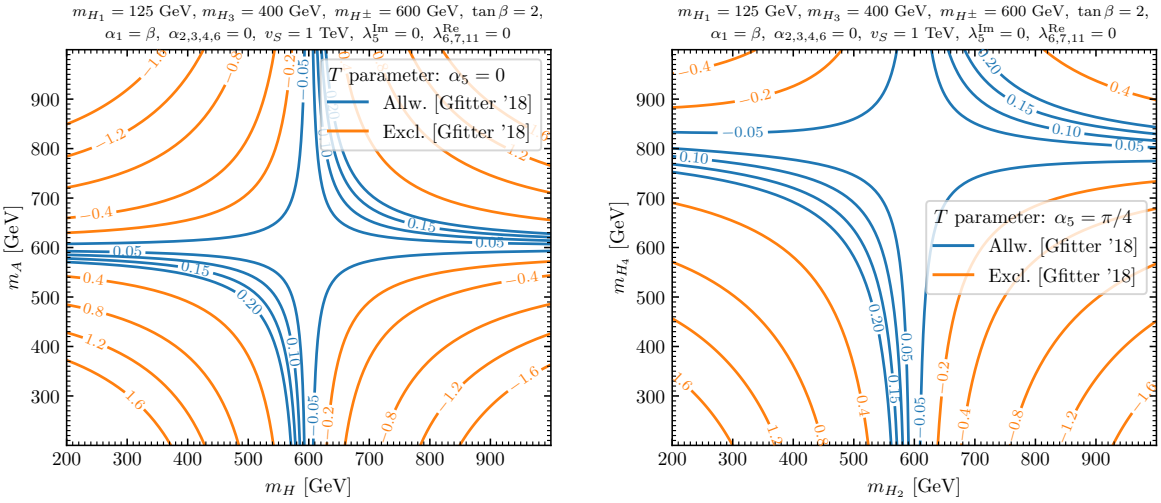

Figure 4. Left: predictions for the T-parameter in a CP-conserving scenario in the $\{m_H, m_A\}$ plane, where m_H is the mass of the second CP-even doublet Higgs state, and m_A is the mass of the CP-odd Higgs state. The mixing angles α are set according to the alignment limit given in eq. (2.26), such that the singlet field corresponding to the Higgs boson with a mass of $m_{H_3} = 400\,\text{GeV}$ is decoupled, and there is no CP-violating mixing in the scalar sector. All other input parameters are set as shown on top of the plot. The contour lines indicate fixed values of T. Blue lines correspond to values of T that are compatible with the experimentally allowed range from a global fit to EWPOs from ref. [84], see text for details, while orange lines correspond to values of the T-parameter that are outside of the experimentally allowed range. Right: the same as in the left plot, but for a scenario with CP-violation via a non-zero value of $\alpha_5 = \pi/4$. In this case, the CP-odd component of the Higgs doublet fields mixes with the singlet scalar, giving rise to two CP-mixed mass eigenstates H_3 and H_4. Since in this case there is no CP-odd eigenstate anymore, we change the axes labels to m_{H_2} and m_{H_4} instead of m_H and m_A used in the left plot.

In our model the main modifications to the EWPOs arise via weak isospin breaking generated at loop-level, giving rise to non-zero values of T. As a consequence, the two most precisely measured EWPO, the W-boson mass M_W and the leptonic effective weak mixing angle, usually denoted as $\sin^2\Theta_{\text{eff}}$, receive corrections with respect to the SM prediction, which can be used to constrain the parameter space of the model. To this end, we compute T at the one-loop level and apply the limit from the Gfitter collaboration [84] that was obtained from a global fit to various EWPOs.[12]

In figure 4 we show the predictions for the T parameter for two representative parameter planes. In the left plot, we consider the CP-conserving limit, and the mixing between the singlet state and the doublet states is zero. The neutral scalar spectrum consists of a SM-like

[12]More recent measurements of the W-boson mass performed by LHCb [85], ATLAS [86] and CMS [87] are not contained in the Gfitter 2018 analysis. However, these measurements are in good agreement with the SM and the PDG average value of M_W on which the Gfitter 2018 result is based. Hence, the new measurements performed at the LHC would not yield significant modifications to the allowed parameter space regions discussed here. On the other hand, the CDF M_W measurement published in 2022 is in significant tension with the SM [88]. While the large upwards shift in M_W in the direction of the CDF measurement can be accommodated in 2HDM [89, 90] and 2HDM + singlet models [91], we do not consider this possibility here due to the discrepancies between the CDF measurement and the LHC (and LEP) measurements.

JHEP04(2026)038

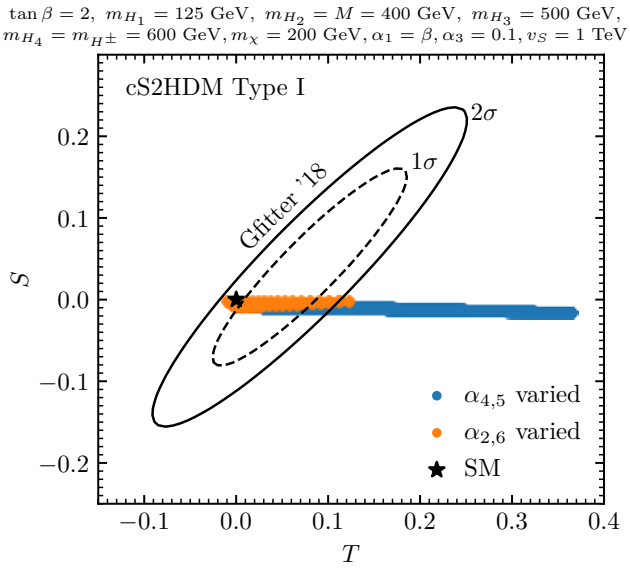

Figure 5. Predictions for the S- and the T-parameters for two scenarios with the parameters fixed as shown on top of the plot. For the blue points, the mixing angles α_4 and α_5 where varied from $-\pi/2$ to $\pi/2$, with $\alpha_2 = \alpha_6 = 0$. For the orange points, instead α_2 and α_6 were varied, while $\alpha_4 = \alpha_5 = 0$ (see main text for details). The black dashed and solid contours indicate the experimentally allowed regions in the S-T-plane at 1σ and 2σ confidence level, respectively [84]. The black star indicates the SM prediction.

Higgs boson H_1, a second CP-even Higgs boson H and a CP-odd Higgs boson A whose masses are varied between 200 GeV and 1 TeV, and a singlet Higgs boson H_3 whose mass is chosen to be 400 GeV. Finally, the mass of the charged scalars is set to $m_{H^\pm} = 600$ GeV. The remaining parameters are fixed as shown above the plot. One can observe that the values of T in agreement with the experimental data, indicated with blue contours, are confined to the parameter space regions where either H or A is approximately mass degenerate with $H^\pm$. This is the expected and known result from the 2HDM, which we here reproduce by decoupling the singlet field.

This can be compared to the right plot of figure 4, where we change the value of one of the mixing angles from $\alpha_5 = 0$ (left plot) to $\alpha_5 = \pi/4$ (right plot). This gives rise to a mixing in the scalar sector between the pseudoscalar component and the singlet component. Accordingly, we change the labels on the axes to m_{H_2} and m_{H_4} since there are no CP eigenstates anymore. As a consequence of the CP-violation, the experimentally allowed region is shifted to larger values of m_{H_4}. We observe that the T-parameter goes to zero if $m_{H_2} = m_{H^\pm}$ (as before) and if the mean of the two masses of H_3 and H_4 is approximately equal to the mass of $m_{H^\pm}$, i.e. $(m_{H_3} + m_{H_4})/2 \approx m_{H^\pm}$ (see also ref. [92]). In the latter case, the T-parameter is predicted to be in agreement with the experimental value without the presence of approximately mass-degenerate scalars, in contrast to the CP-conserving limit. This is an important difference between pure 2HDMs and models that in addition to a second Higgs doublet contain one or more gauge singlet fields with non-zero vevs.

JHEP04(2026)038

To assess the relevance of constraints from EWPOs beyond custodial-symmetry breaking effects, we have additionally evaluated the predictions for the S-parameter, which is defined as [83]

$$\frac{\alpha}{4s_w^2 c_w^2} S = \left[\frac{\Pi_{ZZ}(M_Z^2) - \Pi_{ZZ}(0)}{M_Z^2} - \left.\frac{\partial A_{\gamma\gamma}(q^2)}{\partial q^2}\right|_{q^2=0} + \frac{c_w^2 - s_w^2}{c_w s_w} \left.\frac{\partial A_{\gamma Z}(q^2)}{\partial q^2}\right|_{q^2=0} \right]_{\text{BSM}} - \left[\frac{\Pi_{ZZ}(M_Z^2) - \Pi_{ZZ}(0)}{M_Z^2} - \left.\frac{\partial A_{\gamma\gamma}(q^2)}{\partial q^2}\right|_{q^2=0} + \frac{c_w^2 - s_w^2}{c_w s_w} \left.\frac{\partial A_{\gamma Z}(q^2)}{\partial q^2}\right|_{q^2=0} \right]_{\text{SM}} . \quad (3.5)$$

Here, $\Pi_{\gamma\gamma}$ and $\Pi_{\gamma Z}$ are the transverse parts of the photon and mixed photon-Z boson self-energies, respectively, and q is the external momentum. The S-parameter measures new-physics contributions to the momentum dependence of neutral-current interactions. The cS2HDM predictions for the T- and the S-parameters at one-loop level are shown in figure 5 for two representative scenarios. In both cases, non-zero contributions arise from mass splittings among the neutral BSM scalars, if the state H_4, which is chosen to be mass degenerate with $H^\pm$, acquires CP-even admixtures and thus deviates from a purely CP-odd eigensate (see discussion above).

In the first scenario (blue points), we vary the mixing angles α_4 and α_5 in the range $[-\pi/2, \pi/2]$. Non-zero values of these two mixing angles induce CP-even components in H_4 through mixing with the doublet-like state H_2 and the singlet-like state H_3. The other free parameters of the cS2HDM are kept fixed to the values shown on top of the plot. In particular, the alignment limit is maintained by fixing $\alpha_1 = \beta$ and $\alpha_2 = \alpha_6 = 0$, such that the lightest scalar H_1 behaves as the SM Higgs boson for all blue points. In the second scenario (orange points), we instead vary α_2 and α_6, while fixing $\alpha_4 = \alpha_5 = 0$. This generates a singlet admixture and a CP-odd component in the lightest state H_1. As a consequence, its couplings to fermions and gauge bosons are modified compared to the ones of the SM Higgs boson. We therefore vary α_2 and α_6 in the range in which the constraints from LHC Higgs-boson cross section measurements are satisfied, as discussed in section 3.3.1. The experimentally allowed regions at the 1σ and 2σ confidence level are indicated by the dashed and solid black contours, respectively [84]. As can be seen, the predictions for S and T are strongly correlated in extensions of the SM with a second Higgs doublet such as the cS2HDM. Values of S that are compatible with the experimental bounds on T are in general significantly smaller than the corresponding values of T. We stress that, while showing here only the results for two specific scenarios, we have verified within our numerical discussion in section 4 that this behaviour persists across the viable parameter space of the model in our scan. Consequently, we impose only the experimental constraint on the T-parameter in the parameter scan presented in section 4.

3.4 Dark-Matter constraints

The presence of the DM scalar in our model imposes significant constraints on the parameter space due to several factors. First, the model must reproduce the experimentally observed relic abundance of DM, or at the very least, avoid predicting an overabundance that exceeds current cosmological limits. While direct detection experiments generally place stringent

JHEP04(2026)038

bounds on the interaction cross-section between the DM and nucleons, these constraints are of minor relevance in our model due to the cancellation of DM-nucleon scattering, a consequence of the pNG nature of the DM particle. Finally, indirect detection constraints arise from astronomical observations that are sensitive to DM annihilation signals.

3.4.1 Relic abundance

In our model the DM candidate χ is produced in the early universe through the thermal freeze-out mechanism. To calculate the predicted DM relic abundance, we created a model file for `FeynRules v.12.2` [93, 94], which was then used to generate the corresponding `CalcHEP` [95] files that are required to implement the model in the public code `micrOMEGAS v.5.3.41` [42, 43]. This allows us to compute the relic abundance, taking into account all relevant DM annihilation processes at leading order. We confront the theoretically predicted values for the relic abundance assuming the standard freeze-out scenario, $(\Omega h^2)_{\rm FO}$, with the experimental value $(\Omega h^2)_{\rm Planck} = 0.1200 \pm 0.0012$ obtained by the Planck collaboration by measuring the power spectrum of the cosmic microwave background [96]. We define the ratio

$$\xi_{\rm Planck} = \frac{(\Omega h^2)_{\rm FO}}{(\Omega h^2)_{\rm Planck}} \,. \tag{3.6}$$

Parameter points predicting $\xi_{\rm Planck} > 1$ overclose the universe and are regarded as excluded by the measurement of the relic abundance of DM (under the assumption of a standard cosmological history and the freeze-out mechanism). Parameter points predicting $\xi_{\rm Planck} \approx 1$ are allowed and predict the total amount of the observed relic abundance of DM. Finally, parameter points predicting $\xi_{\rm Planck} \leq 1$ can be regarded as allowed, but in order to fully account for the observed abundance of DM additional components would be required that are not contained in our model.

The presence of the pNG DM state requires that the real component of Φ_S has a non-zero vev v_S. This allows for a mixing of the neutral components of the Higgs doublets and the real singlet component, see discussion in section 2.1. As a consequence, a phenomenologically viable pNG DM state is only present if the singlet field φ_S mixes with at least one of the other neutral fields φ_1, φ_2 or A_0 from the Higgs doublets. If, on the other hand, the real singlet component is not mixed with the doublet fields, the singlet sector decouples from the visible sector, and the portal couplings required for the thermal freeze-out mechanism vanish.

In the CP-conserving limit, the portal interactions between the DM state χ and the visible matter can be confined to the CP-even part of the Higgs sector. As a consequence, if the state H_1 corresponding to the 125 GeV Higgs boson acts as a portal, the state H_1 has to have a non-zero singlet admixture, and the model predicts modifications of the couplings of the Higgs boson at 125 GeV with respect to the SM predictions. This is an important difference to models like the 2HDM+a in which the CP-even Higgs sector, and thus the Higgs boson at 125 GeV, does not act as a portal between the DM and the ordinary matter in the annihilation processes, such that no departures from the alignment limit are required.

To quantify the coupling modifications of the 125 GeV Higgs boson that are required for a prediction of the DM relic abundance equal or below the Planck measurement in a CP-conserving scenario in which the 125 GeV Higgs boson acts as a portal, we show in the

JHEP04(2026)038

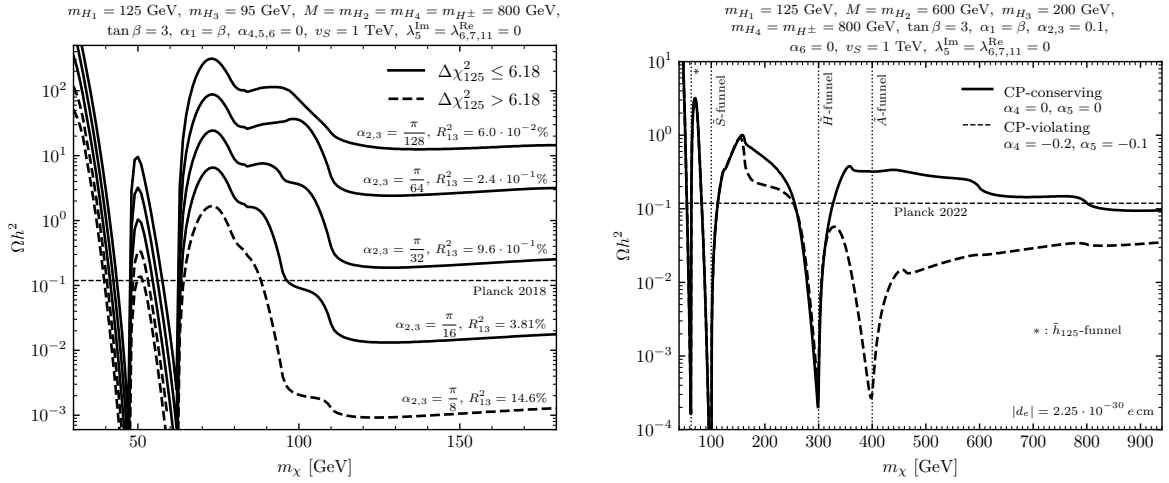

Figure 6. Left: predicted relic abundance in the CP-conserving limit with Yukawa type I with a SM-like Higs boson at $m_{h_1} = 125.1\,\text{GeV}$, a singlet-like Higgs boson at $m_{h_3} = 95\,\text{GeV}$, and the other doublet-like Higgs-bosons at $M = m_{h_2} = m_{h_4} = m_{H^\pm} = 800\,\text{GeV}$. The remaining free parameters are set as follows: $\tan\beta = 3$, $\alpha_1 = \beta$, $\alpha_{4,5,6} = 0$, $v_S = 1000\,\text{GeV}$, $\lambda_5^{\rm Im} = \lambda_6^{\rm Re} = \lambda_7^{\rm Re} = \lambda_{11}^{\rm Re} = 0$, and the mixing angles $\alpha_2 = \alpha_3$ are varied as shown in the plot. The values of R^2_{13} shown in the plot are the singlet-admixture of the SM-like Higgs boson h_1. The solid lines correspond to the regions of the DM mass m_χ compatible with the LHC Higgs-boson measurements for a given value of $\alpha_2 = \alpha_3$, whereas the dashed lines indicate regions that are excluded, see section 3.3.1 for details. The horizontal dashed line shows the experimental value of the DM relic abundance measured by Planck [96]. Right: predicted relic abundance as a function of m_χ in a scenario with CP-violation ($\alpha_4 = -0.2$, $\alpha_5 = -0.1$) and without ($\alpha_4 = \alpha_5 = 0$) CP-violation indicated with the solid and dashed lines, respectively. All other parameters are set as shown on top of the plot. The value of the electron EDM $|d_e|$ shown in the lower right corner is the one predicted for the parameter points corresponding to the dashed line, independently of the DM mass m_χ, see discussion in section 3.5. The horizontal dashed line shows the experimental value of the DM relic abundance measured by Planck, and the vertical dashed lines indicate the mass of the particle that is responsible for the main annihilation channel in the funnel regions.

left plot of figure 6 the predicted values of the relic abundance Ωh^2 as a function of the DM mass m_χ for a representative benchmark point with a singlet-like Higgs boson lighter than 125 GeV. Each line corresponds to different values of the mixing angles α_2 and α_3, where all other parameters were fixed to the values shown on top of the plot. Since $\alpha_{4,5,6} = 0$, in the limit $\alpha_{2,3} \to 0$ the singlet decouples and the portal couplings vanish, while for increasing values of α_2 and α_3 the mixing between the Higgs boson H_1 at 125 GeV and the singlet-like Higgs boson H_3 at 95 GeV increases. According to the discussion above, we observe that the predicted relic abundance becomes overall smaller when the mixing angles are increased. For the upper three lines, where the singlet admixture of H_1, given by $R^2_{13} = \sin^2\alpha_2$ here (see eq. (2.12)), is below one percent, the predicted abundance of DM is larger than the value observed by the Planck collaboration. As a result, the corresponding parameter points are excluded except for the *funnel* regions $m_\chi \approx m_{H_1}/2$ and $m_\chi \approx m_{H_3}/2$ where the annihilation is resonantly enhanced. On the other hand, for larger singlet admixtures in the SM-like Higgs boson of $R^2_{13} = 3.81\%$ and $R^2_{13} = 14.6\%$ (the lowest two lines), the predicted abundance is

JHEP04(2026)038

below the Planck value across most of the DM mass interval depicted in figure 6. However, if the singlet admixture becomes too large, the coupling modifications of the 125 GeV Higgs boson are not in agreement with the signal-rate measurements from the LHC. In the plot, we indicate the mass intervals of χ which are incompatible with the Higgs data at more than 2σ confidence level (see discussion in section 3.3.1) with dashed lines. The lowest line with a singlet component of about 15% in 125 GeV Higgs boson is shown entirely as a dashed line, indicating that all parameter points with $\alpha_{2,3} = \pi/8$ are excluded. In addition, the line for $\alpha_{2,3} = \pi/16$, corresponding to a singlet component of about 4%, is excluded for DM masses of $m_\chi \lesssim 62\,\text{GeV}$, where the invisible decay mode of the 125 GeV Higgs boson gives rise to an additional modification to the signal rates, rendering them incompatible with the LHC measurements. Assuming the absence of CP-violation in the Higgs sector, we conclude that large parts of the parameter space of the model require coupling modifications of the detected Higgs boson of a few percent in order to be compatible simultaneously with LHC Higgs-boson measurements and the Planck measurement of the DM relic abundance (taken as upper limit), apart from corners of the parameter space with tuned DM mass values in which the DM annihilation is resonantly enhanced.

This picture changes if CP-violation in the Higgs sector is present, which is demonstrated for an example scenario in the right plot of figure 6. Here, we set $\alpha_2 = 0.1$ and $\alpha_6 = 0$, such that the singlet admixture of the 125 GeV Higgs boson is $R^2_{13} = 1\%$, which is substantially below the current and near future experimental sensitivity of the LHC to modifications of the Higgs-boson signal rates, rendering the scenario well compatible with the LHC data. CP-violation in the Higgs sector is introduced with non-zero values of the two mixing angles α_4 and α_5 (dashed line), whereas there is no CP-violation if these angles are zero (solid line). The specific values $\alpha_4 = -0.2$ and $\alpha_5 = -0.1$ were chosen in order to obtain a prediction for the eEDM of $|d_e| = 2.25 \cdot 10^{-30}\ e\,\text{cm}$ that is well below the current experimental upper bounds, see the discussion in section 3.5. All other free parameters are set to the values shown above the plot. We depict the predicted DM relic abundance for both cases ($\alpha_{4,5} = 0$ and $\alpha_{4,5} \neq 0$) as a function of the DM mass m_χ. One can see that in large parts of the depicted range of m_χ both lines approximately lie on top of each other. However, at $m_\chi \approx m_{H_4}/2 \approx 400\,\text{GeV}$, the dashed line drops by several orders of magnitude in Ωh^2 below the solid line. Here, the non-zero values of α_4 and α_5 give rise to a non-zero coupling for $\chi\chi H_4$ interactions, and the DM annihilation is resonantly enhanced via s-channel annihilation with a dominantly CP-odd state H_4 in the s-channel. On the other hand, without CP-violation the coupling $\chi\chi H_4$, with H_4 being a pure CP-odd state, is absent, and the solid line remains flat in the "$\tilde{A}$-funnel" region indicated in the plot, where the tilde in the notation $\tilde{A}$ indicates that for $\alpha_4 \neq 0$ and $\alpha_5 \neq 0$ the state is only an approximate CP-odd state. This demonstrates a generic feature of the considered model: under the presence of CP-violation, the DM-portal interactions can be governed by the coupling of the DM state to a mostly CP-odd state, in which case the DM relic abundance can be accommodated in agreement with the Planck measurement without sizable modifications to the properties of the 125 GeV Higgs boson with respect to the SM predictions. Thus, allowing for CP-violating phases in the scalar sector significantly widens the allowed parameter space of the model compared to the case in which no CP-violating is considered.

JHEP04(2026)038

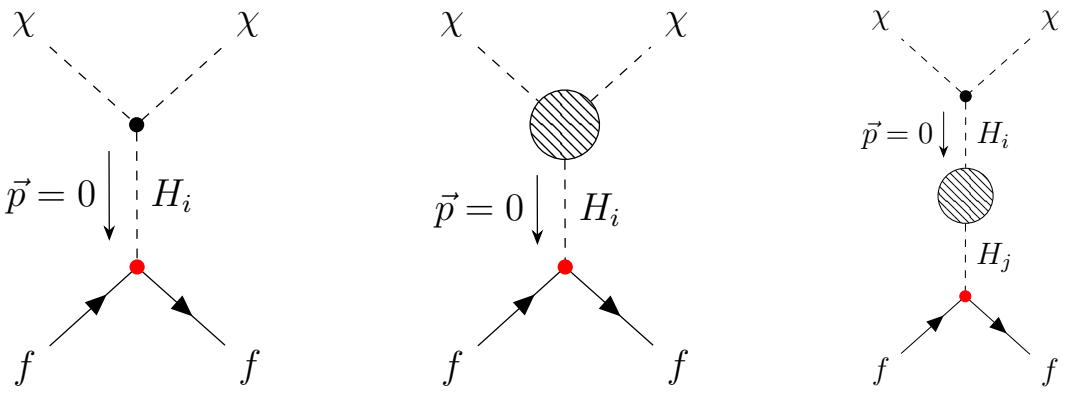

Figure 7. Feynman diagrams for the scattering process $\chi f \to \chi f$ at the classical level (left) and at the quantum level, with vertex corrections (center) and propagator corrections (right). The red vertex is in general CP violating. The hashed blobs represent loop corrections that give rise to non-vanishing amplitudes in the limit of zero momentum transfer $\vec{p} = 0$.

We end this section by mentioning that in regions of the parameter space where the cS2HDM predicts a relic density below the value measured by Planck, there is room for an extended dark sector that could provide the correct abundance. For instance, as discussed in ref. [97], one possibility is to add a second singlet field stabilized by an independent $\mathbb{Z}_2$ symmetry, which couples only feebly to the visible sector. In this case the additional singlet can act as a freeze-in DM candidate, while leaving the collider and Higgs-sector phenomenology of the cS2HDM essentially unaffected.

3.4.2 Direct detection

Due to the pNG-nature of the DM state χ, the scattering process $\chi f \to \chi f$ is absent at classical level in the limit of zero momentum transfer. This is a consequence of a cancellation between the t-channel scattering amplitudes with neutral-scalar exchange corresponding to the Feynman diagrams shown on the left-hand side of figure 7. This cancellation becomes manifest by expressing the $H_i\chi\chi$ couplings as shown on the right-hand side of eq. (2.47) and exploiting the orthogonality of the scalar mixing matrix R. As a result, the scattering rate at DM direct-detection experiments is strongly suppressed. However, the cancellation mechanism does not hold at the quantum level since the global U(1) symmetry is softly broken in order to give a finite mass to χ, see the term proportional to m_χ^2 in the scalar potential shown in eq. (2.1). The potentially numerically important contributions arise at one-loop level from diagrams in which χ appears as virtual particle either in the scalar trilinear vertex or in the t-channel propagator, see the two diagrams on the right-and side of figure 7. Box contributions where two Higgs bosons are exchanged between the DM state χ and the fermion line are highly suppressed by additional factors of first- and second-generation quark Yukawa couplings and are therefore neglected here, see also the discussions in refs. [23, 50, 98].

In order to confront the model with experimental limits from DM direct-detection experiments, we computed the scattering amplitude for the process $\chi f \to \chi f$, where the fermion f can be either an up-type quark u or a down-type quark d, at the one-loop level in

JHEP04(2026)038

the limit of vanishing momentum-transfer.[13] Under the presence of CP-violation, we have to consider also spin- and momentum-dependent operators in the non-relativistic effective theory that describes the DM-nucleon scattering. In the UV theory, the loop diagrams shown in figure 7 generate four dimension-6 operators

$$\mathcal{L}_{\text{UV}} = \sum_q \left(\hat{\mathcal{C}}^{(6)}_{3,q} \mathcal{O}^{(6)}_{3,q} + \hat{\mathcal{C}}^{(6)}_{4,q} \mathcal{O}^{(6)}_{4,q} \right) + \hat{\mathcal{C}}^{(6)}_{5,g} \mathcal{O}^{(6)}_{5} + \hat{\mathcal{C}}^{(6)}_{6,g} \mathcal{O}^{(6)}_{6} \,, \tag{3.7}$$

with the CP-even operators

$$\mathcal{O}^{(6)}_{3,q} = m_q (\chi\chi)(\bar{q}q) \qquad \text{and} \qquad \mathcal{O}^{(6)}_{5,g} = \frac{\alpha_s}{12\pi} (\chi\chi) G^{a\mu\nu} G^a_{\mu\nu} \,, \tag{3.8}$$

and the CP-odd operators

$$\mathcal{O}^{(6)}_{4,q} = m_q (\chi\chi) \mathrm{i} (\bar{q}\gamma_5 q) \qquad \text{and} \qquad \mathcal{O}^{(6)}_{6,g} = \frac{\alpha_s}{8\pi} (\chi\chi) G^{a\mu\nu} \widetilde{G}^a_{\mu\nu} \,, \tag{3.9}$$

and where we follow the notation and conventions of ref. [99]. We make use of the three-flavour scheme in which the sum in eq. (3.7) runs over the light quark flavours $q = u, d, s$. m_q is the mass of the light quark q, α_s is the strong coupling constant at hadronic scales $\mu \approx 1\,\text{GeV}$, and $G^{a\mu\nu}$ and $\widetilde{G}^{a\mu\nu}$ are the gluon field strength tensor and its dual, respectively.

We compute the Wilson coefficients $\hat{\mathcal{C}}^{(6)}_{3,q}$ and $\hat{\mathcal{C}}^{(6)}_{4,q}$ at one-loop level taking into account the set of diagrams depicted generically in the middle and right diagrams shown in figure 7 with $f = q$ and factoring out a factor of m_q. The resulting expressions are UV-finite without renormalization and thus also independent of the renormalization scale. We will present a detailed discussion about this loop computation in an accompanying paper.[14]

The effective operators $\mathcal{O}^{(6)}_{5,g}$ and $\mathcal{O}^{(6)}_{6,g}$ account for the interaction of χ with gluons which is generated via the exchange of the neutral scalars H_i between χ and the heavy quarks Q contained as virtual particles in the nucleons. In the so-called heavy quark expansion [101] one can integrate out the heavy quarks, giving rise to an effective gluon interactions that can be determined via the matching relations [102]

$$m_Q (\bar{Q}Q) \to -\frac{2}{3} \frac{\alpha_s}{8\pi} G^{a\mu\nu} G^a_{\mu\nu} \qquad \text{and} \qquad m_Q \mathrm{i} (\bar{Q}\gamma_5 Q) \to -\frac{\alpha_s}{16\pi} G^{a\mu\nu} \widetilde{G}^a_{\mu\nu} \,, \tag{3.10}$$

where m_Q denotes the mass of the heavy quark. Comparing to eq. (3.7), we therefore obtain the Wilson coefficients for the effective gluon interaction via

$$\hat{\mathcal{C}}^{(6)}_{5,g} = \sum_Q \hat{\mathcal{C}}^{(6)}_{3,Q} \qquad \text{and} \qquad \hat{\mathcal{C}}^{(6)}_{6,g} = \frac{1}{2} \sum_Q \hat{\mathcal{C}}^{(6)}_{4,Q} \,, \tag{3.11}$$

where the sum runs over the heavy quark flavours $Q = t, b, c$. Here $\hat{\mathcal{C}}^{(6)}_{3,Q}$ and $\hat{\mathcal{C}}^{(6)}_{4,Q}$ are the Wilson coefficients of the operators $\mathcal{O}^{(6)}_{3,Q}$ and $\mathcal{O}^{(6)}_{4,Q}$, respectively. Similarly to $\hat{\mathcal{C}}^{(6)}_{3,q}$ and $\hat{\mathcal{C}}^{(6)}_{4,q}$, these are given by the CP-even and CP-odd components of the amplitude resulting from the loop diagrams shown in figure 7 with $f = Q$, respectively.

[13] The contributions from finite-velocity effects are several orders smaller than the quantum corrections assuming cold, i.e. non-relativistic, DM [50]. Thus, they are not taken into account here.

[14] The computations for the scattering rates of pNG DM on nucleons at the one-loop level can be found for the SM+singlet model in refs. [50, 98, 100] and for the CP-conserving 2HDM+singlet model in ref. [23], respectively.

JHEP04(2026)038

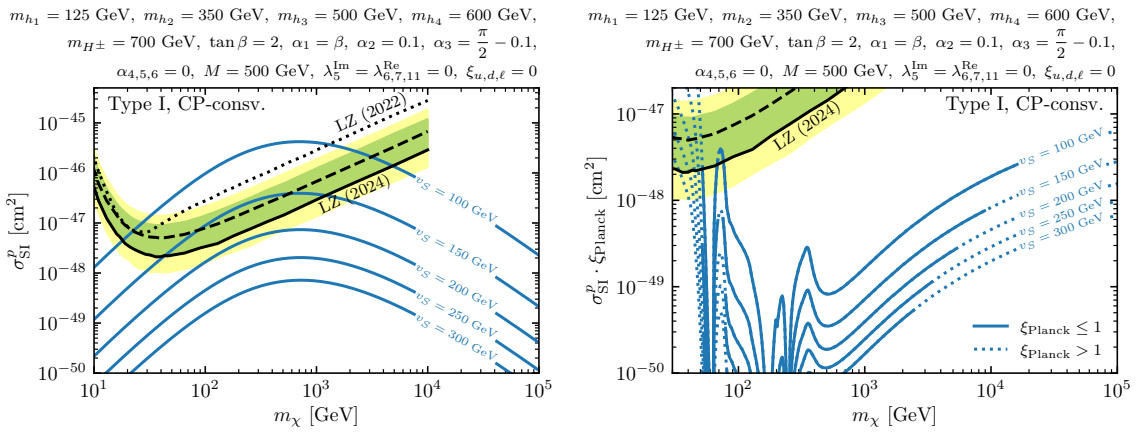

Figure 8. Prediction for the spin-independent DM-proton scattering cross section in the absence of CP-violation in a benchmark scenario taken from ref. [23]. In the right plot, the predicted values of the scattering cross section are rescaled with the ratio $\xi_{\rm Planck} = (\Omega h^2)_{\rm FO}/(\Omega h^2)_{\rm Planck}$, where $(\Omega h^2)_{\rm FO}$ is the predicted DM relic abundance assuming standard freeze-out mechanism and $(\Omega h^2)_{\rm Planck}$ is the experimental value measured by Planck [96]. If the blue lines are displayed as dashed lines, then the parameter points predict $\xi_{\rm Planck} > 1$ and are excluded based on the measured value of the DM relic abundance. Also shown are the currently strongest experimental expected and observed 90% confidence-level limits from the LZ experiment with the black dashed and solid line, respectively [104]. The green and yellow shaded regions indicate the 1σ and 2σ uncertainty bands, respectively. The left plot also shows with the dotted black line the previous LZ limit published in 2022 [105].

With the Wilson coefficients in the UV theory at hand, one can compute the scattering rates for different DM direct detection experiments. In the absence of CP-violation, one finds $\hat{\mathcal{C}}^{(6)}_{4,q} = \hat{\mathcal{C}}^{(6)}_{6,g} = 0$, and only spin-independent scattering cross sections are generated which for a given nucleon $N = p, n$, with p and n being the proton and the neutron, respectively, can be written as [103]

$$\sigma^N_{\rm SI} = \frac{1}{\pi} \frac{m_N^4}{(m_N + m_\chi)^2} \left| \sum_q F_S^{q/N} \hat{\mathcal{C}}^{(6)}_{3,Q} + \frac{2}{27} F_G^N \hat{\mathcal{C}}^{(6)}_{5,g} \right|^2 , \tag{3.12}$$

where m_N is the nucleon mass, and where the hadronic form factors $F_S^{q/N}$ for scalar currents have to be extracted from experimental data or derived using lattice simulations in QCD, see discussion below, and $F_G^N \approx 1 - \sum_q F_S^{q/N}$. The predicted spin-independent nucleon scattering cross section $\sigma^N_{\rm SI}$ can then readily be confronted with the upper limits reported by the various DM direct-detection experiments.

In figure 8 we show a comparison between the predicted values for the spin-independent DM-proton scattering cross section $\sigma^p_{\rm SI}$ as a function of the DM mass m_χ and for different values of v_S in a CP-conserving benchmark scenario taken from ref. [23] for which the expression given in eq. (3.12) can be applied. We verified that this scenario satisfies the theoretical constraints from the boundedness of the scalar potential and from perturbative unitarity. In the left plot of figure 8 we validate the result from ref. [23], demonstrating that the scattering rates generated at one-loop level can be of the order of the currently strongest experimental limits from the LZ collaboration [106] for values of v_S substantially below the

JHEP04(2026)038

masses of the BSM neutral Higgs bosons, where the scalar couplings related to the singlet field λ_8, λ_9, λ_{10} and λ_{11} become sizable, see eqs. (2.41)–(2.44). On the other hand, for values of $v_S \gtrsim m_{H_2}, m_{H_3}, m_{H_4}$ the predicted scattering cross sections rapidly fall below the current and near future experimental sensitivity of DM direct detection experiments.

The same scalar portal couplings governing the scattering amplitudes are also responsible for the DM annihilation process in the early universe that determines the predicted relic abundance of DM. As a result, for pNG DM the parameter space regions that can potentially be probed by direct detection experiments typically predict a significant under-abundance of DM, i.e. $\xi_{\text{Planck}} \ll 1$ as defined in eq. (3.6). In this case, the reduced density of DM particles that reach the detector, and thus the expected number of scattering events, are suppressed by factors of ξ_{Planck}. Since the experimental collaboration assume the measured value of the DM relic abundance when setting limits, one can account for the impact of a smaller DM density by comparing the product $\sigma^p_{\text{SI}} \cdot \xi_{\text{Planck}}$ to the experimental limit on σ^p_{SI}. This is what we show in the right plot of figure 8 with ξ_{Planck} computed using `micrOMEGAS` [43] (see the discussion in section 3.4.1) and assuming the standard freeze-out mechanism. Here the lines indicate the value of $\sigma^p_{\text{SI}} \cdot \xi_{\text{Planck}}$ for the same parameter point shown in the left plot. The intervals in which solid lines are displayed correspond to values of $\xi_{\text{Planck}} \leq 1$, and dashed lines are used for $\xi_{\text{Planck}} > 1$. In the latter case, the corresponding parameter points are excluded because the DM relic abundance is predicted to be too large. One can see that now the prospects for the direct detection of χ are severely reduced. Conversely, a hypothetical detection of DM at direct detection experiments currently in operation would be incompatible with the depicted benchmark scenario for all values of v_S except for $v_S = 100\,\text{GeV}$ and a DM mass of $m_\chi \approx 80\,\text{GeV}$.

So far we have focused on a CP-conserving scenario. However, the cancellation mechanism suppresses the tree-level contribution to the DM-nucleon scattering irrespective if explicit sources of CP-violation are present in the scalar potential or the Yukawa sector, in contrast to the well studied 2HDM+a DM model. Under the presence of CP-violating parameters, the comparison to the experimental data from DM direct detection experiments becomes significantly more involved because also momentum-dependent and spin-dependent interactions between the DM state χ and the nucleons are generated. In order to take into account these effects, it is required to consider additional operators in the non-relativistic effective description of the DM-nucleon scattering. To this end, we perform a matching of the Wilson coefficients in the UV theory shown in eq. (3.7) to the relevant set of Galilean-invariant operators in the non-relativistic effective field theory describing the interaction between χ and nucleons [99],

$$\mathcal{L}_{\text{NR}} = c_1^N \mathcal{O}_1^N + c_{10}^N \mathcal{O}_{10}^N \qquad \text{with} \qquad \mathcal{O}_1^N = \mathbb{1}_N \qquad \text{and} \qquad \mathcal{O}_{10}^N = -\text{i}\left(\vec{S}_N \cdot \frac{\vec{q}}{m_N}\right), \tag{3.13}$$

where $N = p$ for protons and $N = n$ for neutrons. Here, c_1^N and c_{10}^N are the Wilson coefficients of spin-independent and spin-dependent interactions contained in the operators $\mathcal{O}_1^N$ and $\mathcal{O}_{10}^N$, respectively.[15] $\vec{S}_N$ denotes the spin of the nucleon N, and $\vec{q}$ is the three-momentum vector of the exchanged momentum in the χ-N scattering. No other operators are generated in

[15] The lower index of the non-relativistic operators $\mathcal{O}_i^N$ is a naming convention. In total there are ten different operators that can be obtained in a non-relativistic reduction of a manifestly relativistic operator basis up to second order in $\vec{p}$ if one considers only spin-0 or spin-1 mediators [107].

JHEP04(2026)038

the non-relativistic effective field theory at leading order in the chiral expansion from the operators present in our model in the UV shown in eq. (3.7). The Wilson coefficients are in general momentum dependent, but working in the limit of vanishing momentum exchange we can perform the matching between the UV theory and the non-relativistic EFT to leading order in chiral counting. One finds the relations [108]

$$c_1^N = \frac{1}{2m_\chi}\left(\sum_q F_S^{q/N}\hat{\mathcal{C}}_{3,q}^{(6)} + F_G\,\hat{\mathcal{C}}_{5,g}^{(6)}\right), \tag{3.14}$$

$$c_{10}^N = \frac{1}{2m_\chi}\left(\sum_q F_P^{q/N}\hat{\mathcal{C}}_{4,q}^{(6)} + F_{\widetilde{G}}\,\hat{\mathcal{C}}_{6,g}^{(6)}\right), \tag{3.15}$$

where $F_S^{q/N}$, $F_P^{q/N}$, F_G and $F_{\widetilde{G}}$ are hadronic form factors whose values can be computed in lattice QCD. We use the numerical values summarized in ref. [108] using lattice QCD results from refs. [109–111]. The Wilson coefficients for the scattering on protons ($N = p$) and neutrons ($N = n$) can be decomposed into isoscalar (s) and isovector (v) components,

$$c_i^s = \frac{1}{2}(c_i^p + c_i^n)\,, \qquad c_i^v = \frac{1}{2}(c_i^p - c_i^n)\,, \tag{3.16}$$

which are often used as independent interactions in experimental analyses.

Once c_1^N and c_{10}^N are known, the scattering rates can be computed for different target materials and exposure time of the different experiments. We can circumvent this step because recently the LZ collaborations has presented exclusion limits directly on the Wilson coefficients $c_i^{s,v}$ of the non-relativistic EFT based on the data collected until 2022 [106]. In figure 9 we show a comparison between the LZ limits on the EFT Wilson coefficients and the predicted values $c_{1,10}^{s,v}$ (normalized to $1/v^2$) for the benchmark point used also in figure 8, but with a fixed value of $v_S = 200\,\text{GeV}$, and we use non-zero values for $\alpha_4 = \alpha_5$ in order to study the phenomenological impact of the presence of CP-violation. In the two plots in the bottom row one can see that the coefficients c_{10}^s and c_{10}^v, corresponding to the CP-odd operator $\mathcal{O}_{10}$, are several orders of magnitudes below the experimental sensitivity of the LZ experiment (or other comparable DM direct detection experiments). We therefore conclude that for the pNG DM state contained in our model the experimental constraints on the spin-dependent scattering of χ on nucleons do not play a role. In the top row, in which we show the predictions for the coefficients c_1^s and c_1^v, corresponding to the CP-even operator $\mathcal{O}_1$, one can see that the isoscalar interactions give rise to the dominant contributions to the spin-independent scattering. For fixed values of the DM mass, the values of $(c_1^s \times v^2)^2$ vary by almost a factor of 100 by changing the mixing angles α_4 and α_5 from 0 to 0.4. As a consequence, while the spin-dependent interactions directly induced by the CP-violation is not observable, the indirect effects of the CP-violation on the magnitude of the spin-independent interactions are significant and should be taken into account in a prediction for scattering rates at DM direct-detection experiments. In our presentation of benchmark scenarios in section 4, we will apply as a constraint the most recent LZ limits on the spin-independent DM-nucleon scattering cross sections (see figure 8), including the indirect effects of the CP-violating effects via their impact on the CP-even operators $\mathcal{O}_{3,q}$ and $\mathcal{O}_{5,g}$ (see eq. (3.8)), and not considering any further the experimental limits on the spin-dependent interaction rates.

JHEP04(2026)038

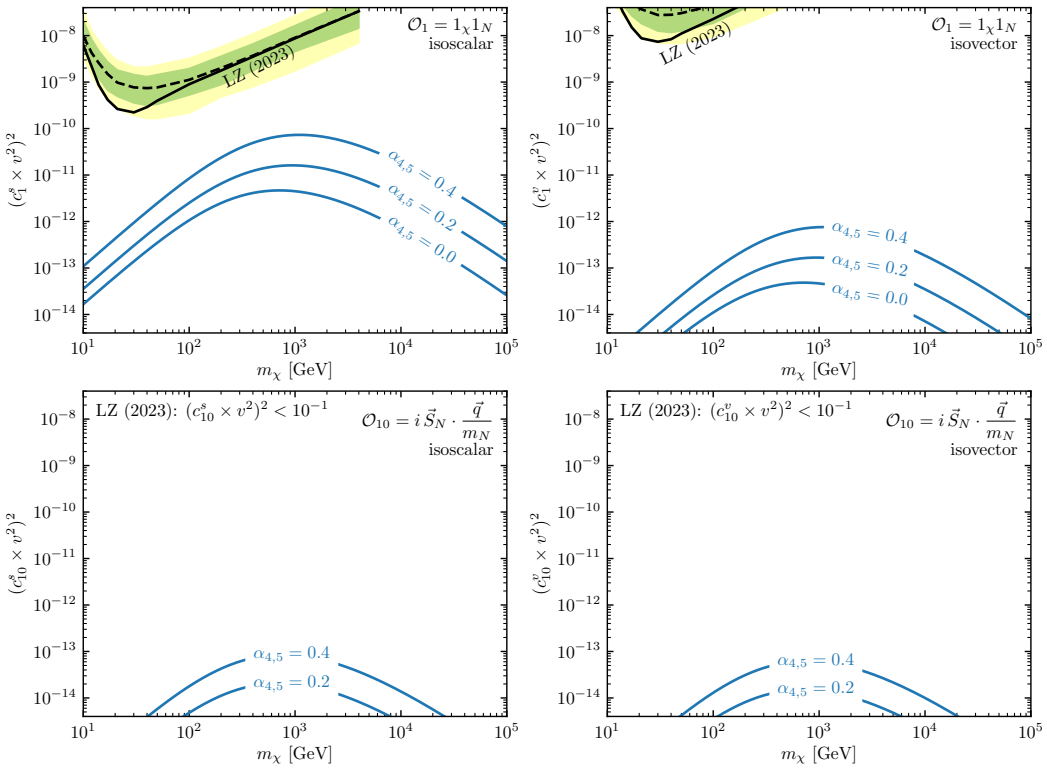

Figure 9. Predicted values of the squared Wilson coefficients c_1^s, c_1^v, c_{10}^s and c_{10}^v as defined in eq. (3.16) as a function of the DM mass m_χ in the top left, top right, bottom left and bottom right plot, respectively, normalized to $1/v^2$, and for different values of the mixing angles α_4 and α_5. The other free parameters are fixed as shown in figure 8. The plots in the top row also show the current experimental upper limits on c_1^s, c_1^v from the LZ collaboration [106].

3.4.3 Indirect detection

DM indirect detection experiments search for astrophysical signals that arise from the annihilation or decay of DM particles, which would result in gamma rays, neutrinos or cosmic rays consisting of high-energetic electrons, positrons and antiprotons. The primary constraints from DM indirect detection come from the observations of astronomical objects with high DM density, such as the galactic center of the milky way, dwarf spheroidal galaxies or galaxy clusters. In the present model, the scalar DM particle χ interacts with the visible sector via the Higgs sector, such that it mostly annihilates into third-generation fermions or gauge bosons, which subsequently decay into stable particles. The dominant annihilation processes depend on the DM mass m_χ, the mass spectrum of the neutral Higgs bosons, m_{H_i}, and their coupling to χ.

Experimental constraints on today's DM annihilation cross sections have been set by a variety of indirect detections experiments, including observations from the Fermi-LAT telescope [112], HESS [113], MAGIC [114] and AMS-02 [115]. In the context of our model, however, the potential impact of these constraints is very limited, in particular on rather light DM masses with $m_\chi \lesssim 70\,\text{GeV}$ [21] where the parameter space is much more stringently constrained by LHC limits on the invisible branching ratio of the 125 GeV Higgs boson and

JHEP04(2026)038

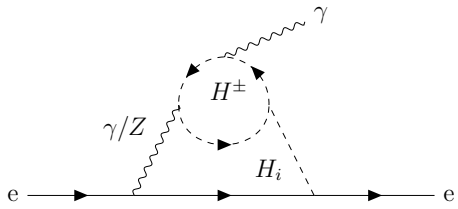

Figure 10. Example diagram with a charged Higgs boson loop contributing to the electron EDM at the two-loop level.

the Planck measurement of the DM relic abundance.[16] For larger DM masses the particle density of DM particles is substantially smaller, suppressing the expected rate of cosmic rays generated via DM annihilation, and the measured value of the DM relic abundance (taken as an upper bound) typically results in stronger constraints on the parameter space [19, 21, 24].[17] Additionally, the constraints from DM indirect detection experiments suffer from sizable systematic uncertainties which arise from uncertainties in the DM density profile within the observed astronomical objects and along the propagation path of the cosmic rays, the propagation models of cosmic-ray particles, and the modeling of different background signals from other astrophysical sources. As a consequence, we do not consider constraints from DM indirect detection in this work, leaving a comprehensive analysis for this model, including the impact of CP-violating interactions, for future work.

3.5 Electric dipole moments

The most stringent constraints on CP-violation in the Higgs potential typically arise from the non-observation of electron electric dipole moments (eEDMs). This holds true in the model considered here. The eEDM d_e is defined in the $q^2 = 0$ limit of the CP-odd Pauli form factor in the $e^+e^-\gamma$ vertex function [118]

$$id_e\bar{u}(p')\sigma^{\mu\nu}q_\nu\gamma_5 u(p)\,, \qquad \sigma^{\mu\nu} = \frac{i}{2}[\gamma^\mu, \gamma^\nu]\,, \tag{3.17}$$

where $u(p)$ is the electron Dirac spinor, q is the incoming momentum of the photon, and γ^μ are the Dirac matrices. The theoretical predictions for the eEDM in this model have been investigated in ref. [24]. There it was shown that (as in the CP-violating 2HDM) the numerically dominant contributions in most parts of the parameter space arise first at the two-loop level, whereas the one-loop contributions to the eEDM are subleading barring sizable destructive interferences at the two-loop level. Taking this into account, in our analysis we consider the two-loop Barr-Zee type contributions [119]. An example diagram is shown in figure 10, where CP-violation can be present in the $H^\pm H^\mp H_i$ couplings (see section 2.5.1)

[16] See ref. [21] for a discussion of the parameter space regions favoured by the galactic-center excess [116] in the CP-conserving limit of our model.

[17] It has recently been pointed out in ref. [117] that primordial magnetic fields may seed the formation of dense early minihalos, potentially enhancing the DM annihilation rate and thereby, depending on the main annihilation channel, leading to significantly stronger indirect detection constraints on WIMP scenarios. We do not take these effects into account in the present analysis.

JHEP04(2026)038

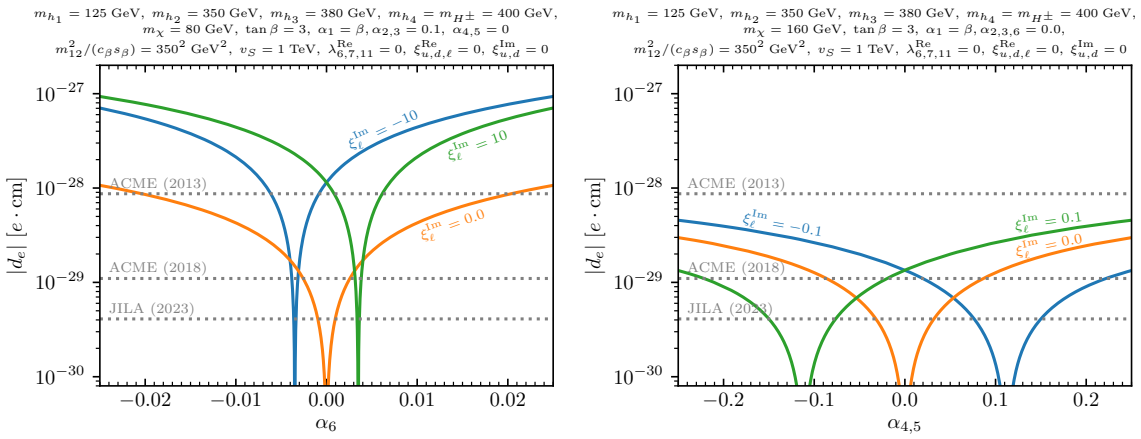

Figure 11. Predicted values of the eEDM $|d_e|$ (see text for details) as a function of α_6 (left) and $\alpha_4 = \alpha_5$ (right) for $\xi_\ell^{\mathrm{Im}} = -10$, $\xi_\ell^{\mathrm{Im}} = 0$ and $\xi_\ell^{\mathrm{Im}} = 10$ (left) and $\xi_\ell^{\mathrm{Im}} = -0.1$, $\xi_\ell^{\mathrm{Im}} = 0$ and $\xi_\ell^{\mathrm{Im}} = 0.1$ (right) in blue, orange and green, respectively, with the other free parameters set as shown on top of the plot. The horizontal gray dashed lines indicate the experimental 90% confidence-level upper limits from the ACME [124, 125] and JILA [126] collaborations.

and in the $H_i e^+ e^-$ couplings (see section 2.5.2). This diagram is special since, in the absence of CP-mixing in the scalar sector and without CP-violating $H_i f \bar{f}$ couplings, this diagram can still give rise to non-vanishing EDMs for $\lambda_5^{\mathrm{Im}} \neq 0$ from the diagram with the state A_0 on the internal line connecting the electron propagator with the $H^\pm$-loop, via the CP-violating $A_0 H^\pm H^\mp$ coupling given for the alignment limit in eq. (2.52). Another set of diagrams which contributes only under the presence of CP-violating $H_i f \bar{f}$ couplings is obtained, for instance, by replacing the $H^\pm$-loop with a fermion-loop, in which case also CP-violating couplings of the neutral scalars H_i to top and bottom quarks become relevant, which has great implications for the interplay between the eEDM and the phenomenology at the LHC.

Our computation of the eEDM is based on the complete set of gauge-invariant Barr-Zee type contributions published for the complex 2HDM in ref. [120].[18] In order to make these expressions applicable to our model, we replaced the effective couplings of the Higgs bosons contained in the complex 2HDM by the corresponding coupling factors of the Higgs bosons contained in our model, taking into account the additional neutral scalar state originating from the real component of the singlet field Φ_S. To approximately account for sizable QCD corrections [122] in the contributions with bottom- and charm-quarks, we use running quark masses at the electroweak scale $\mu = M_Z$ as put forward in ref. [123]. The DM state (originating from the imaginary component of Φ_S) does not enter in the eEDM predictions at two-loop level. As a consequence, at the considered loop order the DM mass m_χ can be varied in our model without having an impact on the eEDM.

To get an idea of the typical size of the eEDM, we show the predictions for $|d_e|$ in an example scenario as a function of the mixing angle α_6 and for three different values of ξ_ℓ^{Im} in the left plot of figure 11. All other free parameters are set as shown on top of the plot.

[18] We did not include the so-called kite diagrams (cf. ref. [118] and ref. [121] for recent discussions in the context of the CP-violating 2HDM and the next-to-minimal supersymmetric extension of the SM (NMSSM), respectively). Their contribution will be discussed in a future publication.

JHEP04(2026)038

Also indicated with horizontal dotted lines are the experimental upper limits on $|d_e|$ at 90% confidence level obtained by the ACME collaboration in 2013 [124] and 2018 [125], and by JILA in 2023 [126]. Non-zero values of the mixing angle α_6 in general give rise to a non-zero CP-odd admixture in the state H_1, which here corresponds to the Higgs boson at 125 GeV. Moreover, non-zero values of ξ_ℓ^{Im} give rise to CP-violating couplings between the Higgs bosons H_i and charged leptons, also inducing non-zero values for the eEDM. The orange line showing the case $\xi_\ell^{\text{Im}} = 0$ goes to zero for $\alpha_6 = 0$ where the model is CP-conserving. For $\alpha_6 \neq 0$ the orange line grows to values of $|d_e| \gtrsim 10^{-28}\ e\cdot$ cm, which is more than an order of magnitudes larger than the current experiment limits. The blue and the green lines show the predictions for the eEDM for non-zero values of $\xi_\ell^{\text{Im}} = -10$ and $\xi_\ell^{\text{Im}} = 10$, respectively. This leads to a shift to non-zero values of the mixing angle α_6 where the considered example parameter point is in agreement with the experimental upper limits on the eEDM. This demonstrates that it is possible to have a cancellation in the eEDM between the CP-violation from the Higgs potential (for $\alpha_6 \neq 0$ here) and the CP-violation from the Yukawa sector (for $\xi_\ell^{\text{Im}} \neq 0$ here), such that the predicted value for the eEDM is below the current bounds. However, if the CP-violating effects are present in the couplings of the 125 GeV Higgs boson as is the case here, the cancellation requires a substantial amount of fine-tuning of parameters, as is visible in the left plot of figure 11. It should be noted here that if large cancellations between different amplitudes at the considered two-loop level are present, the numerically most important contributions to the eEDM are at some point expected to arise at the one-loop level or the three-loop level which are not taken into account here.

In the right plot of figure 11 we show $|d_e|$ as a function of $\alpha_4 = \alpha_5$, and for three different values of $\xi_\ell^{\text{Im}} = -0.1$, $\xi_\ell^{\text{Im}} = 0.0$ and $\xi_\ell^{\text{Im}} = 0.1$ in blue, orange and green, respectively. Non-zero values of the mixing angles α_4 and α_5 result in CP-violating mixing between the BSM Higgs bosons $H_{2,3,4}$, whose masses are set to $m_{H_2} = 350$ GeV, $m_{H_3} = 380$ GeV and $m_{H_4} = 400$ GeV. For the SM-like Higgs boson H_1 at 125 GeV, on the other hand, there is no CP-odd admixture since here $\alpha_6 = 0$. By comparing both plots in figure 11 one can see that the predicted eEDM induced by non-zero values of α_4 and α_5 (right plot) is substantially smaller compared to the predictions for non-zero values of α_6 (left plot). This demonstrates that the cancellation that is required to predict a sufficiently small eEDM under the presence of CP-violation is significantly less severe if the CP-violating effects are mostly confined to the properties of the BSM Higgs bosons with masses that are greater than 125 GeV, while the 125 GeV Higgs boson acts mostly as a CP-even state. This is in line with the fact that (in the absence of accidental cancellations) the generated eEDM scale via [127]

$$|d_e| \sim \frac{m_e}{1\text{ MeV}} \left(\frac{1\text{ TeV}}{M}\right)^2 \cdot 10^{-26}\ e\text{ cm}\,, \tag{3.18}$$

where M represents the mass scale of the particles whose interactions are CP-violating. Hence, the heavier the Higgs bosons H_i with CP-violating couplings, the smaller is the resulting eEDM.

4 Benchmark planes and scans

In this section, we discuss the results of our numerical analysis regarding the impact of the theoretical and experimental constraints on the parameter space of the cS2HDM, with a

JHEP04(2026)038

special focus on the eEDM experimental upper bound, the DM direct detection limits, and the LHC Higgs data. In section 4.1 and section 4.2, we discuss the results from a scan over the parameter space of the model. We generated random parameter points and tested them against theoretical and experimental constraints as described in section 3. The values for each free parameter (see eq. (2.46)) of the parameter points were selected within the intervals summarised in table 2. In this parameter scan, all points were required to satisfy the theoretical, collider, and EWPO constraints, except for DM direct detection and eEDM bounds. These two constraints were instead studied in detail using the scan results in order to investigate their impact on the parameter space. In practice, the direct detection limits turned out to not exclude any parameter point due to the cancellation mechanism (see section 3.4.2), while the parameter points excluded or allowed by the eEDM are explicitly indicated in figure 11 and figure 14. After discussing the results of the parameter scan, in section 4.3 we compare the sensitivity of LHC cross section measurements of the 125 GeV Higgs boson to CP-violating couplings, and compare it to the sensitivity of eEDM experiments.

Throughout our numerical analysis, we consider parameter space regions where the masses of the BSM Higgs bosons are restricted to values below 1 TeV. We stress that this is a choice rather than a limitation of the model. The cS2HDM features a well-defined decoupling limit in which all BSM scalars can become heavy: $M \approx v_S \approx m_{H_{2,3,4}} \approx m_{H^\pm} \gg v$, where v denotes the Higgs vacuum expectation value and represents the electroweak scale. We focus on scalar masses below the TeV scale for several reasons. First, this mass range allows for direct production of the additional Higgs bosons at the LHC, making the model testable at current and future colliders. Second, DM direct detection experiments are most sensitive to scenarios in which the DM mass (which is naturally bound to be close to the Higgs boson masses for efficient annihilation in the early universe) are below the multi TeV-range. Third, Higgs bosons with masses substantially larger than the electroweak scale effectively decouple, rendering a strong first-order electroweak phase transition unlikely, such that electroweak baryogenesis cannot be realized.

4.1 The electron EDM constraint

As explained in section 3.5, the eEDM is one of the most stringent constraints on CP-violation in the Higgs potential. In light of the recent improvements of the experimental upper limit on the eEDM, see the discussion in section 3.5, we performed a random parameter scan in order to confirm that it is possible to find points in the parameter space of the cS2HDM that are allowed by this constraint. In figure 12, we show the predicted values for the eEDM $|d_e|$ for each parameter point plotted against the mass of the DM candidate m_χ. All displayed points we generated by demanding that the whole set of theoretical and experimental constraints discussed in section 3 is satisfied, with the exception of the upper limit on the eEDM. The black lines represent the latest upper bounds on the eEDM as presented by the ACME Collaboration in 2014 [124] (solid) and 2018 [125] (dash-dotted), and more recently by the JILA in 2023 [126] (dashed). One can see that while most parameter points are excluded by the most stringent experimental limit from JILA, in line with the expectation from eq. (3.18), there are also parameter points over the whole scan range of the DM mass that still evade this constraint. This shows that in the cS2HDM the possibility of having CP-violation in both the scalar and Yukawa sectors provides the necessary cancellation to sufficiently suppress the

JHEP04(2026)038

Parameter	Range	Parameter	Range
m_{H_1}	125.09	M	$[200, 1000]$
m_{H_2}	$[20, 1000]$	v_S	$[200, 1000]$
m_{H_3}	$[20, 1000]$	λ_5^{Im}	0
m_{H_4}	$[20, 1000]$	λ_6^{Re}	0
$m_{H^\pm}$	$[200, 1000]$	λ_7^{Re}	0
m_χ	$[20, 1000]$	$\lambda_{11}^{\mathrm{Re}}$	0
$\tan\beta$	$[1, 10]$	ξ_u^{Re}	$[-15, 15]$
α_1	β	ξ_d^{Re}	$[-15, 15]$
α_2	0	ξ_ℓ^{Re}	$[-15, 15]$
α_3	$[-\frac{\pi}{2}, \frac{\pi}{2}]$	ξ_u^{Im}	$[-15, 15]$
α_4	$[-\frac{\pi}{2}, \frac{\pi}{2}]$	ξ_d^{Im}	$[-15, 15]$
α_5	$[-\frac{\pi}{2}, \frac{\pi}{2}]$	ξ_ℓ^{Im}	$[-15, 15]$
α_6	0		

Table 2. List of parameter ranges for the random scan of the parameter space of the cS2HDM. The values for the masses and v_S are expressed in GeV and single values represent constant values for the corresponding parameter.

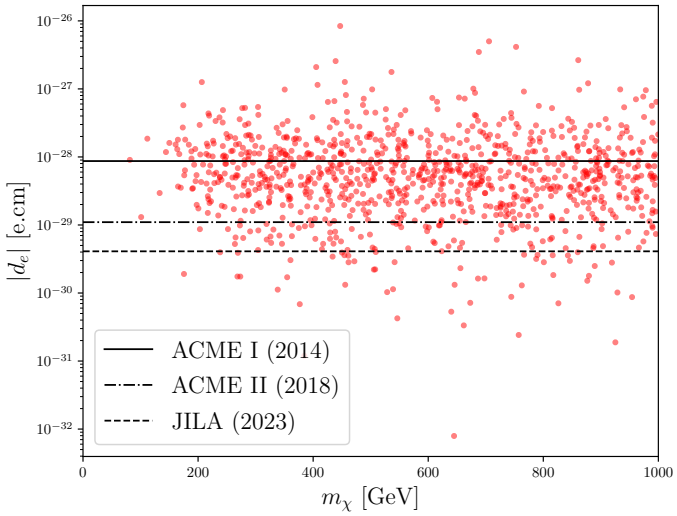

Figure 12. Predicted values of the electron EDM as a function of the DM candidate mass for a parameter space scan. The horizontal black lines represent the experimental upper limits from the ACME [124, 125] and JILA [126] collaborations.

eEDM down to the allowed range. In addition, the allowed parameter points are distributed down to rather low DM masses of $m_\chi \lesssim 200\,\mathrm{GeV}$. This shows that the eEDM constraint does not exclude the part of the parameter space that could potentially be probed with DM searches at the LHC. This enables an interesting interplay between the eEDM measurements and LHC DM searches that can be exploited to constrain the model.

JHEP04(2026)038

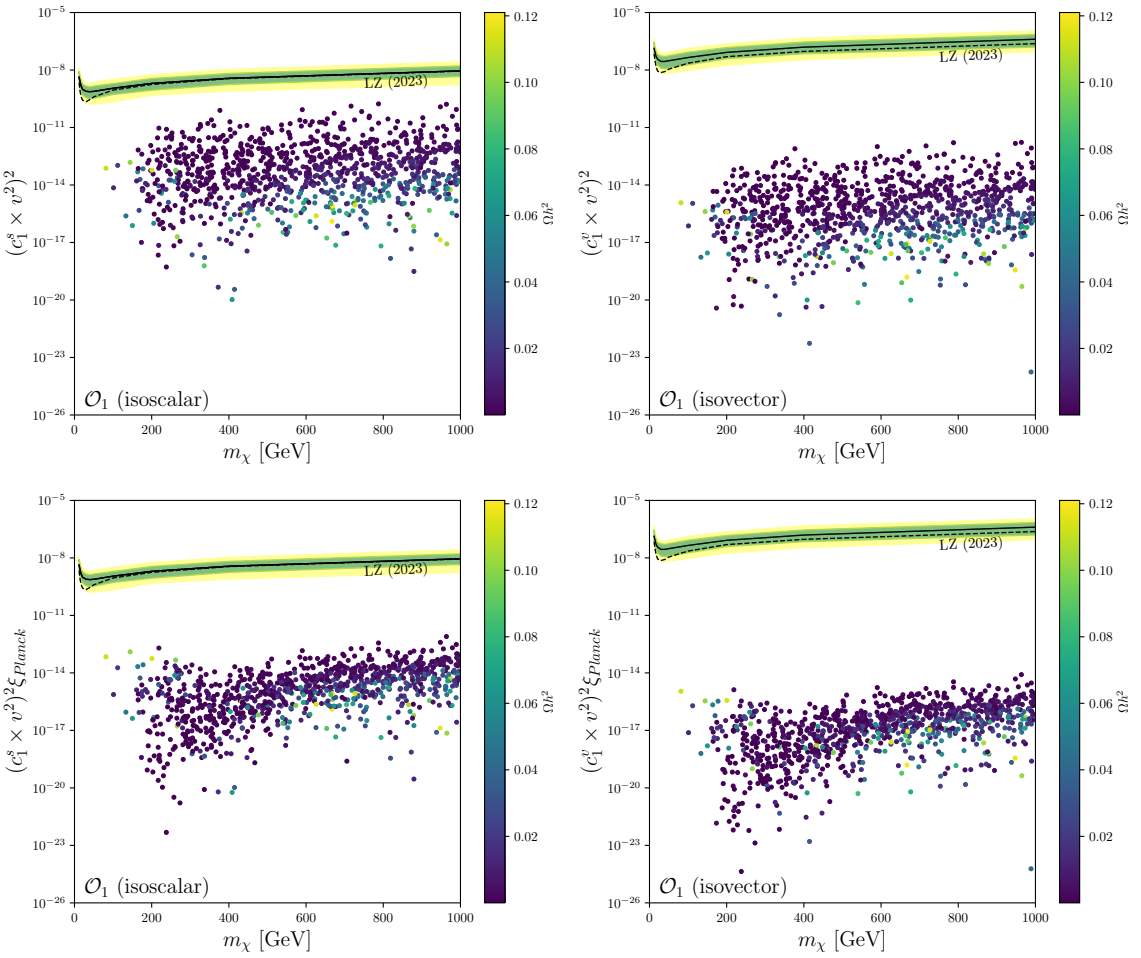

Figure 13. Predicted values of the squared non-relativistic Wilson coefficients c_1^s (left) and c_1^v (right) plotted against the DM mass m_χ for a scan of the parameter space. Also shown with the solid and dashed black lines are the observed and expected upper limits set by the LZ experiment, respectively [106]. The green and orange bands show the 1σ and 2σ uncertainty bands, respectively. The color of each point indicates the predicted DM relic abundance. In the bottom row, the values for each point were scaled by ξ_{Planck} to adjust for the respective fraction of the DM relic density.

4.2 DM direct detection

As mentioned before, one of the most attractive features of pNG DM models is the fact that the DM-nucleon scattering cross section is naturally suppressed, making it easier to evade the DM direct detection constraint. To demonstrate this, and to estimate to what extend current direct detection limits are able to probe the parameter space of the cS2HDM, we analyze here the predicted DM-nucleon scattering cross sections focusing on the dominant spin-independent interactions (see the discussion in section 3.4.2. We compare the theoretical predictions against the currently most stringent cross-section limits that were published by the LZ collaboration.

In the top row of figure 13 we show the predicted values for the squared Wilson coefficients c_1^s (left) and c_1^v (right) respectively referring to the isoscalar and isovector components of the non-relativistic spin-independent operator $\mathcal{O}_1$, as defined in eq. (3.16), plotted against the mass of the DM candidate m_χ. The color code represents the predicted relic abundance Ωh^2

JHEP04(2026)038

for each point. Finally, the black line represents the observed experimental upper bound as presented by the LZ Collaboration in 2023 [106]. We observe that most points are several orders of magnitude below the experimental limit for both the isoscalar and isovector Wilson coefficients, confirming that the pNG nature of the DM candidate makes it possible to evade the DM direct detection constraint. Nevertheless, we also find parameter points which are only about two orders of magnitude below the LZ limit, and which therefore might be in reach of future experiments [128]. For most points, the DM candidate accounts only for a small fraction of the measured DM relic abundance of the Universe, meaning that in these cases some additional DM mechanism not present in our model would be needed to explain the remaining relic abundance. Regarding the DM mass, we observe that the allowed points cover the range from around 100 GeV to 1 TeV. The lower limit of the range of m_χ arises mainly from LHC Higgs data because for $m_\chi \leq 62\,\text{GeV}$ the decay channel $H_1 \to \chi\chi$ becomes kinematically allowed, which is highly constrained by direct searches for invisible Higgs boson decays and from global fits to the LHC cross section measurements [10]. However, it should be noted that in a parameter scan that is more targeted to the low-mass region it is possible to find valid parameter points also for $m_\chi \leq 62\,\text{GeV}$ [21].

We included CP-violating phases in the parameter scan via non-zero values of the flavour alignment parameters $\xi_{u,d,\ell}$ and the mixing angles $\alpha_{4,5}$. Thus, our parameter scan demonstrates that the introduction of CP-violation in the cS2HDM does not spoil the suppression of the DM-nucleon scattering rates. For models like the 2HDM+a, where the presence of CP-violation in the Higgs sector is expected to weaken the suppression of the scattering rates, it would be worthwhile to investigate how significant this effect is. We leave an analysis of the size of scattering cross sections in the 2HDM+a in the presence of CP-violation in the Higgs sector, and a comparison to the cS2HDM studied here, for future work.

The LZ experimental limit, as shown in figure 13, is determined assuming that the DM candidate represents the full measured DM relic abundance. For our scan we only required that the predicted DM relic abundance is below the measured limit. To compare our theoretical predictions with the experimental measurements taking into account this effect of a reduced particle density of χ according to the predicted relic abundance, one can in an approximate approach re-scale the predicted value for the DM-nucleon scattering cross section for each point by the fraction of the predicted over the measured DM relic abundance. In the bottom row of figure 13, we show the squared Wilson coefficients c_1^s (left) and c_1^v (right) re-scaled by the ratio ξ_{Planck} as defined in eq. (3.6), plotted against the mass of the DM candidate m_χ. Again, the color code represents the predicted DM relic abundance Ωh^2 for each point. We see that, in comparison with the unscaled predictions shown in the plots in the top row, most points move substantially further away from the experimental upper bound. We carried out the same analysis for the non-relativistic spin-dependent operator $\mathcal{O}_{10}$. In this case, the values for the correspondent Wilson coefficients c_{10}^s and c_{10}^v, were many orders of magnitude lower than the spin-independent counterparts, therefore reinforcing the conclusions drawn at the end of section 3.4.2 that for the pNG DM state the experimental constraints on the spin-dependent DM-nucleon scattering do not play a role even if explicit CP-violation is considered.

As mentioned already above, the most sensitive observable to new sources of CP-violation is the eEDM. It is therefore interesting to investigate possible correlations between the

JHEP04(2026)038

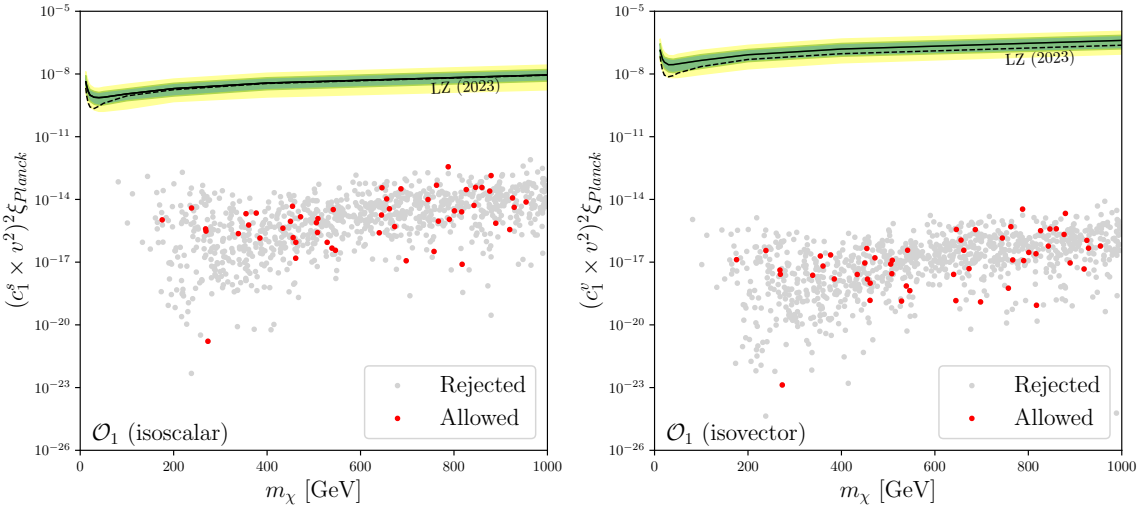

Figure 14. Predicted values of the squared non-relativistic Wilson coefficients c_1^s (left) and c_1^v (right) re-scaled with the ratio of predicted over observed relic abundance ξ_{Planck} plotted against the DM mass m_χ for a scan of the parameter space. The red points are allowed by the JILA 2023 electron EDM constraint while the gray points are excluded.

predicted values for the eEDM and the DM-nucleon scattering cross sections. In figure 14 we show as in the bottom row of figure 13 the predicted re-scaled values of the squared non-relativistic Wilson coefficients c_1^s (left) and c_1^v (right) plotted against the mass of the DM candidate m_χ. The gray points represent the points that are excluded by the eEDM experimental upper bound given by the JILA Collaboration, while the red points represent the points that evade this constraint. The allowed points have values between 10^{-17} and 10^{-12} for c_1^s and between 10^{-19} and 10^{-14} for c_1^v. The allowed points are uniformly distributed across the displayed DM mass interval. Consequently, the constraints from DM direct detection experiments (once reaching more sensitivity to pNG DM) and the ones from the eEDM measurements are largely independent and complementary.

4.3 LHC sensitivity to CP-violating Higgs boson couplings

An important question is to what extent the LHC can probe CP-violation in the observed 125 GeV Higgs boson, or if sizable CP-odd components that could give rise to detectable effects are already excluded by the stringent upper limits on the eEDM. In addition, searches for additional Higgs bosons at the LHC provide complementary sensitivity to CP-violating phases, since CP-violating coupling components can enhance or suppress certain production and decay channels. We stress that in this discussion we will focus on LHC measurements or experimental limits on total cross sections that are not themselves direct indications of CP-violation, but which are modified in the presence of CP-mixed interactions.[19] This is in contrast to the eEDM bounds, which provide an unambiguous probe of CP-violation.

[19]Truly CP-sensitive Higgs boson observables can be obtained by utilizing differential information and angular distributions, which have been employed in measurements of Higgs boson decays into τ-lepton pairs [129, 130], Higgs boson production in association with top quarks [131, 132], and Higgs boson production via vector-boson fusion [133, 134]. The resulting constraints on CP-violating Higgs boson couplings to τ-leptons, gauge bosons and top quarks are still relatively weak. We leave an investigation of whether these measurements can probe

JHEP04(2026)038

In order to study the interplay between LHC and EDM constraints, we analyze three representative parameter planes in which we vary $\sin(\beta-\alpha_1)$ together with the imaginary part of one of the three flavor-alignment parameters ξ_f, with $f = u, d, \ell$ for up-type quarks, down-type quarks and leptons, respectively. For $\sin(\beta-\alpha_1) = 0$ the model is in the alignment limit, and the light Higgs boson H_1 playing the role of the SM-like Higgs boson has purely CP-even interactions, regardless of the values of ξ_f. Away from the alignment limit, $\sin(\beta-\alpha_1) \neq 0$, the CP-odd admixtures in the Yukawa couplings of H_1 increase with increasing values of $|\xi_f^{\text{Im}}|$. We therefore consider the cases where (i) only ξ_u^{Im} is varied, (ii) only ξ_d^{Im} is varied, and (iii) only ξ_ℓ^{Im} is varied, while the other two imaginary parts are set to zero. For this analysis, we fix all remaining parameters to the following values,

$$\begin{aligned} &m_{H_1}=125.1\,\text{GeV}, \quad m_{H_{2,3,4}}=m_{H^\pm}=200\,\text{GeV}, \quad m_\chi=90.0\,\text{GeV}, \quad \tan\beta=5, \quad \xi^{\text{Re}}_{u,d,\ell}=0, \\ &\alpha_{2,4,5,6}=0, \quad \alpha_3=\pi/4, \quad M=150\,\text{GeV}, \quad v_S=100\,\text{GeV}, \quad \lambda_5^{\text{Im}}=0, \quad \lambda^{\text{Re}}_{6,7,11}=0. \end{aligned} \tag{4.1}$$

In this setup the Yukawa sector reduces to type-I in the limit $\xi_f^{\text{Im}} = 0$. Moreover, since $\alpha_{4,5,6}$ and λ_5^{Im} are set to zero, the imaginary parts of the parameters ξ_f are the only sources of CP-violation.

Even though not central to the following discussion, we have verified that the benchmark planes satisfy all relevant theoretical and experimental constraints. In particular, vacuum stability (bounded-from-below conditions) and perturbative unitarity are ensured by the choice of relatively low masses for the BSM Higgs bosons, in combination with slightly smaller values of M and v_S. Constraints from the EWPOs are satisfied since we remain close to the alignment limit and the BSM Higgs states are taken to be mass-degenerate, thereby suppressing contributions to the ρ-parameter. The choice of $\tan\beta$ is motivated by compatibility with existing LHC searches in the CP-conserving limit. For the DM sector, we fix $m_\chi < 100\,\text{GeV}$, which opens invisible decay modes of the BSM scalars and thereby reduces their branching ratios for decays into visible final states such as $H_{2,3,4} \to \gamma\gamma, \tau^+\tau^-, ZZ$. This in turn weakens the corresponding constraints from LHC searches and provides additional freedom to vary $\sin(\beta-\alpha_1)$ and the alignment parameters ξ_f. Finally, we set $\alpha_3 = \pi/4$, so that H_2 and H_3 share an equal singlet component. If α_3 were also set to zero, the singlet field would completely decouple. For the parameter planes discussed here, we did not perform a comprehensive evaluation of the DM relic abundance. For the chosen value of $m_\chi = 90\,\text{GeV}$, however, the pNG DM candidate is expected to be largely underabundant, as efficient annihilation in the early universe proceeds via s-channel exchange of the SM-like Higgs boson H_1 into gauge-boson pairs. In addition, the proximity of m_χ to half of the BSM scalar masses further enhances annihilation through exchange of the heavier neutral scalars. Given this underproduction, and in combination with the cancellation mechanism suppressing direct-detection scattering amplitudes, current limits from DM direct detection experiments are not constraining the shown parameter planes.

In figure 15 we show the constraints on the parameter space in three parameter planes. Each plot shows the dependence on $\sin(\beta-\alpha_1)$ along the horizontal axis, while the vertical axis corresponds to one of the imaginary parts of the flavour-alignment parameters, ξ_u^{Im}

parameter space that is not already excluded by the inclusive LHC Higgs data and BSM Higgs boson searches, as well as the upper limit on the eEDM, for future studies (see ref. [49] for an analysis in the complex 2HDM).

JHEP04(2026)038

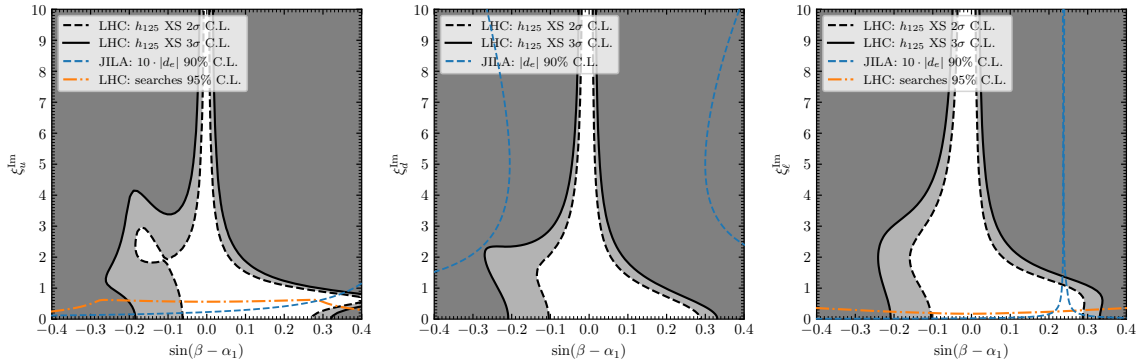

Figure 15. Parameter space excluded by LHC Higgs data in planes with $\sin(\beta-\alpha_1)$ on the horizontal axes and the flavour alignment parameters on the vertical axes: $\xi_u^{\rm Im}$ (left), $\xi_d^{\rm Im}$ (centre), and $\xi_\ell^{\rm Im}$ (right). The dashed and solid black lines indicate the exclusion region at 2σ and 3σ confidence level, respectively, obtained with `HiggsTools`. The region above the orange dot-dashed lines are excluded by cross section limits from LHC searches for additional Higgs bosons. The region above the dashed blue lines predict a value for the eEDM that is equal to the upper limit from JILA in the centre plot and equal to ten times the upper limit from JILA in the left and the right plot (the limit was increased by a factor of ten for better visibility).

(left), $\xi_d^{\rm Im}$ (center), and $\xi_\ell^{\rm Im}$ (right). The black dashed and solid curves indicate the regions excluded at 2σ ($\sim 95\%$) and 3σ ($\sim 99\%$) confidence level, respectively, based on Higgs boson cross-section measurements as obtained with `HiggsTools`. The orange dot-dashed lines represent exclusions from cross-section limits from LHC searches for BSM Higgs bosons, with the parameter space above the line being excluded. Finally, the blue dashed lines show where the predicted eEDM is equal to the current JILA upper limit in the central plot and to ten times this limit in the left and right plots (the scaling being introduced for visibility).

In the left plot we find that, in the CP-conserving limit, departures from alignment are allowed in the range $-0.06 \lesssim \sin(\beta-\alpha_1) \lesssim 0.27$ at 95% confidence level. This range is significantly modified when $\xi_u^{\rm Im}$ is non-zero. For moderate values around $\xi_u^{\rm Im} \sim 0.5$, deviations up to $\sin(\beta-\alpha_1) \sim 0.4$ become consistent with the LHC Higgs data. For larger values of $\xi_u^{\rm Im} \gtrsim 4$, the allowed region in $\sin(\beta-\alpha_1)$ shrinks significantly. Additional constraints arise from the eEDM, which in this plane excludes values $\xi_u^{\rm Im} \gtrsim 0.1$. This stringent exclusion is due to CP-violation in the $H_i t\bar{t}$ interactions, where the large top-quark Yukawa coupling induces sizable eEDM contributions at the two-loop level. We also find important restrictions from LHC searches for additional Higgs bosons. Values of $\xi_u^{\rm Im} \gtrsim 0.7$ are excluded, driven by cross section limits from searches for new spin-0 resonances decaying into photon pairs [135], since the loop-induced $H_i \to \gamma\gamma$ decay receives enhanced contributions from the top-quark loop when $\xi_u^{\rm Im}$ increases. Overall, while a CP-violating coupling of the SM-like Higgs boson to top quarks can enlarge the allowed departures from the alignment limit, compatibility with eEDM and BSM Higgs-boson searches would require to adjust the additional parameters to make the parameter space with $\xi_u^{\rm Im} \gtrsim 0.1$ be phenomenologically viable. For instance, one can modify the mixing angles α_i or one of the other alignment parameters $\xi_f^{\rm Im}$ to supress the eEDM, or raise the BSM scalar masses to alleviate the tensions with LHC searches.

JHEP04(2026)038

Turning to the second plot in the middle of figure 15, where $\xi_d^{\rm Im}$ is varied, we observe that increasing the CP-violating component in the down-type Yukawa sector leads overall to a reduction of the allowed range of $\sin(\beta-\alpha_1)$ and the parameter space that is consistent with LHC Higgs data. This is a consequence of the fact that a CP-odd component in the $H_1 b\bar{b}$ coupling enhances the partial width for decays of H_1 into bottom quarks, thereby increasing its total width. As a result, the branching ratios for decays into detected final states (most notably $H_1 \to \gamma\gamma$ and $H_1 \to ZZ^*$) are suppressed, which tightens the constraints from Higgs-boson signal-strength measurements. In this plane the dominant contributions to the eEDM are proportional to the bottom-quark Yukawa coupling and therefore strongly suppressed compared to the case discussed above in which the top-quark Yukawa coupling is CP-violating. Accordingly, the blue dashed curve, which indicates where the JILA bound would be saturated, lies entirely within the dark-shaded region already excluded at the 3σ level by LHC Higgs data. Finally, cross-section limits from searches for additional Higgs bosons do not impose constraints in this parameter plane, and therefore no orange line is visible in the plot. Increasing $\xi_d^{\rm Im}$ enhances the decays of the heavy scalars into $b\bar{b}$, but the corresponding LHC searches are significantly less sensitive due to the overwhelming QCD background. At the same time, the branching ratios into cleaner final states such as $\gamma\gamma$ and $\tau^+\tau^-$ are suppressed, weakening the impact of these searches. In summary, in the considered parameter plane the LHC Higgs-boson cross-section measurements provide the dominant sensitivity to CP-violation in the down-type quark sector.

The right plot of figure 15 shows the case where $\xi_\ell^{\rm Im}$ is varied, corresponding to CP-violating couplings of the Higgs bosons to charged leptons. Here, the range of $\sin(\beta-\alpha_1)$ allowed by the LHC Higgs data is less strongly affected by varying the imaginary part of the flavour alignment parameter compared to the two parameter planes discussed above. For moderate values of $\xi_\ell^{\rm Im} \sim 1$ the upper limit of the allowed region of $\sin(\beta-\alpha_1)$ increases slightly, while for values around $\xi_\ell^{\rm Im} \sim 2$ the lower limit moves to somewhat smaller values. This behaviour is mainly driven by modifications of the $H_1 \to \tau^+\tau^-$ decay mode, while the production cross sections are essentially unchanged because quark couplings remain unaffected. As a result, the overall dependence of the fit to the LHC Higgs data on $\xi_\ell^{\rm Im}$ is less pronounced than in the cases of $\xi_u^{\rm Im}$ and $\xi_d^{\rm Im}$. The eEDM provides an extremely strong constraint in this parameter plane. Since $\xi_\ell^{\rm Im}$ directly induces CP-violating interactions of H_i with electrons, the predicted eEDM exceeds the experimental bound across almost the entire parameter space. The only exception is a finely tuned region around $\sin(\beta-\alpha_1) \sim 0.25$, where accidental cancellations between different two-loop contributions lead to a vanishing eEDM. Whether this narrow window is physically viable, however, would require taking into account additional contributions, such as the so-called "kite" diagrams at two-loop level, as well as potential higher-loop effects. Furthermore, searches for additional Higgs bosons decaying into $\tau^+\tau^-$ final states [136] provide strong constraints in this plane, as shown with the orange line. With increasing $\xi_\ell^{\rm Im}$ the branching ratios for the decays of the heavy Higgs states into $\tau^+\tau^-$ are enhanced, and current limits exclude values of $\xi_\ell^{\rm Im} \gtrsim 0.4$. In summary, the parameter space with sizeable CP-violating lepton Yukawa couplings is effectively excluded in this parameter plane by a combination of eEDM limits and LHC searches for additional Higgs bosons. As in the case of $\xi_u^{\rm Im}$ (see left plot of figure 15), making the parameter regions shown in white, which are in agreement with the LHC Higgs data, physically viable would

JHEP04(2026)038

require adjusting other parameters of the model to suppress the eEDM and avoid the strong bounds from direct searches at the LHC.

4.4 Benchmark point with a strong first-order electroweak phase transition

In order to demonstrate explicitly that the cS2HDM can accommodate all the ingredients required for electroweak baryogenesis, while remaining consistent with current experimental constraints and predicting a valid DM candidate, we now discuss a representative benchmark scenario. Rather than performing a dedicated finite-temperature analysis of the electroweak phase transition (which is beyond the scope of this work and left for future studies) we adopt as a starting point a benchmark point from the literature in the context of the complex 2HDM (C2HDM) that has been shown to feature a strong first-order electroweak phase transition and CP-violation in the Higgs sector, leading to a baryon asymmetry of the correct order of magnitude [67]. We emphasize that the C2HDM benchmark point adopted here represents only one possible realization of a strong first-order electroweak phase transition. A variety of different Higgs-boson mass hierarchies and parameter configurations have been shown to give rise to such a transition, see e.g. refs. [66, 67, 137–139] for recent studies.

A generic feature of the C2HDM is that CP violation originates from a single independent source in the scalar potential, which simultaneously controls the CP-violating effects relevant for electroweak baryogenesis and induces contributions to EDMs. As a consequence, parameter regions that yield a sufficiently large baryon asymmetry are typically in tension with the stringent experimental bounds on the eEDM. This is also the case for the benchmark point adopted here, which predicts an electron EDM exceeding the current experimental limit by approximately one order of magnitude [67]. In the cS2HDM, however, additional and independent sources of CP violation are present that allow this tension to be alleviated. In particular, we show that by introducing a complex lepton flavour-alignment parameter ξ_ℓ, the predicted eEDM can be suppressed below the experimental bounds while keeping the Higgs-sector CP violation and the properties of the electroweak phase transition unchanged.

The modification of the lepton Yukawa sector compared to the C2HDM is expected to have negligible impact on the generation of the baryon asymmetry, because the dominant contributions to electroweak baryogenesis arise from transport processes involving the top quark due to its large Yukawa coupling. To obtain the correct DM relic abundance, a small mixing is introduced between H_1, the SM-like Higgs boson at 125 GeV, and the singlet state H_3 whose mass is chosen to be $m_{H_3} = 200\,\text{GeV}$, while the DM mass is set to $m_\chi = 80\,\text{GeV}$. The small mixing between H_1 and H_3, introduced by setting $\alpha_2 = 0.02$, generates $H_{1,3}\chi\chi$ couplings of the appropriate size to predict the correct DM relic abundance. We verified that the mixing is sufficiently small to not be in tension with LHC Higgs boson cross section measurements and LHC searches for additional Higgs bosons. Moreover, α_2 is small enough to induce only negligible modifications to the scalar potential, thus preserving the strength of the electroweak phase transition as it was found in the C2HDM.

In table 3 we state the values of the free parameters used for this benchmark scenario. The masses of H_2 and H_4 are taken over from the C2HDM parameter point, as well as the values of the mass parameter M, $\tan\beta$ and λ_5^{Im}. The mass difference between H_2 and H_4 is responsible for generating sizable quartic scalar couplings that facilitate an electroweak

JHEP04(2026)038

Input parameters	
m_{H_1}	125.09
m_{H_2}	420
m_{H_3}	200
m_{H_4}	660
$m_{H^\pm}$	660
m_χ	80
$\tan\beta$	2.960654
α_1	β
α_2	0.02
α_3	0.0
α_4	0.0525
α_5	0.0
α_6	-0.024708
M	m_{H_2}
v_S	100
λ_5^{Im}	0.563345
$\lambda_{6,7,11}^{\mathrm{Re}}$	0.0
$\xi_{u,d,\ell}^{\mathrm{Re}}$	0.0
$\xi_{u,d}^{\mathrm{Im}}$	0.0
ξ_ℓ^{Im}	$[-2, 1]$
Predictions	
ξ_n (transition strength)	2.4
η_s (baryon asymmetry)	$9.5 \cdot 10^{-11}$
$\Omega_\chi h^2$ (DM relic abundance)	0.11
$\Delta\chi^2$ (`HiggsSignals`)	< 3.14
Main branching ratios of BSM Higgs bosons	
$H_2 \to t\bar{t}$	98%
$H_2 \to H_1 Z$	1.3%
$H_3 \to \chi\chi$	100%
$H_4 \to t\bar{t}$	18%
$H_4 \to H_2 Z$	81%
$H^\pm \to tb$	17%
$H^\pm \to H_2 W^\pm$	83%

Table 3. Benchmark scenario for the cS2HDM adapted from a C2HDM parameter point reproducing the observed baryon-to-entropy ratio of the universe η_s. The top section shows the input parameters of the cS2HDM, the middle section a few model predictions for the electroweak phase transition, DM, and Higgs phenomenology, and the bottom section lists the dominant branching ratios of the BSM Higgs bosons. Masses are in GeV.

JHEP04(2026)038

phase transition with a strength of $\xi_n = 2.4$.[20] The values of the mixing angles α_1, α_4 and α_6 are set to coincide with the corresponding values in the C2HDM. The values of $\alpha_2 = 0.02$ and $v_S = 100\,\text{GeV}$ are chosen to obtain the correct DM relic abundance, and the remaining mixing angles α_3 and α_5 are set to zero.[21] Finally, the flavour alignment parameters are set to $\xi_{u,d,\ell} = 0$ to resemble the Yukawa type I, except for the imaginary part of ξ_ℓ, which was varied in the range $-2 \leq \xi_\ell^{\text{Im}} \leq 1$. We verified that this benchmark scenario satisfies all theoretical and experimental constraints discussed in section 3.

In ref. [67], the prediction for the baryon-to-entropy ratio η_s for the C2HDM parameter point was estimated to be $\eta_s = 9.5 \cdot 10^{-11}$, which roughly agrees with the observed value $\eta_s^{\text{obs}} = 8.7 \cdot 10^{-11}$, thus (considering the sizable theory uncertainties in the prediction of the baryon asymmetry generated during the transition) successfully realizing electroweak baryogenesis.[22] As discussed above, by appropriately choosing the parameters of the cS2HDM, the prediction for η_s can be taken over here since ξ_ℓ^{Im} does not have an important impact. The eEDM in the C2HDM was found to be $|d_e| = 1.5 \cdot 10^{-28}\,e$ cm, which is about two orders of magnitude above the current experimental limits. Hence, the non-observation of the eEDM precludes electroweak baryogenesis in this parameter point of the C2HDM. However, as can be seen in figure 16, in the cS2HDM we can use non-zero values of ξ_ℓ^{Im} in order to suppress the eEDM, making it compatible with the experimental limits for $\xi_\ell^{\text{Im}} \approx -1.45$ and $\xi_\ell^{\text{Im}} \approx 0.78$. As a result, we demonstrate here with a concrete parameter point that the cS2HDM is capable of predicting the correct baryon asymmetry of the universe via electroweak baryogenesis with an eEDM that falls well below the current experimental limits. At the same time, the DM relic abundance is predicted in agreement with the measured value via standard thermal freeze-out of Higgs-portal DM while satisfying the constraints from DM direct detection experiments. However, we stress again that in the blind spots in which the Barr-Zee-type contributions to the eEDM are strongly suppressed by means of large accidental cancellations, additional contributions to the eEDM (not taken into account here) become relevant and might be of the order of the current experimental bounds.

This benchmark scenario can be tested at the LHC, for instance via the detection of the heavier Higgs bosons. In particular, decays of a heavier scalar into a lighter Higgs boson plus a gauge boson, such as $H_4 \to H_2 Z$ or $H^\pm \to H_2 W^\pm$, have sizable branching ratios and provide promising search channels. Decays into pairs of DM particles, $\chi\chi$, would give signatures with missing transverse energy and could provide a mechanism to distinguish the cS2HDM from the C2HDM or more general 2HDMs. However, for this particular benchmark point, chosen deliberately close to the C2HDM, such signatures are not promising: the singlet-like state H_3 decays exclusively into $\chi\chi$ but has a very small direct production cross section due to

[20] The strength of the transition is defined as the ratio between the electroweak symmetry breaking vacuum expectation value and the transition temperature. To allow for electroweak baryogenesis, the value of ξ_n should be larger than one.

[21] To match a C2HDM parameter point to a cS2HDM parameter point, and using the most common notation for the mixing angles in the C2HDM, the cS2HDM mixing angles should be chosen according to: $\alpha_1 = \alpha_1^{\text{C2HDM}}$, $\alpha_2 = 0$, $\alpha_3 = 0$, $\alpha_4 = -\alpha_3^{\text{C2HDM}}$, $\alpha_5 = 0$ and $\alpha_6 = -\alpha_2^{\text{C2HDM}}$.

[22] Predictions for the resulting baryon asymmetry are subject to various different sources of theoretical uncertainties from the modeling of the expanding bubbles of true vacuum in the early universe and their interactions with the thermal plasma. Depending on the properties of the phase transition, the relative uncertainty on the prediction for η_s can be of an order of magnitude or more, see e.g. refs. [18, 139, 140].

JHEP04(2026)038

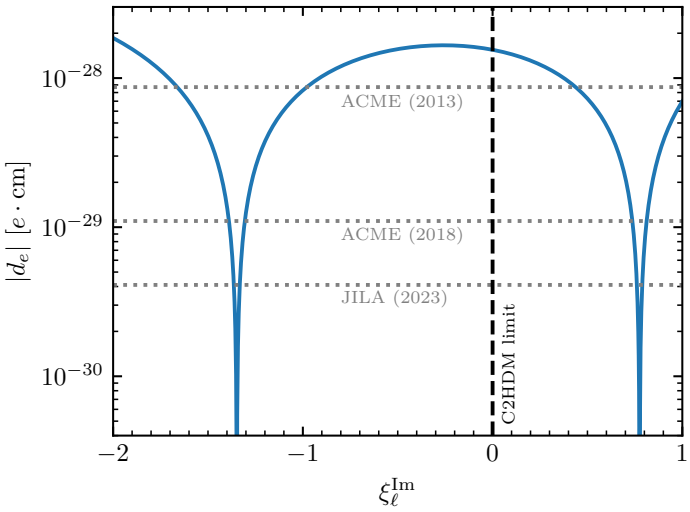

Figure 16. Predicted values of the eEDM as a function of ξ_ℓ^{Im}. The horizontal black lines represent the experimental upper limits from the ACME [124, 125] and JILA [126] collaborations. The black dashed vertical line indicates the limit ξ_ℓ^{Im} in which the benchmark scenario resembles the C2HDM parameter point (see main text for details).

its singlet nature, and it is also not produced in decays of the heavier states. At the same time, the branching ratios of the doublet-like BSM scalars H_2 and H_4 into $\chi\chi$ are negligible. To make the signal with missing energy more promising, one would have to go to parameter space regions of the cS2HDM that depart from C2HDM-like configurations, where the decays into $H_i \to \chi\chi$ can become relevant. To assess the potential for electroweak baryogenesis in such scenarios, however, a dedicated computation of the dynamics of the electroweak phase transition and the resulting baryon asymmetry in the cS2HDM is required, as the results cannot be simply inferred from the C2HDM. We leave such an analysis for future work.

5 Conclusions and outlook

In this paper, we have introduced the CP-violating singlet-extended 2-Higgs-Doublet Model (cS2HDM) as a unified framework that can simultaenously address two important open questions in particle physics: the unknown nature of Dark Matter (DM) and the unknown origin of the baryon asymmetry of the universe (BAU). In order to predict a viable Higgs-portal DM candidate, our model extends the Standard Model (SM) by incorporating a complex scalar singlet field that is charged under a global U(1) symmetry. The imaginary component of the singlet field acts as a pseudo-Nambu-Golstdone (pNG) DM particle which is naturally faint to DM direct detection experiments, while the real component gives rise to an additional Higgs boson contributing to the portal interactions between the visible and the dark sector. Additionally, we augment the Higgs sector with a second SU(2) Higgs doublet, whose presence allows for additional sources of CP-violation in the Higgs sector, and the additional scalar interactions can facilitate a strong first-order electroweak (EW) phase transition. In total, the Higgs sector of the cS2HDM predicts four neutral Higgs bosons, a pair of charged Higgs bosons, and a spin-0 DM state that interacts with the fermions exclusively

JHEP04(2026)038

via the exchange of Higgs bosons. Instead of imposing natural flavour conservation via a discrete $\mathbb{Z}_2$ symmetry under which the two Higgs doublets have opposite parity, we make use of flavour alignment in the Yukawa sector, which suppresses flavour-changing neutral currents while permitting additional sources of CP-violation in the Yukawa sector that would otherwise be forbidden. Both the new sources of CP-violation and the presence of a strong EW phase transition are necessary ingredients to explain the BAU via EW baryogenesis.

To put the cS2HDM into context, we briefly compare its features with those of other popular Higgs-portal DM models. The SM extended only by a singlet scalar can in principle provide both a DM candidate and a strong first-order EW phase transition, but it lacks additional CP-violating sources required for EW baryogenesis, and the predicted DM state is in strong tension with direct detection bounds except in the narrow Higgs-funnel region or for heavy DM masses in the multi-TeV range, making it an unappealing target for DM searches at the LHC. The 2-Higgs-Doublet Model (2HDM) offers complementary features: in its variant in which the additional Higgs doublet is inert (inert 2HDM), the model contains a stable DM candidate and can support a strong first-order EW phase transition. However, CP-violation in the Higgs sector is forbidden and the parameter space predicting the observed DM relic abundance is largely excluded by direct detection experiments. On the other hand, in the generic 2HDM in which both doublets take part in EW symmetry breaking, CP-violation is possible and EW baryogenesis can be realized, but no stable DM candidate is present. The 2HDM+a, which extends the 2HDM by a gauge singlet pseudoscalar field and a DM particle (typically a Dirac fermion), and which often serves as benchmark model for LHC DM searches, predicts a viable DM candidate with suppressed scattering rates at direct-detection experiments and can accommodate a strong first-order EW phase transition. However, its attractive cancellation mechaism suppressing spin-independent DM-nulceon scattering is in general spoiled once explicit CP-violation is introduced in the Higgs sector. By contrast, the cS2HDM retains the natural suppression of direct-detection rates associated with the pNG DM state under the presence of CP-violation in the Higgs sector. As a result, the cS2HDM can realize the standard thermal freeze-out picture of Higgs-portal DM, and it simultaneously provides a Higgs sector capable of supporting EW baryogenesis. Moreover, it offers several independent sources of CP-violation that can be arranged to evade the stringent experimental limits from the non-observation of the electron electric dipole moment (eEDM), in particular through cancellations between CP-violating sources in the scalar and the Yukawa sector. As a result, the cS2HDM stands out as a particularly attractive benchmark model for LHC DM searches.

After defining the model, we confronted it with a broad set of theoretical and experimental constraints. On the theory side, we imposed vacuum stability and perturbative unitarity bounds on the parameters of the scalar potential. On the phenomenological side, we computed predictions for Higgs-boson branching ratios and production cross sections at the LHC, enabling us to study the collider phenomenology of the model at the LHC. We calculated the DM relic abundance assuming thermal freeze-out and evaluated one-loop induced DM-nucleon scattering rates to assess the impact of direct detection experiments. We further investigated the consequences of EW precision observables by calculating at the one-loop level the EW ρ-parameter that is sensitive to mass splittings of different isospoin component of scalars due to the breaking of the custodial symmetry. Finally, we studied the predicted eEDM,

JHEP04(2026)038

which provides the most stringent probe of new CP-violation in the Higgs sector through recent upper bounds from ACME and JILA.

A novel aspect of this work concerns the treatment of DM direct detection in the presence of CP-violating portal interactions, which in the cS2HDM can be present both in the coupling of the DM state χ with the Higgs bosons H_i, as well as in the Yukawa couplings of the Higgs bosons H_i with the quarks q. By including these CP-violating interactions, we performed a matching of the CP-even and CP-odd operators describing the $\chi q \to \chi q$ scattering in the UV theory onto the non-relativistic effective field theory operators that describe the DM-nucleon scattering at low energies. A consequence of the CP-violating interactions is that the matching not only generates the usual spin-independent interactions but also spin-dependent and momentum-dependent operators. By studying these contributions numerically, we demonstrated that the dominant effect of the new CP-odd components of the portal couplings is a quantitative modification of the predicted spin-independent scattering cross sections, while the induced spin-dependent rates are far too small to be experimentally accessible.

Combining these ingredients, we performed a random parameter scan in which all theoretical, LHC, DM, eEDM, and precision constraints were imposed, allowing us to identify viable benchmark points. We analyzed in detail the severity of eEDM limits, and how they are related to DM direct detection bounds. We payed special attention to the impact of the new sources of CP-violation contained in the cS2HDM. In addition, we investigated in examplary parameter planes the sensitivity of current LHC Higgs data and direct searches for additional Higgs bosons to CP-violating couplings between the Higgs bosons and fermions, highlighting their complementarity with the stringent eEDM bounds.

With this paper, we provide a public software tool that incorporates all the ingredients discussed above and enables future studies of the cS2HDM. Our framework combines a modified version of `HDECAY` written in Fortran to calculate scalar branching ratios, an interface to the C++ package `HiggsTools` to obtain cross sections from effective couplings and confront the model with LHC Higgs data and limits from BSM Higgs boson searches at LEP and the LHC, as well as `micrOMEGAs` to compute the DM relic abundance. All other calculations discussed in our paper, including the one-loop predictions for DM scattering and the matching onto the non-relativistic effective field theory describing the interactions between χ and nucleons, the EW ρ-parameter, and the electron EDM at the two-loop level considering Barr-Zee-type contributions, are implemented directly in our tool. Our goal is that the cS2HDM can serve as a benchmark model both for LHC DM searches and for scenarios motivated by EW baryogenesis, for which it is essential to provide the necessary tools, which we make available with this publication under the following link:

https://gitlab.com/thomas.biekoetter/cs2hdmtools

As an outlook, we plan to extend this work by performing global scans of the high-dimensional parameter space of the cS2HDM using more sophisticated sampling techniques beyond random scanning, e.g. applying genetic algorithms using the public Fortran package `evortran` [141]. This will allow us to identify benchmark scenarios that are suitable to simultaneously realize EW baryogenesis and predict the observed DM relic abundance. Such studies will include a detailed analysis of the thermal history to determine regions with a

JHEP04(2026)038

sufficiently strong first-order EW phase transition by implementing the model into the public program `BSMPT` [142–144], as well as an exploration of the characteristic collider signatures of such scenarios model at the LHC.

Acknowledgments

RS and PG are supported by FCT under Contracts: UID/00618/2025 and 2024.03328.CERN (https://doi.org/10.54499/2024.03328.CERN). PG is also supported by FCT under the contract 2022.11377.BD (https://doi.org/10.54499/2022.11377.BD). MM acknowledges support by the Deutsche Forschungsgemeinschaft (DFG, German Research Foundation) under grant 396021762 - TRR 257. TB acknowledges the support of the Spanish Agencia Estatal de Investigación through the grant "IFT Centro de Excelencia Severo Ochoa CEX2020-001007-S". The project that gave rise to these results received the support of a fellowship from the "la Caixa" Foundation (ID 100010434). The fellowship code is LCF/BQ/PI24/12040018.

Data Availability Statement. This article has no associated data or the data will not be deposited.

Code Availability Statement. This article has associated code in a code repository. Available at: https://gitlab.com/thomas.biekoetter/cs2hdmtools.

Open Access. This article is distributed under the terms of the Creative Commons Attribution License (CC-BY4.0), which permits any use, distribution and reproduction in any medium, provided the original author(s) and source are credited.

References

[1] ATLAS collaboration, *Observation of a new particle in the search for the Standard Model Higgs boson with the ATLAS detector at the LHC*, *Phys. Lett. B* **716** (2012) 1 [arXiv:1207.7214] [INSPIRE].

[2] CMS collaboration, *Observation of a New Boson at a Mass of 125 GeV with the CMS Experiment at the LHC*, *Phys. Lett. B* **716** (2012) 30 [arXiv:1207.7235] [INSPIRE].

[3] ATLAS collaboration, *A detailed map of Higgs boson interactions by the ATLAS experiment ten years after the discovery*, *Nature* **607** (2022) 52 [*Erratum ibid.* **612** (2022) E24] [arXiv:2207.00092] [INSPIRE].

[4] CMS collaboration, *A portrait of the Higgs boson by the CMS experiment ten years after the discovery*, *Nature* **607** (2022) 60 [arXiv:2207.00043] [INSPIRE].

[5] ATLAS collaboration, *ATLAS searches for additional scalars and exotic Higgs boson decays with the LHC Run 2 dataset*, *Phys. Rept.* **1116** (2025) 184 [arXiv:2405.04914] [INSPIRE].

[6] V. Silveira and A. Zee, *SCALAR PHANTOMS*, *Phys. Lett. B* **161** (1985) 136 [INSPIRE].

[7] B. Patt and F. Wilczek, *Higgs-field portal into hidden sectors*, hep-ph/0605188 [INSPIRE].

[8] A. Falkowski, C. Gross and O. Lebedev, *A second Higgs from the Higgs portal*, *JHEP* **05** (2015) 057 [arXiv:1502.01361] [INSPIRE].

[9] V. Barger et al., *LHC Phenomenology of an Extended Standard Model with a Real Scalar Singlet*, *Phys. Rev. D* **77** (2008) 035005 [arXiv:0706.4311] [INSPIRE].

JHEP04(2026)038

[10] T. Biekötter and M. Pierre, *Higgs-boson visible and invisible constraints on hidden sectors*, *Eur. Phys. J. C* **82** (2022) 1026 [arXiv:2208.05505] [INSPIRE].

[11] G. Arcadi, F. Costa, A. Goudelis and O. Lebedev, *Higgs portal dark matter freeze-in at stronger coupling: observational benchmarks*, *JHEP* **07** (2024) 044 [arXiv:2405.03760] [INSPIRE].

[12] V. Barger et al., *Complex Singlet Extension of the Standard Model*, *Phys. Rev. D* **79** (2009) 015018 [arXiv:0811.0393] [INSPIRE].

[13] C. Gross, O. Lebedev and T. Toma, *Cancellation Mechanism for Dark-Matter-Nucleon Interaction*, *Phys. Rev. Lett.* **119** (2017) 191801 [arXiv:1708.02253] [INSPIRE].

[14] K. Huitu et al., *Probing pseudo-Goldstone dark matter at the LHC*, *Phys. Rev. D* **100** (2019) 015009 [arXiv:1812.05952] [INSPIRE].

[15] K. Kannike and M. Raidal, *Phase Transitions and Gravitational Wave Tests of Pseudo-Goldstone Dark Matter in the Softly Broken $U(1)$ Scalar Singlet Model*, *Phys. Rev. D* **99** (2019) 115010 [arXiv:1901.03333] [INSPIRE].

[16] A.D. Sakharov, *Violation of CP Invariance, C asymmetry, and baryon asymmetry of the universe*, *Pisma Zh. Eksp. Teor. Fiz.* **5** (1967) 32 [INSPIRE].

[17] V.A. Kuzmin, V.A. Rubakov and M.E. Shaposhnikov, *On the Anomalous Electroweak Baryon Number Nonconservation in the Early Universe*, *Phys. Lett. B* **155** (1985) 36 [INSPIRE].

[18] J. van de Vis, J. de Vries and M. Postma, *Bubble Trouble: a Review on Electroweak Baryogenesis*, arXiv:2508.09989 [INSPIRE].

[19] X.-M. Jiang et al., *Pseudo-Nambu-Goldstone dark matter and two-Higgs-doublet models*, *Phys. Rev. D* **100** (2019) 075011 [arXiv:1907.09684] [INSPIRE].

[20] Z. Zhang et al., *Phase transition gravitational waves from pseudo-Nambu-Goldstone dark matter and two Higgs doublets*, *JHEP* **05** (2021) 160 [arXiv:2102.01588] [INSPIRE].

[21] T. Biekötter and M.O. Olea-Romacho, *Reconciling Higgs physics and pseudo-Nambu-Goldstone dark matter in the S2HDM using a genetic algorithm*, *JHEP* **10** (2021) 215 [arXiv:2108.10864] [INSPIRE].

[22] M. Mühlleitner, J. Müller, S.L. Williamson and J. Wittbrodt, *The CN2HDM*, arXiv:2110.06680 [INSPIRE].

[23] T. Biekötter, P. Gabriel, M.O. Olea-Romacho and R. Santos, *Direct detection of pseudo-Nambu-Goldstone dark matter in a two Higgs doublet plus singlet extension of the SM*, *JHEP* **10** (2022) 126 [arXiv:2207.04973] [INSPIRE].

[24] N. Darvishi and B. Grzadkowski, *Pseudo-Goldstone dark matter model with CP violation*, *JHEP* **06** (2022) 092 [arXiv:2204.04737] [INSPIRE].

[25] T. Biekötter, S. Heinemeyer and G. Weiglein, *The CMS di-photon excess at 95 GeV in view of the LHC Run 2 results*, *Phys. Lett. B* **846** (2023) 138217 [arXiv:2303.12018] [INSPIRE].

[26] J.M. Cline and P.-A. Lemieux, *Electroweak phase transition in two Higgs doublet models*, *Phys. Rev. D* **55** (1997) 3873 [hep-ph/9609240] [INSPIRE].

[27] S. Weinberg, *Unitarity Constraints on CP Nonconservation in Higgs Exchange*, *Phys. Rev. D* **42** (1990) 860 [INSPIRE].

[28] S. Baum and N.R. Shah, *Two Higgs Doublets and a Complex Singlet: Disentangling the Decay Topologies and Associated Phenomenology*, *JHEP* **12** (2018) 044 [arXiv:1808.02667] [INSPIRE].

JHEP04(2026)038

[29] S. Heinemeyer et al., *Phenomenology of a 96 GeV Higgs boson in the 2HDM with an additional singlet*, *Phys. Rev. D* **106** (2022) 075003 [arXiv:2112.11958] [INSPIRE].

[30] J. Dutta, G. Moortgat-Pick and M. Schreiber, *Phenomenology of the dark matter sector in the 2HDM extended with complex scalar singlet*, *Eur. Phys. J. Plus* **140** (2025) 87 [arXiv:2203.05509] [INSPIRE].

[31] J. Dutta et al., *Search for Dark Matter in 2HDMS at LHC and future Lepton Colliders*, arXiv:2504.14529 [INSPIRE].

[32] S. Ipek, D. McKeen and A.E. Nelson, *A Renormalizable Model for the Galactic Center Gamma Ray Excess from Dark Matter Annihilation*, *Phys. Rev. D* **90** (2014) 055021 [arXiv:1404.3716] [INSPIRE].

[33] J.M. No, *Looking through the pseudoscalar portal into dark matter: Novel mono-Higgs and mono-Z signatures at the LHC*, *Phys. Rev. D* **93** (2016) 031701 [arXiv:1509.01110] [INSPIRE].

[34] LHC Dark Matter Working Group collaboration, *LHC Dark Matter Working Group: Next-generation spin-0 dark matter models*, *Phys. Dark Univ.* **27** (2020) 100351 [arXiv:1810.09420] [INSPIRE].

[35] C. Boehm et al., *Extended gamma-ray emission from Coy Dark Matter*, *JCAP* **05** (2014) 009 [arXiv:1401.6458] [INSPIRE].

[36] A. Alves, S. Profumo, F.S. Queiroz and W. Shepherd, *Effective field theory approach to the Galactic Center gamma-ray excess*, *Phys. Rev. D* **90** (2014) 115003 [arXiv:1403.5027] [INSPIRE].

[37] S.J. Huber, K. Mimasu and J.M. No, *Baryogenesis from transitional CP violation in the early Universe*, *Phys. Rev. D* **107** (2023) 075042 [arXiv:2208.10512] [INSPIRE].

[38] S. Liu and L. Wang, *Spontaneous CP violation electroweak baryogenesis and gravitational wave through multistep phase transitions*, *Phys. Rev. D* **107** (2023) 115008 [arXiv:2302.04639] [INSPIRE].

[39] A. Djouadi, J. Kalinowski and M. Spira, *HDECAY: A Program for Higgs boson decays in the standard model and its supersymmetric extension*, *Comput. Phys. Commun.* **108** (1998) 56 [hep-ph/9704448] [INSPIRE].

[40] HDECAY collaboration, *HDECAY: Twenty$_{++}$ years after*, *Comput. Phys. Commun.* **238** (2019) 214 [arXiv:1801.09506] [INSPIRE].

[41] H. Bahl et al., *HiggsTools: BSM scalar phenomenology with new versions of HiggsBounds and HiggsSignals*, *Comput. Phys. Commun.* **291** (2023) 108803 [arXiv:2210.09332] [INSPIRE].

[42] G. Bélanger, F. Boudjema, A. Pukhov and A. Semenov, *MicrOMEGAs 2.0: A program to calculate the relic density of dark matter in a generic model*, *Comput. Phys. Commun.* **176** (2007) 367 [hep-ph/0607059] [INSPIRE].

[43] G. Bélanger et al., *micrOMEGAs5.0: Freeze-in*, *Comput. Phys. Commun.* **231** (2018) 173 [arXiv:1801.03509] [INSPIRE].

[44] H.E. Haber and D. O'Neil, *Basis-independent methods for the two-Higgs-doublet model. II. The significance of tanβ*, *Phys. Rev. D* **74** (2006) 015018 [*Erratum ibid.* **74** (2006) 059905] [hep-ph/0602242] [INSPIRE].

[45] A. Pich and P. Tuzon, *Yukawa Alignment in the Two-Higgs-Doublet Model*, *Phys. Rev. D* **80** (2009) 091702 [arXiv:0908.1554] [INSPIRE].

JHEP04(2026)038

[46] P.M. Ferreira, L. Lavoura and J.P. Silva, *Renormalization-group constraints on Yukawa alignment in multi-Higgs-doublet models*, *Phys. Lett. B* **688** (2010) 341 [arXiv:1001.2561] [INSPIRE].

[47] A. Peñuelas and A. Pich, *Flavour alignment in multi-Higgs-doublet models*, *JHEP* **12** (2017) 084 [arXiv:1710.02040] [INSPIRE].

[48] S.L. Glashow and S. Weinberg, *Natural Conservation Laws for Neutral Currents*, *Phys. Rev. D* **15** (1977) 1958 [INSPIRE].

[49] T. Biekötter et al., *Impact of new experimental data on the C2HDM: the strong interdependence between LHC Higgs data and the electron EDM*, *JHEP* **05** (2024) 127 [arXiv:2403.02425] [INSPIRE].

[50] D. Azevedo et al., *One-loop contribution to dark-matter-nucleon scattering in the pseudo-scalar dark matter model*, *JHEP* **01** (2019) 138 [arXiv:1810.06105] [INSPIRE].

[51] H.E. Haber, V. Keus and R. Santos, *P-even, CP-violating signals in scalar-mediated processes*, *Phys. Rev. D* **106** (2022) 095038 [arXiv:2206.09643] [INSPIRE].

[52] S. Kanemura, M. Kubota and K. Yagyu, *Aligned CP-violating Higgs sector canceling the electric dipole moment*, *JHEP* **08** (2020) 026 [arXiv:2004.03943] [INSPIRE].

[53] B.W. Lee and S. Weinberg, *Cosmological Lower Bound on Heavy Neutrino Masses*, *Phys. Rev. Lett.* **39** (1977) 165 [INSPIRE].

[54] T. Binder, T. Bringmann, M. Gustafsson and A. Hryczuk, *Early kinetic decoupling of dark matter: when the standard way of calculating the thermal relic density fails*, *Phys. Rev. D* **96** (2017) 115010 [*Erratum ibid.* **101** (2020) 099901] [arXiv:1706.07433] [INSPIRE].

[55] T. Abe, *Early kinetic decoupling and a pseudo-Nambu-Goldstone dark matter model*, *Phys. Rev. D* **104** (2021) 035025 [arXiv:2106.01956] [INSPIRE].

[56] L.J. Hall, K. Jedamzik, J. March-Russell and S.M. West, *Freeze-In Production of FIMP Dark Matter*, *JHEP* **03** (2010) 080 [arXiv:0911.1120] [INSPIRE].

[57] M.J.D. Powell, *An efficient method for finding the minimum of a function of several variables without calculating derivatives*, *Comput. J.* **7** (1964) 155 [INSPIRE].

[58] https://github.com/jacobwilliams/PowellOpt, [Accessed: 2024-04-01].

[59] A. Arhrib et al., *Extended Higgs sector of 2HDM with real singlet facing LHC data*, *Eur. Phys. J. C* **80** (2020) 13 [arXiv:1811.12431] [INSPIRE].

[60] C.-Y. Chen, M. Freid and M. Sher, *Next-to-minimal two Higgs doublet model*, *Phys. Rev. D* **89** (2014) 075009 [arXiv:1312.3949] [INSPIRE].

[61] G.C. Dorsch, S.J. Huber, K. Mimasu and J.M. No, *Echoes of the Electroweak Phase Transition: Discovering a second Higgs doublet through $A_0 \to ZH_0$*, *Phys. Rev. Lett.* **113** (2014) 211802 [arXiv:1405.5537] [INSPIRE].

[62] P. Basler et al., *Strong First Order Electroweak Phase Transition in the CP-Conserving 2HDM Revisited*, *JHEP* **02** (2017) 121 [arXiv:1612.04086] [INSPIRE].

[63] T. Biekötter et al., *The trap in the early Universe: impact on the interplay between gravitational waves and LHC physics in the 2HDM*, *JCAP* **03** (2023) 031 [arXiv:2208.14466] [INSPIRE].

[64] T. Biekötter et al., *First shot of the smoking gun: probing the electroweak phase transition in the 2HDM with novel searches for $A \to ZH$ in $\ell^+\ell^- t\bar{t}$ and $\nu\nu b\bar{b}$ final states*, *JHEP* **01** (2024) 107 [arXiv:2309.17431] [INSPIRE].

JHEP04(2026)038

[65] G.C. Dorsch, S.J. Huber, K. Mimasu and J.M. No, *The Higgs Vacuum Uplifted: Revisiting the Electroweak Phase Transition with a Second Higgs Doublet*, *JHEP* **12** (2017) 086 [arXiv:1705.09186] [INSPIRE].

[66] P. Basler, M. Mühlleitner and J. Wittbrodt, *The CP-Violating 2HDM in Light of a Strong First Order Electroweak Phase Transition and Implications for Higgs Pair Production*, *JHEP* **03** (2018) 061 [arXiv:1711.04097] [INSPIRE].

[67] T. Biekötter and M.O. Olea-Romacho, *Benchmarking a fading window: electroweak baryogenesis in the C2HDM, LHC constraints after Run 2 and prospects for LISA*, *JHEP* **12** (2025) 040 [arXiv:2505.09670] [INSPIRE].

[68] P. Basler, M. Mühlleitner and J. Müller, *Electroweak Phase Transition in Non-Minimal Higgs Sectors*, *JHEP* **05** (2020) 016 [arXiv:1912.10477] [INSPIRE].

[69] P. Bechtle et al., *HiggsSignals: Confronting arbitrary Higgs sectors with measurements at the Tevatron and the LHC*, *Eur. Phys. J. C* **74** (2014) 2711 [arXiv:1305.1933] [INSPIRE].

[70] P. Bechtle et al., *Probing the Standard Model with Higgs signal rates from the Tevatron, the LHC and a future ILC*, *JHEP* **11** (2014) 039 [arXiv:1403.1582] [INSPIRE].

[71] P. Bechtle et al., *HiggsSignals-2: Probing new physics with precision Higgs measurements in the LHC 13 TeV era*, *Eur. Phys. J. C* **81** (2021) 145 [arXiv:2012.09197] [INSPIRE].

[72] H. Georgi and D.V. Nanopoulos, *Suppression of Flavor Changing Effects From Neutral Spinless Meson Exchange in Gauge Theories*, *Phys. Lett. B* **82** (1979) 95 [INSPIRE].

[73] P. Bechtle et al., *HiggsBounds: Confronting Arbitrary Higgs Sectors with Exclusion Bounds from LEP and the Tevatron*, *Comput. Phys. Commun.* **181** (2010) 138 [arXiv:0811.4169] [INSPIRE].

[74] P. Bechtle et al., *HiggsBounds 2.0.0: Confronting Neutral and Charged Higgs Sector Predictions with Exclusion Bounds from LEP and the Tevatron*, *Comput. Phys. Commun.* **182** (2011) 2605 [arXiv:1102.1898] [INSPIRE].

[75] P. Bechtle et al., HiggsBounds – 4*: Improved Tests of Extended Higgs Sectors against Exclusion Bounds from LEP, the Tevatron and the LHC*, *Eur. Phys. J. C* **74** (2014) 2693 [arXiv:1311.0055] [INSPIRE].

[76] P. Bechtle et al., *HiggsBounds-5: Testing Higgs Sectors in the LHC 13 TeV Era*, *Eur. Phys. J. C* **80** (2020) 1211 [arXiv:2006.06007] [INSPIRE].

[77] S. Gori, H.E. Haber and E. Santos, *High scale flavor alignment in two-Higgs doublet models and its phenomenology*, *JHEP* **06** (2017) 110 [arXiv:1703.05873] [INSPIRE].

[78] M. Misiak and M. Steinhauser, *Weak radiative decays of the B meson and bounds on $M_{H^\pm}$ in the Two-Higgs-Doublet Model*, *Eur. Phys. J. C* **77** (2017) 201 [arXiv:1702.04571] [INSPIRE].

[79] M. Misiak, A. Rehman and M. Steinhauser, *Towards $\overline{B} \to X_s\gamma$ at the NNLO in QCD without interpolation in m_c*, *JHEP* **06** (2020) 175 [arXiv:2002.01548] [INSPIRE].

[80] D.A. Ross and M.J.G. Veltman, *Neutral currents and the Higgs mechanism*, *Nucl. Phys. B* **95** (1975) 135 [INSPIRE].

[81] Particle Data Group collaboration, *Review of Particle Physics*, *PTEP* **2022** (2022) 083C01 [INSPIRE].

[82] M.B. Einhorn, D.R.T. Jones and M.J.G. Veltman, *Heavy Particles and the rho Parameter in the Standard Model*, *Nucl. Phys. B* **191** (1981) 146 [INSPIRE].

[83] M.E. Peskin and T. Takeuchi, *A new constraint on a strongly interacting Higgs sector*, *Phys. Rev. Lett.* **65** (1990) 964 [INSPIRE].

JHEP04(2026)038

[84] J. Haller et al., *Update of the global electroweak fit and constraints on two-Higgs-doublet models*, *Eur. Phys. J. C* **78** (2018) 675 [arXiv:1803.01853] [INSPIRE].

[85] LHCb collaboration, *Measurement of the W boson mass*, *JHEP* **01** (2022) 036 [arXiv:2109.01113] [INSPIRE].

[86] ATLAS collaboration, *Measurement of the W-boson mass and width with the ATLAS detector using proton-proton collisions at* $\sqrt{s} = 7$ *TeV*, *Eur. Phys. J. C* **84** (2024) 1309 [arXiv:2403.15085] [INSPIRE].

[87] CMS collaboration, *High-precision measurement of the W boson mass with the CMS experiment at the LHC*, arXiv:2412.13872 [INSPIRE].

[88] CDF collaboration, *High-precision measurement of the W boson mass with the CDF II detector*, *Science* **376** (2022) 170 [INSPIRE].

[89] H. Song, W. Su and M. Zhang, *Electroweak phase transition in 2HDM under Higgs, Z-pole, and W precision measurements*, *JHEP* **10** (2022) 048 [arXiv:2204.05085] [INSPIRE].

[90] H. Bahl, J. Braathen and G. Weiglein, *New physics effects on the W-boson mass from a doublet extension of the SM Higgs sector*, *Phys. Lett. B* **833** (2022) 137295 [arXiv:2204.05269] [INSPIRE].

[91] T. Biekötter, S. Heinemeyer and G. Weiglein, *Excesses in the low-mass Higgs-boson search and the W-boson mass measurement*, *Eur. Phys. J. C* **83** (2023) 450 [arXiv:2204.05975] [INSPIRE].

[92] C. Li, J. Li, S. Su and W. Su, *Electroweak precision constraints of the 2HDM+S*, *Chin. Phys.* **50** (2026) 023105 [arXiv:2507.14288] [INSPIRE].

[93] N.D. Christensen and C. Duhr, *FeynRules — Feynman rules made easy*, *Comput. Phys. Commun.* **180** (2009) 1614 [arXiv:0806.4194] [INSPIRE].

[94] A. Alloul et al., *FeynRules 2.0 — A complete toolbox for tree-level phenomenology*, *Comput. Phys. Commun.* **185** (2014) 2250 [arXiv:1310.1921] [INSPIRE].

[95] A. Belyaev, N.D. Christensen and A. Pukhov, *CalcHEP 3.4 for collider physics within and beyond the Standard Model*, *Comput. Phys. Commun.* **184** (2013) 1729 [arXiv:1207.6082] [INSPIRE].

[96] Planck collaboration, *Planck 2018 results. VI. Cosmological parameters*, *Astron. Astrophys.* **641** (2020) A6 [*Erratum ibid.* **652** (2021) C4] [arXiv:1807.06209] [INSPIRE].

[97] R. Capucha et al., *Freeze-in as a complementary process to freeze-out*, *JHEP* **09** (2024) 113 [arXiv:2407.04809] [INSPIRE].

[98] S. Glaus et al., *Electroweak Corrections in a Pseudo-Nambu Goldstone Dark Matter Model Revisited*, *JHEP* **12** (2020) 034 [arXiv:2008.12985] [INSPIRE].

[99] F. Bishara, J. Brod, B. Grinstein and J. Zupan, *From quarks to nucleons in dark matter direct detection*, *JHEP* **11** (2017) 059 [arXiv:1707.06998] [INSPIRE].

[100] K. Ishiwata and T. Toma, *Probing pseudo Nambu-Goldstone boson dark matter at loop level*, *JHEP* **12** (2018) 089 [arXiv:1810.08139] [INSPIRE].

[101] E. Witten, *Heavy Quark Contributions to Deep Inelastic Scattering*, *Nucl. Phys. B* **104** (1976) 445 [INSPIRE].

[102] J.J. Fan, M. Reece and L.-T. Wang, *Non-relativistic effective theory of dark matter direct detection*, *JCAP* **11** (2010) 042 [arXiv:1008.1591] [INSPIRE].

JHEP04(2026)038

[103] D.G. Cerdeno and A.M. Green, *Direct detection of WIMPs*, arXiv:1002.1912 [DOI:10.1017/CBO9780511770739.018] [INSPIRE].

[104] LZ collaboration, *Dark Matter Search Results from 4.2 Tonne-Years of Exposure of the LUX-ZEPLIN (LZ) Experiment*, *Phys. Rev. Lett.* **135** (2025) 011802 [arXiv:2410.17036] [INSPIRE].

[105] LZ collaboration, *First Dark Matter Search Results from the LUX-ZEPLIN (LZ) Experiment*, *Phys. Rev. Lett.* **131** (2023) 041002 [arXiv:2207.03764] [INSPIRE].

[106] LZ collaboration, *First constraints on WIMP-nucleon effective field theory couplings in an extended energy region from LUX-ZEPLIN*, *Phys. Rev. D* **109** (2024) 092003 [arXiv:2312.02030] [INSPIRE].

[107] N. Anand, A.L. Fitzpatrick and W.C. Haxton, *Weakly interacting massive particle-nucleus elastic scattering response*, *Phys. Rev. C* **89** (2014) 065501 [arXiv:1308.6288] [INSPIRE].

[108] F. Bishara, J. Brod, B. Grinstein and J. Zupan, *DirectDM: a tool for dark matter direct detection*, arXiv:1708.02678 [INSPIRE].

[109] P. Junnarkar and A. Walker-Loud, *Scalar strange content of the nucleon from lattice QCD*, *Phys. Rev. D* **87** (2013) 114510 [arXiv:1301.1114] [INSPIRE].

[110] XQCD collaboration, *πN and strangeness sigma terms at the physical point with chiral fermions*, *Phys. Rev. D* **94** (2016) 054503 [arXiv:1511.09089] [INSPIRE].

[111] S. Durr et al., *Lattice computation of the nucleon scalar quark contents at the physical point*, *Phys. Rev. Lett.* **116** (2016) 172001 [arXiv:1510.08013] [INSPIRE].

[112] FERMI-LAT collaboration, *Searching for Dark Matter Annihilation from Milky Way Dwarf Spheroidal Galaxies with Six Years of Fermi Large Area Telescope Data*, *Phys. Rev. Lett.* **115** (2015) 231301 [arXiv:1503.02641] [INSPIRE].

[113] HESS collaboration, *Search for γ-Ray Line Signals from Dark Matter Annihilations in the Inner Galactic Halo from 10 Years of Observations with H.E.S.S.*, *Phys. Rev. Lett.* **120** (2018) 201101 [arXiv:1805.05741] [INSPIRE].

[114] MAGIC collaboration, *Search for Gamma-Ray Spectral Lines from Dark Matter Annihilation up to 100 TeV toward the Galactic Center with MAGIC*, *Phys. Rev. Lett.* **130** (2023) 061002 [arXiv:2212.10527] [INSPIRE].

[115] AMS collaboration, *Antiproton Flux, Antiproton-to-Proton Flux Ratio, and Properties of Elementary Particle Fluxes in Primary Cosmic Rays Measured with the Alpha Magnetic Spectrometer on the International Space Station*, *Phys. Rev. Lett.* **117** (2016) 091103 [INSPIRE].

[116] FERMI-LAT collaboration, *The Fermi Galactic Center GeV Excess and Implications for Dark Matter*, *Astrophys. J.* **840** (2017) 43 [arXiv:1704.03910] [INSPIRE].

[117] M.O. Olea-Romacho, M. Fairbairn and P. Ralegankar, *Can WIMPs survive the legacy of a magnetised early Universe?*, *SciPost Phys.* **20** (2026) 044 [arXiv:2507.18692] [INSPIRE].

[118] W. Altmannshofer, S. Gori, N. Hamer and H.H. Patel, *Electron EDM in the complex two-Higgs doublet model*, *Phys. Rev. D* **102** (2020) 115042 [arXiv:2009.01258] [INSPIRE].

[119] S.M. Barr and A. Zee, *Electric Dipole Moment of the Electron and of the Neutron*, *Phys. Rev. Lett.* **65** (1990) 21 [*Erratum ibid.* **65** (1990) 2920] [INSPIRE].

[120] T. Abe, J. Hisano, T. Kitahara and K. Tobioka, *Gauge invariant Barr-Zee type contributions to fermionic EDMs in the two-Higgs doublet models*, *JHEP* **01** (2014) 106 [*Erratum ibid.* **04** (2016) 161] [arXiv:1311.4704] [INSPIRE].

JHEP04(2026)038

[121] K. Ning and M.J. Ramsey-Musolf, *Revisiting the electron EDM in the NMSSM*, *Phys. Lett. B* **869** (2025) 139867 [arXiv:2507.06320] [INSPIRE].

[122] J. Brod, Z. Polonsky and E. Stamou, *A precise electron EDM constraint on CP-odd heavy-quark Yukawas*, *JHEP* **06** (2024) 091 [arXiv:2306.12478] [INSPIRE].

[123] W. Altmannshofer et al., *Electron EDM and $\Gamma(\mu \to e\gamma)$ in the 2HDM*, *JHEP* **06** (2025) 156 [arXiv:2410.17313] [INSPIRE].

[124] ACME collaboration, *Order of Magnitude Smaller Limit on the Electric Dipole Moment of the Electron*, *Science* **343** (2014) 269 [arXiv:1310.7534] [INSPIRE].

[125] ACME collaboration, *Improved limit on the electric dipole moment of the electron*, *Nature* **562** (2018) 355 [INSPIRE].

[126] T.S. Roussy et al., *An improved bound on the electron's electric dipole moment*, *Science* **381** (2023) adg4084 [arXiv:2212.11841] [INSPIRE].

[127] D.E. Morrissey and M.J. Ramsey-Musolf, *Electroweak baryogenesis*, *New J. Phys.* **14** (2012) 125003 [arXiv:1206.2942] [INSPIRE].

[128] DARWIN collaboration, *DARWIN: towards the ultimate dark matter detector*, *JCAP* **11** (2016) 017 [arXiv:1606.07001] [INSPIRE].

[129] CMS collaboration, *Analysis of the CP structure of the Yukawa coupling between the Higgs boson and τ leptons in proton-proton collisions at $\sqrt{s} = 13$ TeV*, *JHEP* **06** (2022) 012 [arXiv:2110.04836] [INSPIRE].

[130] ATLAS collaboration, *Measurement of the CP properties of Higgs boson interactions with τ-leptons with the ATLAS detector*, *Eur. Phys. J. C* **83** (2023) 563 [arXiv:2212.05833] [INSPIRE].

[131] CMS collaboration, *Search for CP violation in ttH and tH production in multilepton channels in proton-proton collisions at $\sqrt{s} = 13$ TeV*, *JHEP* **07** (2023) 092 [arXiv:2208.02686] [INSPIRE].

[132] ATLAS collaboration, *Probing the CP nature of the top-Higgs Yukawa coupling in $t\bar{t}H$ and tH events with $H \to b\bar{b}$ decays using the ATLAS detector at the LHC*, *Phys. Lett. B* **849** (2024) 138469 [arXiv:2303.05974] [INSPIRE].

[133] ATLAS collaboration, *Test of CP Invariance in Higgs Boson Vector-Boson-Fusion Production Using the $H \to \gamma\gamma$ Channel with the ATLAS Detector*, *Phys. Rev. Lett.* **131** (2023) 061802 [arXiv:2208.02338] [INSPIRE].

[134] ATLAS collaboration, *Test of CP-invariance of the Higgs boson in vector-boson fusion production and in its decay into four leptons*, *JHEP* **05** (2024) 105 [arXiv:2304.09612] [INSPIRE].

[135] ATLAS collaboration, *Search for resonances decaying into photon pairs in 139 fb^{-1} of pp collisions at $\sqrt{s} = 13$ TeV with the ATLAS detector*, *Phys. Lett. B* **822** (2021) 136651 [arXiv:2102.13405] [INSPIRE].

[136] CMS collaboration, *Searches for additional Higgs bosons and for vector leptoquarks in $\tau\tau$ final states in proton-proton collisions at $\sqrt{s} = 13$ TeV*, *JHEP* **07** (2023) 073 [arXiv:2208.02717] [INSPIRE].

[137] P. Basler, L. Biermann, M. Mühlleitner and J. Müller, *Electroweak baryogenesis in the CP-violating two-Higgs doublet model*, *Eur. Phys. J. C* **83** (2023) 57 [arXiv:2108.03580] [INSPIRE].

JHEP04(2026)038

[138] D. Gonçalves, A. Kaladharan and Y. Wu, *Gravitational waves, bubble profile, and baryon asymmetry in the complex 2HDM*, *Phys. Rev. D* **108** (2023) 075010 [arXiv:2307.03224] [INSPIRE].

[139] G. Barni, *Electroweak Baryogenesis with BARYONET: a self-contained review of the WKB approach*, arXiv:2510.21915 [INSPIRE].

[140] G.C. Dorsch, S.J. Huber and T. Konstandin, *On the wall velocity dependence of electroweak baryogenesis*, *JCAP* **08** (2021) 020 [arXiv:2106.06547] [INSPIRE].

[141] T. Biekötter, *evortran: A modern Fortran package for genetic algorithms with applications from LHC data fitting to LISA signal reconstruction*, *SciPost Phys. Codeb.* **64** (2026) 1 [arXiv:2507.06082] [INSPIRE].

[142] P. Basler and M. Mühlleitner, *BSMPT (Beyond the Standard Model Phase Transitions): A tool for the electroweak phase transition in extended Higgs sectors*, *Comput. Phys. Commun.* **237** (2019) 62 [arXiv:1803.02846] [INSPIRE].

[143] P. Basler, M. Mühlleitner and J. Müller, *BSMPT v2 a tool for the electroweak phase transition and the baryon asymmetry of the universe in extended Higgs Sectors*, *Comput. Phys. Commun.* **269** (2021) 108124 [arXiv:2007.01725] [INSPIRE].

[144] P. Basler et al., *BSMPT v3 a tool for phase transitions and primordial gravitational waves in extended Higgs sectors*, *Comput. Phys. Commun.* **316** (2025) 109766 [arXiv:2404.19037] [INSPIRE].

JHEP04(2026)038